

# **In situ gelling Nanofibers: An Innovative Strategy for the Treatment of Keratomycosis**

Dissertation

zur Erlangung des

Doktorgrades der Naturwissenschaften (Dr. rer. nat.)

der

Naturwissenschaftlichen Fakultät I

-Biowissenschaften-

der Martin-Luther-Universität Halle-Wittenberg

vorgelegt von

Herrn Dipl.-Pharm. Benedikt Nicolas Göttel

geboren am 05.07.1992 in Landstuhl

Gutachter:

1. Prof. Dr. Karsten Mäder
2. Prof. Dr. Arne Viestenz
3. Prof. Dr. Miriam Breunig

Tag der öffentlichen Verteidigung: 06.05.2022 in Halle (Saale)

*„Wahre Wissenschaft lehrt vor allem, zu zweifeln und unwissend zu sein.“*

Miguel de Unamuno (1864-1936)

## Table of Contents

<b>Table of Contents .....</b>	<b>I</b>
<b>List of Abbreviations and Symbols.....</b>	<b>IV</b>
<b>1 Introduction.....</b>	<b>1</b>
1.1 Ocular drug delivery.....	1
1.2 Fungal keratitis.....	9
1.3 Research objectives .....	10
<b>2 Materials .....</b>	<b>13</b>
2.1 Polymers.....	13
2.2 Active pharmaceutical ingredient.....	15
2.3 Further excipients and materials.....	17
2.4 Biological materials.....	18
2.5 Miscellaneous laboratory equipment.....	18
<b>3 Methods.....</b>	<b>20</b>
3.1 Formulation development and characterization .....	20
3.1.1 Rheology.....	20
3.1.2 Light microscopy.....	20
3.1.3 Electrospinning.....	21
3.1.4 Environmental scanning electron microscopy.....	25
3.1.5 Thermogravimetric analysis .....	25
3.1.6 Nanoscale 3D x-ray imaging .....	25
3.1.7 <sup>1</sup> H-nuclear magnetic resonance ( <sup>1</sup> H-NMR).....	26
3.1.8 3D printing.....	26
3.1.9 Curvature formation .....	27
3.1.10 Ocular residence time <i>in vitro</i> .....	27
3.2 Nanoparticles.....	29
3.2.1 Amphotericin B loaded nanoparticles .....	29
3.2.2 DiR loaded nanoparticles .....	30
3.2.3 Photon correlation spectroscopy.....	30
3.2.4 Nanoparticle tracking analysis.....	31
3.2.5 Zeta potential .....	31
3.2.6 Drug load and entrapment efficacy .....	32
3.3 Amphotericin B-Eudragit L-polyelectrolyte complex.....	33
3.3.1 Preparation polyelectrolyte complex .....	33

---

3.3.2	Lyophilisation.....	34
3.3.3	UV/Vis-spectroscopy .....	34
3.3.4	Attenuated total reflection infrared spectroscopy.....	34
3.3.5	Drug load of polyelectrolyte complex .....	35
3.3.6	X-Ray powder diffraction.....	35
3.3.7	Differential scanning calorimetry .....	35
3.3.8	Zeta potential .....	36
3.4	Nanofiber characterization .....	36
3.4.1	Drug load of Amphotericin B loaded nanofibers .....	36
3.4.2	Heat induced stress test .....	36
3.4.3	Plate diffusion assay .....	37
3.4.4	Electron beam sterilization .....	37
3.4.5	Asymmetrical field-flow-field fractionation.....	38
3.4.6	Cytotoxicity <i>in vitro</i> : hTCEpi differentiation-assay .....	39
3.5	Ocular residence time <i>in vivo</i> .....	39
3.5.1	Optical coherence tomography .....	40
3.5.2	Pentacam® imaging.....	42
3.5.3	Tear pH measurement.....	43
3.5.4	Photographic pictures .....	43
3.6	Software .....	43
<b>4</b>	<b>Results and Discussion.....</b>	<b>44</b>
4.1	Formulation development and characterization .....	44
4.1.1	Rheology of electrospinning solutions .....	44
4.1.2	Optical characterization of the electrospun products.....	47
4.1.3	Water content.....	51
4.1.4	Rheology of <i>in situ</i> gelled nanofibers.....	52
4.1.5	<sup>1</sup> H-nuclear magnetic resonance .....	55
4.1.6	Curvature formation .....	58
4.1.7	Nanoscale 3D x-ray imaging .....	59
4.1.8	Ocular residence time <i>in vitro</i> .....	62
4.2	Drug loaded electrospun nanofibers .....	69
4.2.1	Nanoparticle loaded nanofibers.....	69
4.2.1.1	Nanoparticle characterization.....	69
4.2.2	Eudragit L-Amphotericin B-polyelectrolyte complex.....	72
4.2.2.1	UV/Vis-spectroscopy .....	72

---

4.2.2.2	ATR-IR-spectroscopy .....	73
4.2.2.3	Drug content and zeta potential.....	75
4.2.2.4	X-ray powder diffraction.....	76
4.2.2.5	Differential scanning calorimetry .....	77
4.2.2.6	Heat induced stress test .....	79
4.2.3	Morphology and drug load of the electrospun nanofibers.....	80
4.3	Plate diffusion assay.....	84
4.4	Impact of e <sup>-</sup> -beam treatment.....	86
4.5	Cytotoxicity <i>in vitro</i> : hTCEpi differentiation-assay.....	88
4.6	Ocular residence time <i>in vivo</i> .....	90
4.6.1	Optical coherence tomography.....	91
4.6.2	Optical coherence tomography-fluorescence quantification .....	93
4.6.3	Pentacam <sup>®</sup> imaging.....	96
4.6.4	Nanofiber impact onto the physiological tear fluid pH .....	98
<b>5</b>	<b>Summary and Perspectives .....</b>	<b>100</b>
	<b>References .....</b>	<b>VI</b>
	<b>Appendices.....</b>	<b>XXII</b>
	<b>Deutsche Zusammenfassung .....</b>	<b>XXXIII</b>
	<b>Acknowledgements.....</b>	<b>XXXVIII</b>
	<b>Curriculum Vitae .....</b>	<b>XL</b>
	<b>List of Publications.....</b>	<b>XLI</b>
	<b>Selbstständigkeitserklärung .....</b>	<b>XLIII</b>

## List of Abbreviations and Symbols

% [m/m]	Percentage by weight
% [m/v]	Mass percentage by volume
°	Degree
°C	Degree celsius
$\delta$	Loss angle
$\mu$ l	Microliter
$\mu$ m	Micrometer
$\mu$ s	Microsecond
$\eta^*$	Complex viscosity
$2\theta$	Incident angle
2D	Two-dimensional
3D	Three-dimensional
3T3	3-day transfer, inoculum $3 \times 10^5$ cells
A4F	Asymmetric Flow Field-Flow Fractionation
AmpB	Amphotericin B
API	Active pharmaceutical ingredient
ATR-IR	Attenuated Total Reflectance - Infrared Spectroscopy
BAF	BluePeak blue laser autofluorescence
BCS	Biopharmaceutical Classification System
CAD	Computer-Aided Design
cm	Centimeter
d	Diameter
DiR	1,1'-Dioctadecyl-3,3',3'-Tetramethylindotricarbocyanine Iodide
DMSO	Dimethyl sulfoxide
DSC	Differential Scanning Calorimetry
DSMZ	German collection of microorganisms and cell culture GmbH
EDTA	Ethylenediaminetetraacetic acid
ESEM	Environmental Scanning Electron Microscopy
FA	Fluorescein Scanning Angiography
G	Gauge
$G'$	Storage modulus
$G''$	Loss modulus
g/l	Gram per Liter
GG	Gellan Gum
GSE	Gaseous Secondary Electron Detector
h	Hour
$^1\text{H-NMR}$	Proton Nuclear Magnetic Resonance
HA	High acetylated
HPLC	High Performance Liquid Chromatography
hTCEpi	Immortalized human corneal epithelial cell line
NHDF	Normal human dermal fibroblasts
Hz	Frequency
I	Intensity
IC <sub>50</sub>	Half maximal inhibitory concentration

---

log P	Octanol-Water coefficient/Partition coefficient
LVR	Linear viscoelastic region
K/min	Kelvin per Minute
K <sub>α</sub>	K alpha line
keV	Kiloelectronvolt
kGy	Kilogray
kDa	Kilodalton
kPa	Kilopascal
kPas	Kilopascalsecond
kV	Kilovolt
LA	Low acetylated
LVR	Linear viscoelastic region
M	Concentration (mol/l)
m <sup>2</sup> /s	Square meter per second
MALS	Multi Angle Light Scattering
mbar	Millibar
MeV	Megaelectronvolt
min	Minutes
ml	Milliliter
ml/h	Milliliter per hour
mm <sup>2</sup>	Square millimeter
Mpx	Megapixel
ms	Milliseconds
MSFI	Multispectral Fluorescence Imaging
nm	Nanometer
M <sub>w</sub>	Molecular weight
NTA	Nanoparticle Tracking Analysis
OCT	Optical Coherence Tomography
PCS	Photon Correlation Spectroscopy
PDI	Polydispersity index
PES	Polyethersulfon
Ph. Eur.	European Pharmacopeia
PLA	Polylactic acid
PLGA	Poly(lactic-co-glycolic acid)
PVA	Polyvinyl alcohol
rpm	Rotation per minute
s	Seconds
s <sup>-1</sup>	Shear rate
SAL	Sterility assurance level
SC	Sodium cholate
SEC	Size Exclusion Chromatography
STF	Simulated tear fluid
T <sub>1</sub>	Longitudinal relaxation time (spin-lattice)
T <sub>2</sub>	Transverse relaxation time (spin-spin)
T/m	Magnetic gradient strength (Tesla per meter)
T <sub>g</sub>	Glass transition temperature
Torr	Torr

## 1 Introduction

### 1.1 Ocular drug delivery

Ocular diseases like glaucoma, age related macular degeneration, edema or infections require effective pharmacological therapies and sufficient drug concentrations to ensure total patient recovery without remaining tissue damage. But the complex anatomy, histology and physiological clearance mechanisms of the eye make ocular drug delivery to one of the ambitious challenges in field of controlled release. The anatomic conditions of the human eye like fast tear turnover, blinking and lacrimation make the eye to a difficult field of application. Especially the low tear volume of 7-30  $\mu\text{l}$  and a turnover of 0.5-2.2  $\mu\text{l}/\text{min}$  provide effective clearance via nasolacrimal drainage. To overcome these effective clearance mechanisms often high doses and application frequencies of drugs were necessary, which may induce systemic absorption and side effects [1]. In addition to the continuous tear flow high shear stresses caused by a high lid blink frequency of 6-15 times/min induce efficient clearance of instilled drugs [1]. As consequence, aqueous drug solutions like Fluriprofen for example are cleared quickly after instillation. Only 16 % of the initial instilled drug remains at the cornea *in vivo* after 10 min. The effective ocular clearance decreases the bioavailability [2]. In addition to the physical clearance mechanisms, biological barriers like the cellular structure of the cornea with its multilayered structure, in combination with the covering tear film contribute to the prevention of the drug permeation into the segments of the eye. In Figure 1 a schematic illustration of the ocular barriers is displayed.

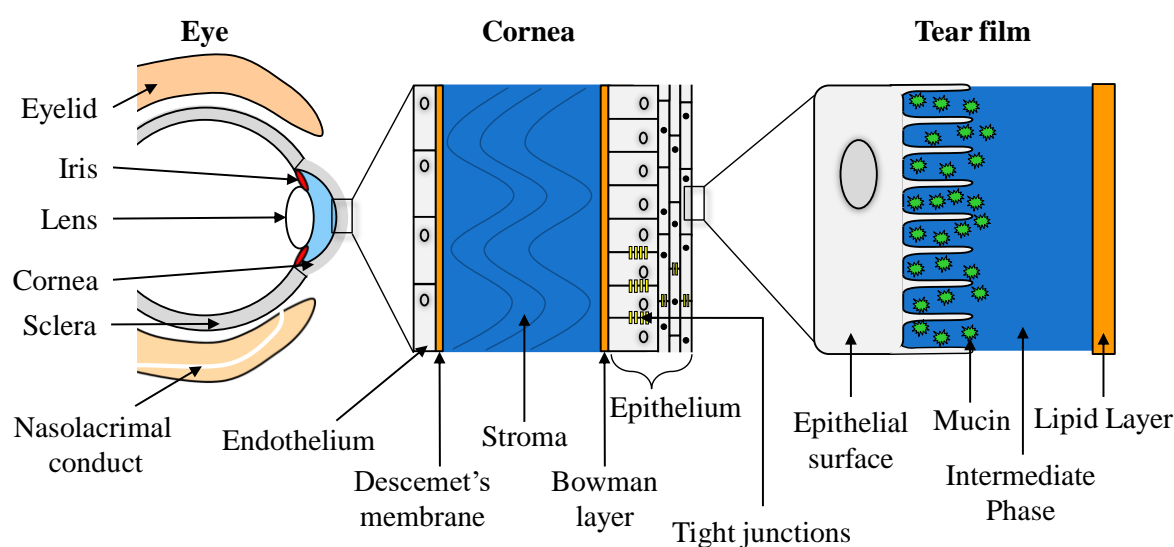


**Figure 1.** Schematic illustration of the physiological barriers of the human eye.



The first outer physiological barrier, which shields the eye from the external environment, is the tear film that covers the cornea. The tear film consists of three different liquid layers with varying physicochemical properties. The outer layer is based on hydrophobic properties containing polar and non-polar lipids like waxes, sterol esters, di-, triglycerides and hydrocarbons. This layer prevents tear fluid evaporation and ensures the moistening of the cornea surface [3,4]. The intermediate phase is characterized by high water content and contains osmotic active electrolytes, peptides and proteins like lysozyme and glycoproteins. Main function of the proteins is the defense from microbiotic pathogens. The enzymes and proteins, which are localized in the hydrophilic segments may induce degradation or inactivation of the drugs. The third layer which is next to the cornea surface is based on mucin, a glycosylated protein, which ensures cornea lubrication and epithelium protection [3]. Each layer of the tear film is characterized by alternating polarities and contributes to reduction of drug permeation. The tear film covers the translucent, non-vascular cornea, which allows light transmission into the eye. The cornea thickness is about 500-600  $\mu\text{m}$  [5–7]. The cornea has a multilayered structure as well and consists of a hydrophobic epithelium, a hydrophilic stroma and a hydrophobic endothelium to prevent penetration of exogenous substances and microorganisms. The corneal tissue is built of epithelial cells, keratocytes (corneal fibroblasts) and endothelial cells. The tear film covered epithelium is made of stratified squamous cell layers, which are joined by tight junctions [2,8]. In the cornea center the epithelial cells are stratified in 5-7 cell layers. The cells at the basal site become a flattened shape during the differentiation process. Furthermore, to the histological barriers cellular mechanisms like cytochrome P450 and efflux pumps are localized in the epithelium and contribute to the decrease of bioavailability of instilled drugs as well [9,10]. The epithelial layer is bordered by the Bowman layer from the stroma. The stroma, covered by the epithelium, contains collagen fibrils and is highly hydrated which induce the barrier for lipophilic drugs. The Descemet's membrane borders the hydrophilic stroma from the covered endothelium. In contrast to the epithelium, the endothelium consists as a cellular monolayer, which allows more permeation of macromolecules between the aqueous humor and the stroma. The totality of the described physiological barriers makes ocular drug delivery to a high challenging task. Nevertheless, ocular diseases like glaucoma, diabetic retinopathy, age-related macular degeneration or ocular infections like keratomycosis require efficient drug delivery systems for a total patient

recovery. In summary, for ocular drug delivery, there is a mismatch between the high medical need and the overall poor performance.

Drug delivery systems prepared for ocular therapy are known under the term ophthalmica. The European Pharmacopeia (Ph. Eur.) specifies ophthalmica as “...*sterile liquid, semi-solid or solid preparations intended for administration upon eyeball and/or to the conjunctiva, or for insertion in the conjunctival sac*” (Pharmacopoea Europaea 10.0, S. 909). The Ph. Eur. differentiates ophthalmica into:

- » Eye drops
- » Eye lotions
- » Powders for eye drops / eye lotions
- » Semi-solid eye preparations
- » Ophthalmic inserts

Different safety requirements are ensured by the Ph. Eur. specifications to avoid ocular irritations and damage. Ophthalmica have to comply with several quality aspects, they have to be sterile, isotonic, euhydic and the size of the containing particles is restricted. The amount of 10 µg drug containing formulation does not allow more than 20 particles larger than 25 µm, maximum 2 particles exceeding 50 µm and no particle must be larger than 90 µm.

In general, ophthalmica can be applied topical to the ocular surface or can be injected directly into the bulb, to treat the anterior or posterior segment of the eye. Dorzolamide hydrochloride for example, a commonly used antiglaucoma active pharmaceutical ingredient (API) reaches therapeutic concentrations in the anterior as well as in the posterior segment after topical instillation as eye drops [11]. Different drug delivery systems were developed to handle the low drug bioavailability in field of pharmaceutical technology. Figure 2 illustrates an overview about the developed drug delivery system, differentiated into fluid, solid and semi-solid formulations.

Fluid systems like aqueous or oily eye drops allow a comfortable application with a low-cost production and achieve a high patient compliance. On the other hand, these systems are characterized by fast ocular clearance and a reduced bioavailability of the instilled drugs. In

addition many drugs are insoluble in aqueous media and need a solubilisation increase via surface active ingredients, cyclodextrins, liposomes or nanotechnology [12–14].

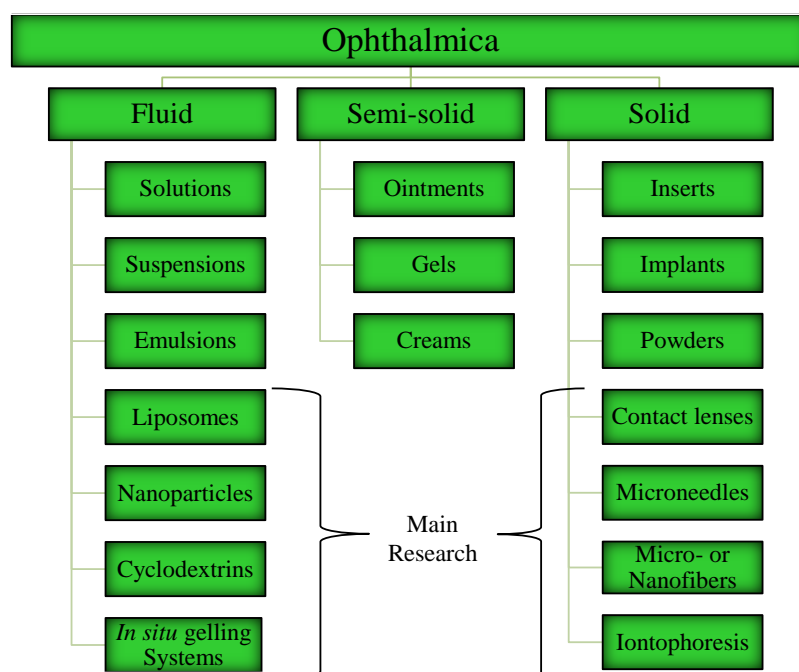


**Figure 2.** Overview about drug delivery systems for ocular use.

Solid dosage forms like inserts or implants were placed directly into the bulb or into the cul-de-sac and allow drug release over a prolonged period. These systems are characterized by a reduced patient compliance and a more invasive application [15]. Due to their solid state and the absence of water in these systems, they do not need any preserving agents to ensure safe microbiotic conditions. Furthermore, these systems are appropriate for drug delivery of hydrolytic sensitive drugs. Solid systems which were placed in the cul-de-sac like the market product Lacrisert<sup>®</sup>, a water soluble hydroxypropyl cellulose based system which is used for the dry eye syndrome, increases the ocular residence time, but has higher eye irritation potential triggered by the solid character. A new field of research is the use of microneedle patches as minimally-invasive drug delivery system for the posterior eye segment. Therefore, needles with a size of 500-750  $\mu\text{m}$  were coated with drugs and were inserted into the cornea *in vivo*, the length of the microneedles is sufficient to penetrate human sclera and to deliver the drug into the aqueous humor of the eye. Microneedles are more efficient for drug delivery to the posterior eye segment compared to conventional eye drops [16]. On the other hand, the treatment with microneedles might induce microdamage at the ocular tissue and cicatrizations over longer period. Another field of research is about

drug loaded contact lenses applied to the ocular surface. But several challenges occur during the development process of these polymer systems (e.g. hydroxyethylmethacrylate based systems), for example sustained drug release, drug load, visual transparency or sufficient oxygen permeability [17–19]. Furthermore, investigations of patches consisting polymeric micro-or nanofibers prepared by electrospinning are promising candidates for ocular drug delivery as well. The electrospun meshes seem as suitable systems for increasing ocular bioavailability, because of a high sample porosity, a high surface area with an adjustable layer thickness and various use of polymers combined with a sustained release [20–23].

Another approach to overcome the physiological barriers of the eye is the iontophoresis technology as a non-invasive method. The electroosmotic based systems induce the permeation of ionized drugs under the influence of an electric field into the ocular tissue and increase the drug bioavailability. The iontophoretic devices consists of two electrodes, one inside a cup shaped applicator, the other one can be placed, for example, on the forehead of a patient. The system contains also an eye cup for the drug formulation and a power supply. The cup shaped applicator is directly placed onto the eye surface. The drug can be applied as hydrogel or solution into the cup reservoir. Triggered by the influence of an external electric field the drugs are able to penetrate into the an- and posterior eye segment. Iontophoresis is an effective method to increase the bioavailability of hydrophilic, charged drugs. However, the electricity treatment often feels uncomfortable for the patients and can induce epithelial edema, inflammatory infiltrations and damages of the cornea. Electroosmotic systems are mainly limited to charged drugs and cannot be transferred to neutral molecules [24].

It is well known that the adjustment of the formulation viscosity induce higher bioavailability of the applied drugs [25,26]. Therefore, semi-solid dosage forms like ointments, gels and creams with a prolonged residence time were developed and are commonly used. However, lipid containing formulations like vaseline based systems cover the ocular surface and might lead to insufficient oxygen supply. Furthermore, the lipid based semi-solid systems cause a blurred vision after application, which contributes to a decreased patient compliance. In contrast to those lipid based systems, hydrogel formulations, for example based on polyvinylpyrrolidone, hyaluronic acid or poly(acrylic acid), show sufficient oxygen supply combined with an increased ocular residence time and less blurred sight. The increased water content of these systems needs the addition of preserving agents to ensure the sterile state of

the formulations during storage, but many of the used agents like thiomersal or benzalkonium chloride/EDTA have higher irritation potential. Because of this, these formulations were low accepted by the patients and cannot be used after chirurgic treatment of the eye. Alternatively, preserving agents and more expensive packaging techniques like single-dose containers or the continuous mono dose systems (COMOD) can be utilized to ensure sterile instillation and storage of the formulation. During the last decades, researchers focused more and more on *in situ* gelling systems. These systems combine the advantages of liquid formulations like easy application and high patient compliance with an increased viscosity of semi-solid systems after eye contact. The liquid character of the systems allows sterile filtration to ensure aseptic conditions. The *in situ* gelling systems underlie a sol-gel transition under influence of environmental stimuli. Different gel forming mechanisms during *in situ* gelation were discussed [27–31]:

- » **Thermo-responsive gelling systems:** Temperature shift from room temperature (sol) to the eye temperature 34 °C (gel) induce gel formation. During the process the polymer hydrophobicity increased by rising polymer entanglements and hydrogen bond formation (Ploxamer 188, Ploxamer 407).
- » **Ion-responsive gelling systems:** Electrostatic interaction of the polymer functions with mono-or divalent cations in the tear fluid. Physical crosslinking of the polymer chains by electrostatic interactions (Gellan Gum, Alginate).
- » **pH-responsive gelling systems:** Dissolved polymer at acidic/basic environment, which forms gels at physiological pH 7.4. Gel formation dependents strongly from  $pK_a$  of the used polymer (Poly(acrylic acid), Chitosan).
- » **Covalently binding systems:** Formation of covalent bonds between physiologic mucus proteins and the polymer, as well as between the polymer chains (Chitosan N-acetylcysteine, Chitosan–thioglycolic acid).
- » **Multi-stimuli-responsive gelling systems:** Combination of more than one gelling mechanism (Ploxamer 188 in combination with Alginate).

Especially the thermo-responsive gelling systems are not suitable for the therapy in summer or in hot countries, because the gelation takes places before instillation into the eye. Each of the described mechanisms needs sufficient solubility and hydrolytic resistance of the drugs,

caused by the aqueous environment of the solvent. Hence, the storage stability of often used drugs is limited. For example Latanoprost which is used for common glaucoma therapy shows intense degradation during storage at higher temperatures in aqueous solution [32].

Another described *in situ* gelling technology to prolong the ocular residence time is utilization of thiolated polymers like chitosan-cysteine, alginate-cysteine or chitosan 4-thio-butyl-amidine conjugates. The thiol functions of the polymers are able to form disulfide bonds with cysteine rich subdomains of the mucus glycoprotein thiol components [31,33,34]. The formed disulfide bonds are reversible by physiologic redox reactions and cause decrease of the irreversible cytotoxic bond formation. Lacrimera<sup>®</sup> which is a first system based on chitosan N-acetylcysteine is available on the market to treat the dry eye syndrome. Once a day application over 5 days provide increase of tear film stability and reduce the patient dry eye symptoms for 30 days and more [35]. Thiomer based systems have to be preserved in multi-dose containers like conventional eye drops to prevent microbiological contamination. In addition, the oxidation potential of the thiol functions in liquid state has to be seen critical and the formulation conditions have to be adjusted. During storage the polymer itself is able to react with each other and gel formation is induced by oxidation. Furthermore, the reactive thiol functions of the polymer are able to react with thiol groups of drugs, what result mostly in inactivation of the API and a reduce gel forming capacity. Until the present day the *in situ* gelling systems are the most promising formulation techniques for efficient drug delivery, but no *in situ* gelling system was developed, which combines temperature independent, ion sensitive gelation with a preservation- and water free formulation technique to overcome the described problems.

To get an overview about available marketed systems, different drug delivery systems are presented in Table 1 with the correlating API and indication. The listed systems are categorized into ointments, eye drops, implants, injections, inserts and other applications.

**Table 1** Examples of approved ophthalmics for the treatment of anterior and posterior segment diseases.

	Product	API <sup>a</sup>	Remarks	Indication
Ointment	Parin-POS <sup>®</sup>	Heparin sodium	Vaseline, paraffin wax based	Eye irritations
	Acic <sup>®</sup> -Ophthal	Aciclovir	Vaseline based	Viral Keratitis
Eye drops	Voltaren <sup>®</sup> ophtha	Diclofenac sodium	2-Hydroxypropyl cyclodextrine based	(Postoperative) Inflammation
	Tears Again <sup>®</sup>	Soy lecithin	Liposomal spray	Dry eye syndrome
	VisuXL <sup>®</sup>	Coenzyme Q10	<i>In situ</i> gelling system (Poloxamer 407 based)	Dry eye syndrome
	Lacrimera <sup>®</sup>	Chitosan N-acetylcysteine	Long acting, Chitosan N-acetylcysteine	Dry eye syndrome
	Timoptic XE <sup>®</sup>	Timolol maleate	<i>In situ</i> gelling system (Gellan Gum based)	Glaucoma
	Moxeza <sup>®</sup>	Moxifloxacin-HCl	<i>In situ</i> gelling system (Gellan Gum based)	Bacterial conjunctivitis
Implant	Vitrasert <sup>®</sup>	Ganciclovir	Intravitreal, Ethylene Vinyl acetate based	Cytomegalovirus retinitis
	Ozurdex <sup>®</sup>	Dexamethasone	Intravitreal, PLGA <sup>b</sup> (50:50) based	Macula oedema
Injection	Lucentis <sup>®</sup>	Ranibizumab	Antibody injection	Macular degeneration
Insert	Mydrasert <sup>®</sup>	Tropicamide, Phenylephrine-HCl	Ammonium Methacrylate Copolymer (Typ A)	Preoperative mydriasis
	Lacrisert <sup>®</sup>	HPMC <sup>c</sup>	Water soluble HPMC <sup>c</sup>	Dry eye syndrome
Other	Visulex-I	Macromolecules (Bevacizumab)	Iontophoretic device; (Clinical Phase)	Macular degeneration

<sup>a</sup> Active Pharmaceutical Ingredient<sup>b</sup> Poly(D,L-Lactid-co-Glycolid)<sup>c</sup> Hydroxypropyl methylcellulose

## 1.2 Fungal keratitis

Fungal infections of the ocular surface and the anterior eye segment are known as fungal keratitis or keratomycosis, caused by fungal inoculation of the ocular tissue [36]. Untreated infections lead to increasing perforation of the cornea structure, tissue damages and finally require often corneal transplantation to maintain visual sight. Hence, an early and precise diagnose as well as differentiation from bacterial infection and inflammation are necessary to prevent the dramatic progress and consequences of the non-treated disease. Adequate therapy with suitable drugs and dosage forms requires exact determination of the fungal species to ensure total patient recovery. In epidemiologic investigations, an increased keratitis incidence was found in countries with tropical climate paired with low-incoming regions in comparison to industrial countries [37–39]. In Germany, 102 patients were diagnosed with a fungal keratitis in the years 2000 to 2017. 65.7 % of these patients needed a keratoplastic surgery, because of a late diagnose and ineffective pharmacologic therapy [40]. It was found that 57 % of the fungal keratitis patients wore contact lenses, 30 % of these had an eye operation previously and 19 % had jobs in the agriculture or gardener sections [40]. Different fungal species like *Fusarium spp.*, *Candida spp.* and *Aspergillus spp.* were determined to be the most pathogens causing fungal infections of the eye [41]. In Figure 3 two different pictures of keratomycosis are displayed. A) Shows an *Aspergillus fumigatus* infection after foreign body injury and B) an *Candida albicans* infected corneal graft [42]. Typical symptoms are redness, pain, ring infiltration, brown-orange pigmentation, hypopyon and fungal satellites from the cornea surface into deeper cellular layers.

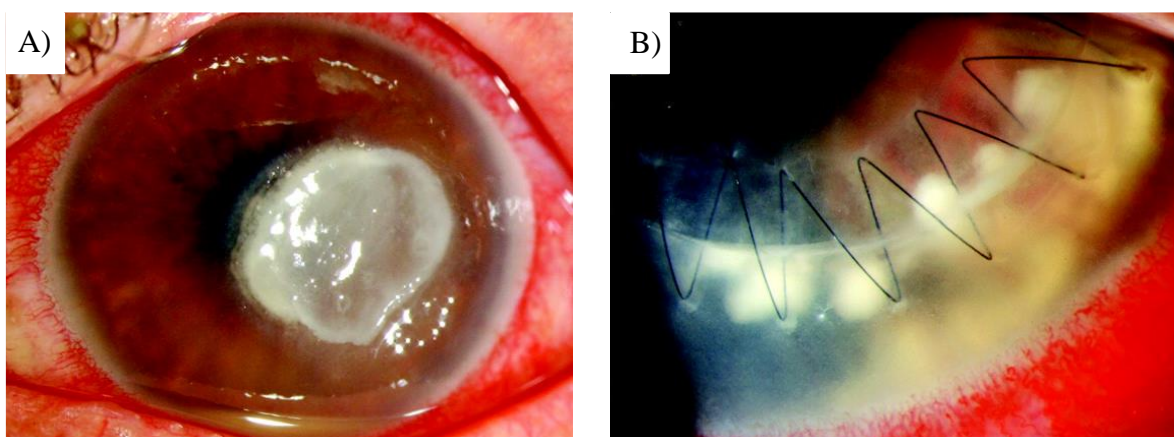


**Figure 3.** Photographic pictures of keratomycosis: A) *Aspergillus fumigatus* infection after a corneal foreign body injury; B) *Candida albicans* infected corneal graft [42].



The keratomycosis therapy is characterized by high application frequency in combination with high doses to reach complete patient recovery. Amphotericin B (AmpB) and Voriconazole used as single or multi-drug therapy are the most common active ingredients for topical or anterior treatment [40,43,44]. The therapy with AmpB eye drops for example is characterized by 1 hourly application to the infected eye, reason is the rapid ocular clearance and low bioavailability of the drug [43]. This underlines the high application effort, which is necessary to ensure efficient recovery of the patient. Until the present day, no commercial therapy of antimycotic drugs for efficient treatment of ocular infections is available. Mostly drug formulations like Fungizone<sup>®</sup>, a bile salt containing AmpB infusion, are used off-label in therapy. Low AmpB bioavailability and high cellular toxicity reduces the chances for total patient recovery without cornea transplantation and make the keratomycosis to a severe disease.

### 1.3 Research objectives

Within the last 20 years the importance of ocular drug delivery and electrospinning as preparation technique is still increasing. New geometries of the electrospun fibers paired with modified release profiles and physicochemical properties make electrospun meshes interesting as new drug delivery system, especially for the field of fungal keratitis. Many researches dealing with the previous described problems of ocular drug delivery and have to overcome the challenges of low bioavailability.

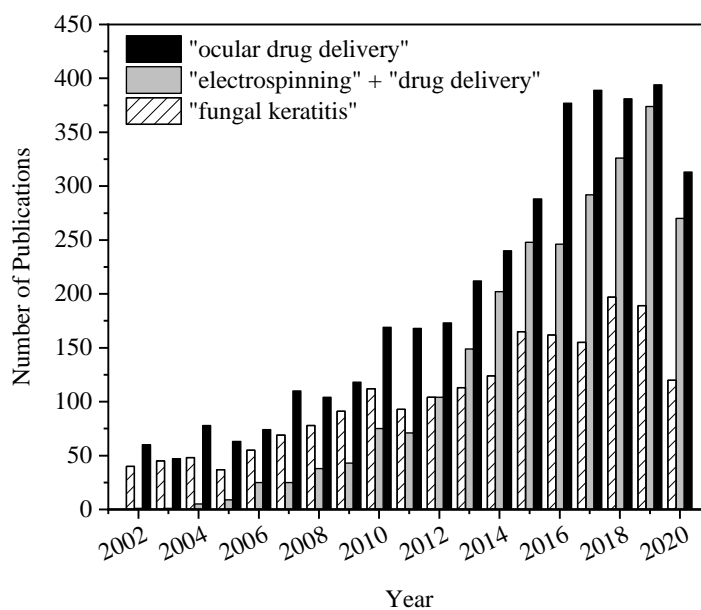


**Figure 4.** Results of webofknowledge literature research for the terms “ocular drug delivery”, “electrospinning+ drug delivery” and “fungal keratitis” from 2002 to 2020 (date 18.09.2020).

Figure 4 illustrates the number of publications during last 20 years in these fields of research, which underline the topicality of the discussed topic. Aim of the present work was the development and physicochemical characterization of a new *in situ* gelling nanofiber based system. Gellan Gum as cation sensitive gelling agent should be used as gelling ingredient. The system must be suitable for treatment of fungal keratitis to reach an improvement of the common therapy. Therefore, AmpB as gold standard antimycotic drug has to be used as API. The developed systems should be investigated in detail, including the following quality aspects:

- » Solid, *in situ* gelling system, based on polymer nanofibers. The system has to be non-toxic and suitable for topical ocular drug delivery.
- » Detailed physicochemical characterization *in vitro* of the developed drug delivery system.
- » Prolongation of the ocular residence time compared to conventional eye drops.
- » Adaptation of the drug delivery system geometry to the anatomical conditions of the human eye.
- » Sufficient encapsulation and maintaining the bioactivity of AmpB to inhibit the growth of fungal microorganisms to improve the conventional keratomycosis therapy.
- » Performance of *in vivo* experiments for potential formulations.

To facilitate the understanding and progression of the research Figure 5 displays an overview about the performed experiments and utilized methods, which were used during the present PhD thesis. The scheme differentiates the performed experiments in drug free and AmpB loaded fibers. For AmpB encapsulation into the fibers different techniques were used. Sodium cholate, nanoparticles and a polyelectrolyte complex formulation were utilized.

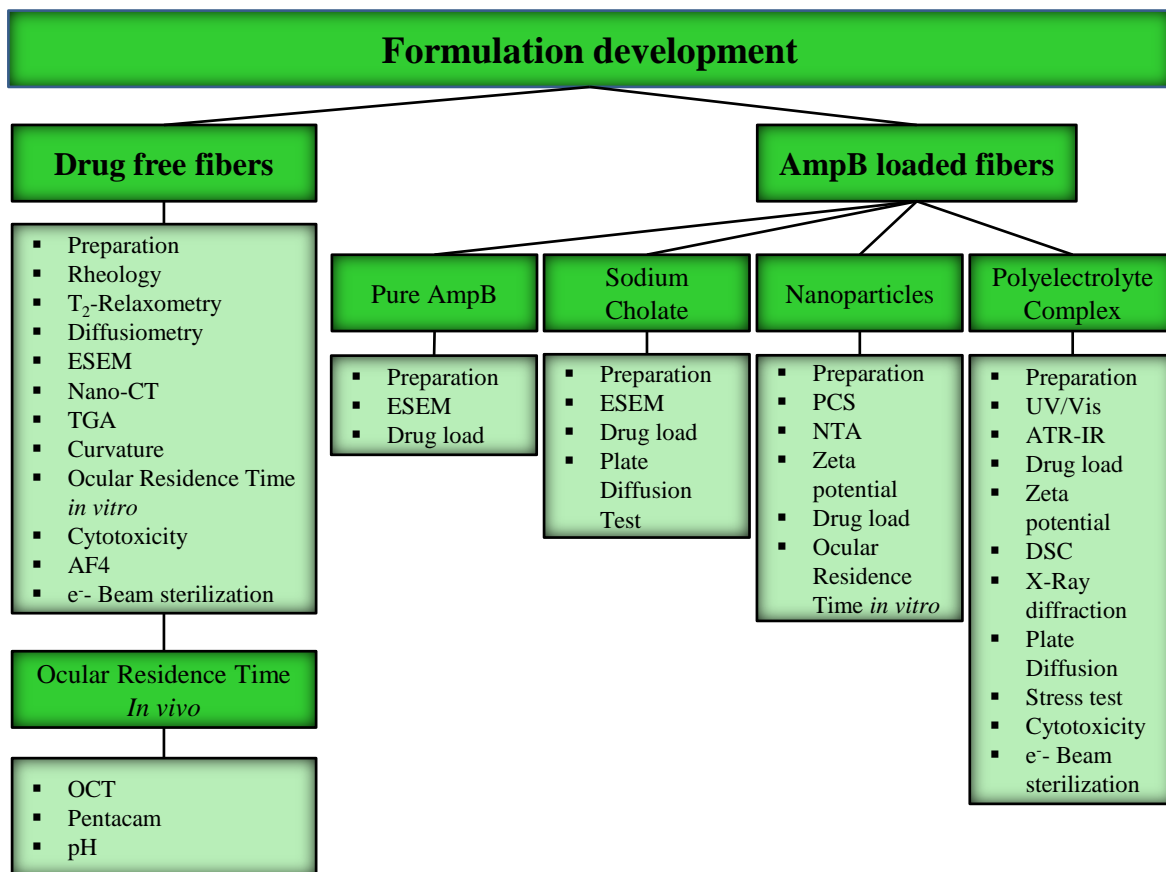


Figure 5. Schematic structure and overview about the experimental part of the thesis.

## 2 Materials

### 2.1 Polymers

#### Gellan Gum

Gellan Gum is a brown, orange multifunctional, water-soluble hydrocolloid that has been used since decades in food technology, which is able to form hydrogels [45]. Utilization as gelling agent make the polymer more and more interesting for different fields of application like tissue engineering and drug delivery [46,47]. Gellan Gum is a negatively charged tetrasaccharide produced by the bacteria *Pseudomonas elodea* and consist of two units of  $\beta$ -D-glucose, one of  $\beta$ -D-glucuronate and one of  $\alpha$ -L-rhamnose [48]. Further, the native polysaccharide is characterized by O-acetyl and glyceryl side chains of the glucose units. By variation of the acetylation degree Gellan Gum has to be differentiated into low (LA) and high (HA) acetylated grades. As consequence of these chemical modifications the gel properties like gel strength, texture and appearance change. The detailed chemical structure of low and high acetylated Gellan Gum is illustrated in Figure 6.

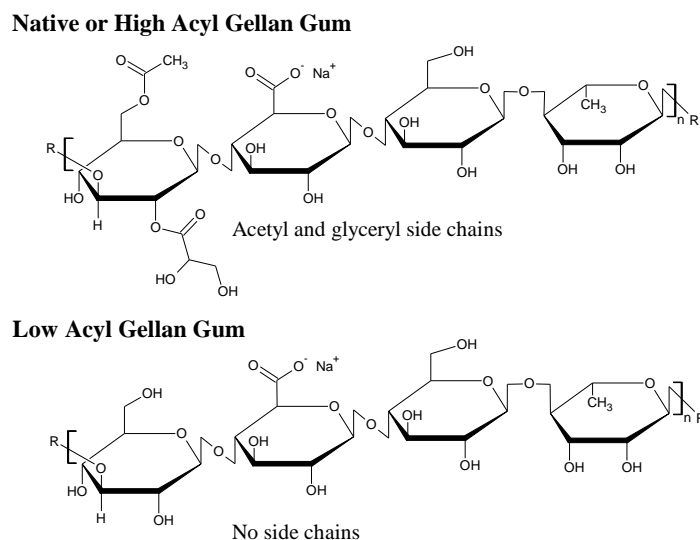


**Figure 6.** Chemical structure of high acyl (HA) and low acyl (LA) Gellan Gum derivatives.

Gellan Gum belongs to the ion-responsive gelling agents and the mechanism is based on interaction with mono- and divalent cations. Hydrogels formed by Gellan Gum with a higher degree of acetylation are soft, flexible and opaque. A lower acetylation degree results in more firm, brittle and transparent gels [49]. In contrast to low acetylated Gellan Gum (LA), the high acetylated derivate does not require cations for gel formation. In aqueous media, low concentrations of Gellan Gum LA are characterized by fluid flow properties in the

absence of cations. After cation contact the sol underlies gel formation. Especially this behavior made Gellan Gum interesting for *in situ* gelling systems. The gel strength can be adjusted by increase the polymer or cation concentration, as well as the cation type [50].

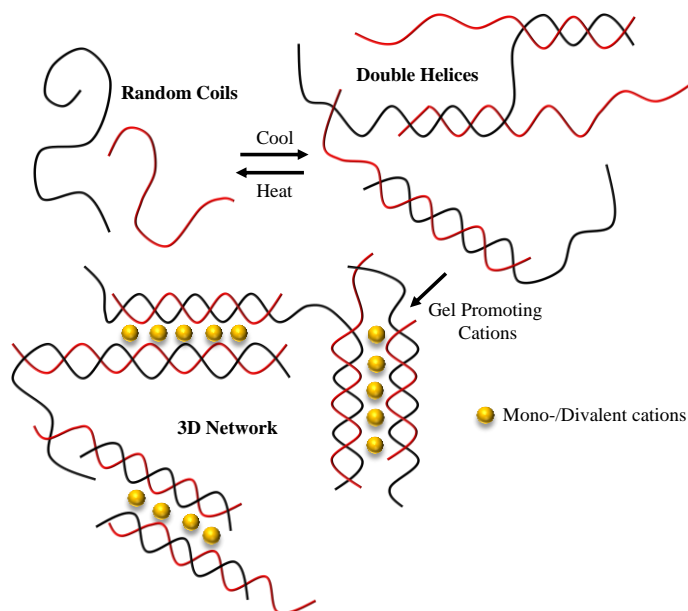


**Figure 7.** Schematic gelation model of Gellan Gum in presence of mono- or divalent cations.

The gelling mechanism of Gellan Gum is based on a cation induced formation of double stranded helices, dependent from the applied temperature. The gelling mechanism is illustrated in Figure 7. Under influence of heat the polymer starts hydration and formation of random coils. Triggered by cooling the random coils convert into 3-fold double helices and allow gel formation with or in absence of cation contact. The cation induced aggregation of the formed helices ensure gel formation [51]. During the present PhD thesis only low acetylated Gellan Gum was used.

### Pullulan

Pullulan is non-colored, white hygroscopic, water-soluble polymer. It is a non-toxic linear polysaccharide synthesized by *Aureobasidium pullulans*. The chemical structure of Pullulan is characterized by three glucose units which are connected as maltotriose by  $\alpha$ -(1 $\rightarrow$ 4) glycosidic bonds. The maltotriose units are connected by  $\alpha$ -(1 $\rightarrow$ 6) linkages [52,53]. The detailed chemical structure is displayed in Figure 8. Pullulan is often used in the food industry or in the field of pharmaceutical technology and is characterized by its excellent film forming properties [54–57]. In food industry the polymer is utilized for food texturing and coatings in fruit preservations. Pullulan cannot be digested by human enzymes

[58,59]. In fields of pharmaceutical technology Pullulan is used as solid non-permeable oxygen barrier, as fast dissolving film ingredient and as vegan capsule material [60–62].

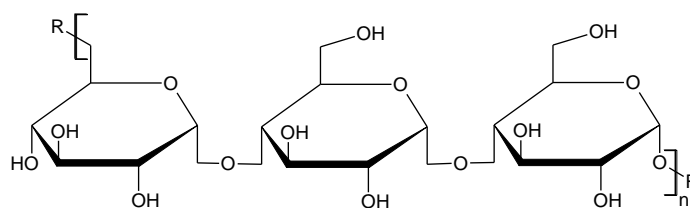


**Figure 8.** Chemical structure of Pullulan.

## 2.2 Active pharmaceutical ingredient

In progress of the present PhD thesis AmpB was used as API. AmpB is a yellow-orange powder and belongs to the polyene antifungal drugs with a molecular weight of 924 g/mol [63]. The API is produced by *Streptomyces nodosus* and is characterized by its strong antifungal activity. AmpB is the gold standard broad spectra antimycotic to inhibit different *Candida*, *Aspergillus* and *Fusarium species* [64]. AmpB is commonly used for the therapy of fungal infections or parasite diseases like leishmania. The antimycotic efficacy is based on binding to the ergosterol in the fungal cell membrane, followed by pore formation. The cell death is induced via the formed transmembrane channel since the cell loses intracellular ions like sodium, potassium and magnesium. The high therapeutic efficacy of AmpB, is unfortunately, often connected with serious side effects like nephrotoxicity, renal impairment, hypokalemia and acidosis during patient treatment [65,66]. Hence the intravascular application of AmpB has to be monitored intensively.

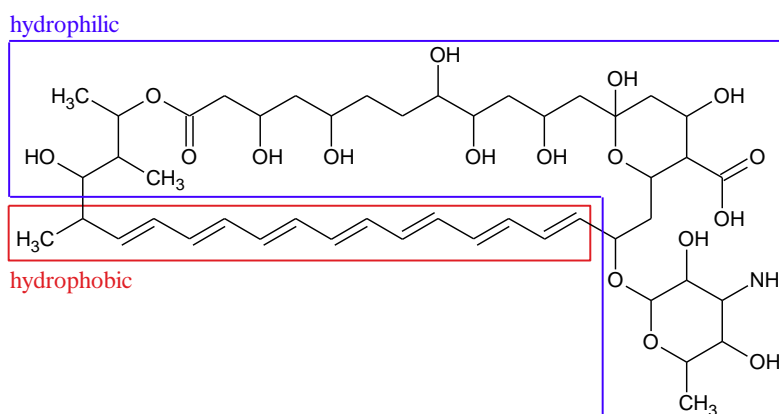


**Figure 9.** Chemical structure of Amphotericin B with highlighted hydrophilic (blue) and hydrophobic (red) molecular regions [67].

In Figure 9 the chemical structure of AmpB is displayed: The structure underlines the amphiphilic behavior of the drug, which is caused by the polar polyol side chain, lactone ring and the hydrophobic polyene chain. Furthermore, AmpB is characterized by amphoteric behavior, induced by the amine and carboxylic function, which contribute to the sparingly solubility of the drug in the most common solvents. AmpB is poorly soluble in water (< 1 µg/ml, pH 6-7) and in the most organic solvents [68,69]. In Table 2 an overview about the AmpB solubility is given. Because of the low solubility and low permeability of AmpB, the molecule belongs to the Biopharmaceutical Classification System (BCS) class IV.

**Table 2.** Solubility of Amphotericin B in different solvents [68–70].

Solvent	Solubility [µg/ml]
Water (pH 6-7)	< 1
Dimethylformamide	2
Chloroform	100
Ethanol	500
Methanol	2000
Dimethyl sulfoxide	30000-40000

Induced by the amphiphilic and amphoteric character, AmpB is able to form different states of aggregation depended on the used concentration. A monomeric, dimeric and poly-aggregated form can be observed. The occurred aggregation state can be easily determined using spectrophotometry, because the absorption spectrum shows characteristic shifts to other extinction maxima depending on the molecular organization. The monomeric form is characterized by three extinction maxima at 406, 383 and 363 nm. In contrast to the monomer, the dimeric form is characterized by extinction maximum at 328-340 nm [71,72]. The poly-aggregated form is recognized by low extinction maxima at 406-420 nm, 383-385 nm and 360-363 nm [68].

### 2.3 Further excipients and materials

**Table 3.** Further excipients, their source and remarks used for the described experiments.

<b>Substance</b>	<b>Source</b>	<b>Remark/Purity</b>
<b>Acetone</b>	VWR, Germany	Purity $\geq$ 99.5 %
<b>Acetonitril</b>	VWR, Germany	Purity $\geq$ 99.95 %
<b>Agar-Agar, Kobe 1</b>	Carl Roth, Germany	Density 0.55
<b>Amphotericin B</b>	Fagron, Germany	Purity 909 I.U./mg
<b>Aqua bidest.</b>	Institute of Pharmacy Martin Luther Universität Halle-Wittenberg, Germany	Produced by double distillation
<b>Calcium chloride</b>	Grüssing, Germany	Purity 99 %
<b>Calcium chloride*2H<sub>2</sub>O</b>	Carl Roth, Germany	Purity $\geq$ 99 %
<b>Dimethyl sulfoxide</b>	Carl Roth, Germany	Purity $\geq$ 99.8 %
<b>DiR<sup>a</sup></b>	ThermoFisher Scientific, U.S.	Fluorescence Dye for MFSI
<b>Disodium EDTA<sup>b</sup></b>	Fluka Analytical, Switzerland	Purity $\geq$ 98.5 %
<b>Disodium phosphate</b>	Grüssing, Germany	Purity 99 %
<b>DMEM<sup>c</sup></b>	Sigma Aldrich, Germany	Dulbecco`s Modified Eagle`s Medium – high glucose
<b>Eudragit L100</b>	Evonik, Germany	Batch: B161103024
<b>Emprove 5-88</b>	Merck, Germany	Hydrolysis 88%
<b>Fluorescein ALCON 10 % Injektionslösung</b>	Alcon Pharma, Germany	Content: 10 %
<b>Fluorescein sodium</b>	Carl Roth, Germany	Charge: 2966247190
<b>Glucose*Monohydrate</b>	Grüssing, Germany	99 %
<b>Hydrochloric acid</b>	Grüssing, Germany	Purity 37 %
<b>Kelcogel CG-LA</b>	CP Kelco, U.S.	Lot. 4D9106A
<b>KGM-2 Bullet Kit</b>	Lonza, Switzerland	Cytotoxicity
<b>Malt extract</b>	Carl Roth, Germany	Plate diffusion assay
<b>Methanol</b>	VWR, Germany	Purity $\geq$ 99.8 %
<b>Monopotassium phosphate</b>	Grüssing, Germany	Purity 99 %
<b>Penicillin-Streptomycin</b>	Sigma Aldrich, Germany	Penicillin 10.000 U/ml Streptomycin 10 mg/ml
<b>Tryptone/Peptone from casein</b>	Carl Roth, Germany	Plate diffusion assay
<b>Potassium chloride</b>	Grüssing, Germany	Purity 99 %
<b>Pullulan</b>	Hayashibara, Japan	Pharmaceutical excipient
<b>Resazurin sodium salt</b>	Sigma Aldrich, Germany	Cytotoxicity assay



<b>Resomer RG 502</b>	Evonik, Germany	Lot. 1052815
<b>Sodium azide</b>	Carl Roth, Germany	Purity $\geq$ 99 %
<b>Sodium bicarbonate</b>	Grüssing, Germany	Purity 99 %
<b>Sodium chloride</b>	Grüssing, Germany	Purity 99.5%
<b>Sodium cholate</b>	Sigma Aldrich, Germany	Purity $\geq$ 99 %
<b>Sodium hydroxide</b>	Carl Roth, Germany	Purity $\geq$ 99 %
<b>Sodium pyruvate</b>	Sigma Aldrich, Germany	11 mg/ml
<b>Triton X-100</b>	Sigma Aldrich, Germany	Cytotoxicity assay
<b>Yeast extract</b>	Carl Roth, Germany	Plate diffusion assay

<sup>a</sup> 1,1-dioctadecyltetramethyl indotricarbocyanine iodide

<sup>b</sup> Ethylenediaminetetraaceticacid disodium magnesium salt

<sup>c</sup> Dulbecco's Modified Eagle's Medium

## 2.4 Biological materials

**Table 4.** Further biological materials used for the described experiments.

<b>Substance</b>	<b>Source</b>	<b>Remark</b>
<b>3T3<sup>a</sup></b>	Thomas Groth (MLU Halle)	Cytotoxicity assay
<b>hTCEpi<sup>b</sup></b>	Evercyte, Austria	Cytotoxicity assay
<b>Issatchenika orientalis</b>	DSMZ, Germany	Plate diffusion test
<b>NHDF<sup>c</sup></b>	Thomas Groth (MLU Halle)	Cytotoxicity assay
<b>Porcine eyes</b>	Tönnies Zerlegebetrieb, Germany	Ocular residence time <i>in vitro</i>

<sup>a</sup> 3-day transfer inoculum  $3 \times 10^5$  cells (murine Fibroblasts)

<sup>b</sup> Immortalized human corneal epithelial cell line

<sup>c</sup> Normal Human Dermal Fibroblasts

## 2.5 Miscellaneous laboratory equipment

**Table 5.** Further laboratory equipment with their sources and remarks for the described experiments.

<b>Substance</b>	<b>Source</b>	<b>Remark</b>
<b>Amicon<sup>®</sup> Ultra 100 kDa</b>	Merck, Germany	Purification; 15 ml
<b>Blema Strip<sup>®</sup></b>	Aristo, Germany	Human experiments pH
<b>Caps</b>	VWR, Germany	8 mm; 13 mm; Orifice central; closed top
<b>Cellstar<sup>®</sup> Tubes</b>	Greiner bio-one, Germany	15 ml; PP <sup>a</sup>

---

<b>Centrifugal Tubes</b>	VWR, German	50 ml; PP <sup>a</sup>
<b>epT.I.P.S.<sup>®</sup> Standard</b>	Eppendorf, Germany	50-1000 µl; 1-10 ml
<b>Gastight<sup>®</sup> Syringes</b>	Hamilton, Germany	1 ml; glass
<b>Gewindeflaschen Brown</b>	VWR, Germany	1.5 ml; 4 ml; glass
<b>Injekt<sup>®</sup>-F</b>	B. Braun, Germany	1 ml
<b>Micro-Insert</b>	VWR, Germany	0.1 ml; 30x5mm
<b>Nadir<sup>®</sup> Dialysis Tubing 10-20 kDa</b>	Carl Roth, Germany	Dialyses/Purification
<b>Reaction Tubes</b>	Greiner bio-one, Germany	1.5 ml; 2 ml
<b>Septums</b>	VWR, Germany	8 mm; 12 mm; Silicone/PTFE <sup>b</sup>
<b>Sterican cannulas</b>	B. Braun, Germany	23 G x 3 1/8''
<b>Sterile Filter</b>	VWR, Germany	Material: PES <sup>c</sup>
<b>ThinCert</b>	Greiner bio-one, Germany	0.4 µm
<b>Universal yellow tips</b>	VWR, Germany	2-200 µl
<b>Well plate</b>	Greiner bio-one, Germany	24 wells, 96 wells

---

<sup>a</sup> Polypropylene

<sup>b</sup> Polytetrafluorethylene

<sup>c</sup> Polyethersulfone

## 3 Methods

### 3.1 Formulation development and characterization

#### 3.1.1 Rheology

##### Rotation rheology of electrospinning solutions

The rheological experiments of the spinning solutions were carried out in the rotation mode of the Kinexus lab+<sup>®</sup> (Malvern, Kassel, Germany). All measurements were performed at 20 °C in a shear rate range of 1-1000 s<sup>-1</sup>. A 60 mm cone was used for the rheological measurements. The measurement data were processed by the rSpace 1.75 software (Malvern, Kassel, Germany). Different polymer solutions expressed in % [m/v] were analyzed: Pure Pullulan 4, 8, 10, 15, 17.5 and 20 %; Pure Gellan Gum LA: 0.225 and 0.5 %; Gellan Gum LA-Pullulan blends: 0.225 % Gellan Gum mixed with 15 or 20 % Pullulan. All samples were prepared in double distilled water. The detailed preparation of the analyzed electrospinning solutions were described in section 3.1.3.

##### Oscillatory rheology of *in situ* formed gels

The rheological behavior of the *in situ* formed gel was analyzed by the Kinexus lab+<sup>®</sup> (Malvern, Kassel, Germany) in the oscillation mode. The collected data were processed by the software rSpace 1.75 (Malvern, Kassel, Germany). All experiments were performed at 34 °C by plate-plate geometry with a diameter of 20 mm. The gap between the upper plate and the lower plate was set to 0.5 mm. Pure Pullulan fibers and fibers with 1 % [w/w] Gellan Gum LA content were investigated. Further details of the fiber preparation process are described in section 3.1.3. A fiber amount of 100 mg was hydrated by addition of 250 µl simulated tear fluid pH 7.4 (STF) or with double distilled water inside the rheometer. Detailed composition of STF is listed in Appendix 1. At first the amplitude sweep was performed to determine the linear viscoelastic region (LVR) of the sample. The detailed data of the performed amplitude sweep are described and discussed in Appendix 3. The frequency sweep was performed in a frequency range of 0.1–20 Hz at a deformation of 0.4 %.

#### 3.1.2 Light microscopy

##### Transmitted light microscopy

Each electrospinning solution was sprayed or spun directly onto an objective slide for a period of 15 s. Afterwards, the morphology of the samples was analyzed by the Axiolab (Carl Zeiss, Jena, Germany) light microscope. The microscope was connected to the UC 30

imaging system (Olympus Optical Co., Hamburg, Germany). All images were captured and analyzed by the OLYMPUS stream motion software (Olympus Optical Co., Hamburg, Germany).

### Reflected light microscopy

The reflected light microscope was used to determine the lens curvature. The lenses were imaged by an OLYMPUS SZX9 Microscope (Olympus Optical Co., Hamburg, Germany) in combination with an OLYMPUS UC 30 imaging system. All images were captured and analyzed by the OLYMPUS stream motion software (Olympus Optical Co., Hamburg, Germany).

### 3.1.3 Electrospinning

Electrospinning is an electric driven spray drying process where a viscous polymer solution underlies fiber formation under influence of an external electric field. Electrospinning allows preparation of fibers with diameters from nm to  $\mu\text{m}$  range. The electrospun samples are characterized by high porosity, high surface area and small layer thickness [73]. Figure 10 illustrates schematically the electrospinning setup and fiber formation process.

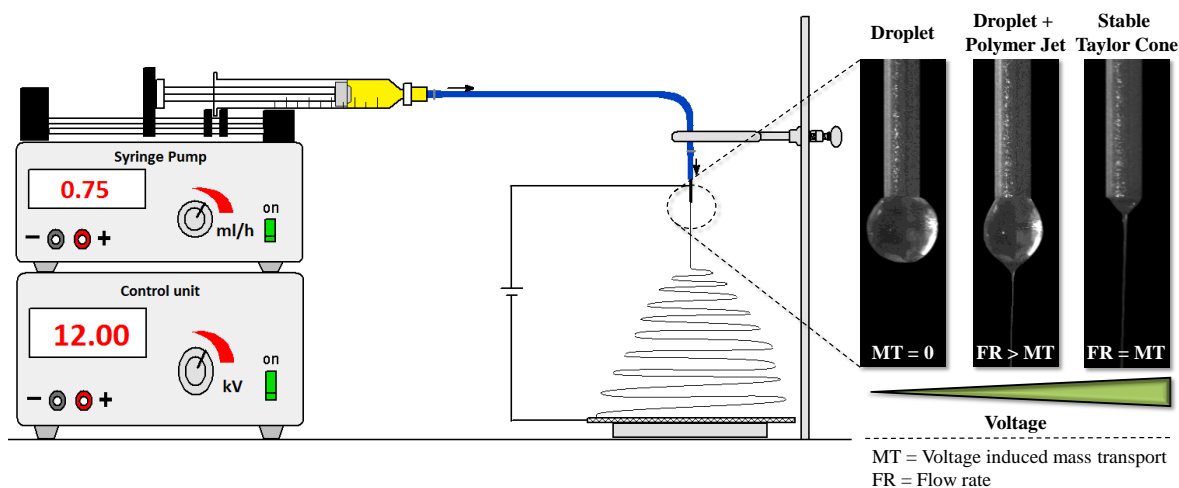


**Figure 10.** Schematic illustration of the electrospinning process with focus onto the voltage induced drop deformation at the emitter tip.

During the spinning process, the solution is transported continuously to an emitter by a syringe pump or compressor. Between the emitter and the collector system an electric field is applied. Induced by the electric field, charge formation at the solution surface takes place and the material becomes transported into direction of the collector unit. During transport, the solution underlies several physical instabilities and a jet is formed. This jet starts thinning

and drying during the flight, until solid fibers are obtained. When no voltage is applied to the polymer solution the surface tension of the spinning formulation induces a drop formation at the emitter tip. If the applied voltage passes a critical value a polymer jet is released from the droplet. With increasing voltage, the amount of transported polymer from the emitter increases as well, until flow rate and mass transport are equal. As consequence of equilibration the characteristic Taylor cone is formed at the emitter tip. Physicochemical properties of the polymer, like molecular weight, concentration, solubility and solution conductivity affect the spinnability of the formulation [74,75]. If the concentration of the polymer is too low, the polymer jet breaks up and particles are formed (= electrospraying). Beside the formulation parameters, the electrospinning setup affects the obtained products as well. All parameters like flow rate, emitter diameter, emitter geometry, emitter-collector distance, temperature, humidity and collector type have to be adjusted and screened to reach a stable and reproducible electrospinning process.

### **Formulation development and spinning of drug free fibers**

In the following section the preparation of the spinning solution and the performed electrospinning process of drug free fibers will be described. All solutions were prepared in double distilled water at room temperature. The electrospinnability and the resulting product of pure Gellan Gum and pure Pullulan, as well as Gellan Gum solutions blended with Pullulan were investigated. The detailed screened spinning solution compositions are listed in Table 6. First, the weighed amount of Gellan Gum listed in Table 6 was dispersed in double distilled water and heated up to 80 °C in a water bath, until a clear solution was obtained. For the blended solutions, Pullulan was added to the hot Gellan Gum solution followed by homogenization with a vortex mixer. Afterwards each solution was centrifuged at 1000 rpm for 10 min (Labofuge 300, Kendro, Osterode, Germany) to remove air bubbles. The electrospinning process was performed by the Electrospinning starter kit (Spraybase<sup>®</sup>, Maynooth, Ireland). The spinning solution was filled in a 1 ml Injekt<sup>®</sup>-F syringe (B. Braun Melsungen AG, Melsungen Germany). For spinning the emitter-collector distance was adjusted to 10 cm and the solution flow rate to 0.75 ml/h. All experiments were performed using a 22 G needle. Flow rate and emitter-collector distance were kept constant for all experiments. For blank fiber formation a voltage of 12-13 kV was applied to the spinning solution until a stable Taylor cone was obtained.

**Table 6.** Investigated polymer compositions of electrospinning solutions containing Gellan Gum LA (GG) and/or Pullulan (PL) in different ratios.

Number	GG [%] m/v	PL [%] m/v	Number	GG [%] m/v	PL [%] m/v
1	0.1	-	13	-	17.5
2	0.2	-	14	-	20
3	0.4	-	15	-	22.5
4	0.6	-	16	0.4	10
5	0.3	20	17	0.6	10
6	-	1	18	0.7	10
7	-	2	19	0.7	12
8	-	3	20	0.7	14
9	-	4	21	0.225	15
10	-	8	22	0.225	17.5
11	-	10	23	0.225	20
12	-	12.5	24	0.225	22.5

**Amphotericin B loaded fibers without addition of any further ingredient**

4 ml double distilled water was added to 5 mg AmpB. The dispersion was stirred under light protection at 360 rpm by a magnetic stirrer for 1 h. Afterwards the excess of AmpB was removed by centrifugation at 1000 rpm for 10 min. The clear solution was used as spinning solvent with 0.225 % Gellan Gum and 20 % Pullulan. For electrospinning a voltage of 12-14 kV was applied.

**Amphotericin B loaded fibers with sodium cholate addition**

A solution with 5 mg/ml sodium cholate was prepared in double distilled water. The solution was added to 5 mg of AmpB. The dispersion was stirred under light protection und room temperature at 360 rpm with a magnetic stirrer for 1 h. The supernatant was used as spinning solvent, to process a 0.225 % Gellan Gum and 20 % Pullulan solution. A voltage of 11-13 kV was applied for electrospinning.

**Amphotericin B-PLGA nanoparticle loaded fibers**

Details of the AmpB loaded PLGA nanoparticle preparation process will be described in section 3.2.1.

10 ml of the purified AmpB loaded PLGA nanoparticles were concentrated by an Amicon® Ultra 15 ml Centrifugal filter (100 kDa) to 3 ml. As result, a spinning solution with 444 mg Pullulan and 5 mg Gellan Gum in 1.7 ml of double distilled water was obtained. After dissolution of the polymers the solution was allowed to cool down to room temperature and 0.5 ml of the concentrated nanoparticle dispersion was added to the spinning solution. The solution was homogenized, air bubbles were removed by centrifugation with 1000 rpm for 10 min and the solution was spun at 12-13 kV.

#### **DiR-PLGA nanoparticle and fluorescein sodium loaded fibers for ocular residence time *in vitro***

Details of the DiR loaded PLGA nanoparticle preparation process will be described in section 3.2.2.

5 mg Gellan Gum was added to 0.7 ml double distilled water and 1 ml fluorescein sodium solution (15 µg/ml). The dispersion was heated up to 80 °C in a water bath until a clear solution was obtained. 444 mg of Pullulan was added to the hot solution, followed by homogenization via vortex mixing. The spinning solution was allowed to cool down to room temperature. After cooling 10 ml of DiR (ThermoFisher Scientific, Waltham, U.S.) loaded PLGA nanoparticles were concentrated with 100 kDa centrifugal filters to 1 ml. 0.5 ml of the concentrated nanoparticle dispersion was added to the spinning solution and mixed until a homogenous formulation was obtained. Air bubbles were removed via centrifugation with 1000 rpm for 10 min. A voltage of 13-14 kV was applied for the electrospinning.

#### **Amphotericin B-Eudragit L-polyelectrolyte complex loaded fibers**

A solution of 20 mg/ml polyelectrolyte complex (29 % w/w AmpB content) was prepared in double distilled water. The preparation of the complex is described in detail in section 3.3.1. Five mg Gellan Gum was hydrated in 1.7 ml double distilled water, then 444 mg Pullulan was added to the solution and was dissolved too. The solution was allowed to cool down to room temperature. Afterwards 0.5 ml polyelectrolyte complex solution was added. After homogenization of the solution, air bubbles were removed via centrifugation with 1000 rpm for 10 min at room temperature, followed by electrospinning at 14-16 kV.

#### **Fluorescein sodium loaded fibers for ocular residence time *in vivo***

Determination of the ocular residence time *in vivo* was performed by fluorescein sodium loaded nanofibers. Therefore, 10 % (v/v) of the spinning solvent was replaced by a

0.1 mg/ml fluorescein sodium solution in double distilled water. Pullulan fibers with 1 % (m/m) Gellan Gum and 0.005 % (m/v) fluorescein sodium content were obtained after spinning at 12-14 kV.

### **3.1.4 Environmental scanning electron microscopy**

Size and morphology of the electrospun fibers were investigated by environmental scanning electron microscopy (ESEM). All samples were analyzed by an ESEM XL 30 FEG electron microscope (Philips Electronic Instruments, Mahwah, U.S.). Therefore, fibers were cut in 20 mg samples and were analyzed by a gaseous secondary detector (GSE) without sputtering. The electron microscope images were captured at 0.9 Torr and an accelerating voltage of 12 keV. Several images were taken per sample. The diameters of one hundred fibers were determined by the IC Measure<sup>®</sup> software (The Imaging Source Europe GmbH, Bremen, Germany).

### **3.1.5 Thermogravimetric analysis**

The mass loss was used to determine the water content of pure Pullulan, Gellan Gum and the electrospun 1 % (w/w) Gellan Gum-Pullulan fibers. Thermogravimetric analysis (TGA) was performed with a Netzsch TG 209 (NETZSCH-Gerätebau GmbH, Selb, Germany). 20 mg of each sample were heated up with 5 K/min from 20-180 °C under nitrogen atmosphere. The water content was determined at 150 °C.

### **3.1.6 Nanoscale 3D x-ray imaging**

Nanoscale 3D x-ray imaging is a new non-destructive method to gain information about the 3D structure of samples in nm size, based on their interaction with x-ray radiation. Dependent from the radiated material properties an optical phase shift of x-ray is used for contrast formation. Fibers after curvature formation prepared from a 20 % Pullulan and 0.225 % Gellan Gum solution were analyzed, which resulted in 1 % Gellan Gum in the Pullulan fibers. The nanoscaled 3D x-ray imaging measurements were performed by Dr. Juliana Martins de Souza e Silva from the Institute of Physics at Martin Luther University Halle-Wittenberg in Germany.

The detailed method parameters and data processing procedure were described in the Appendix 3 and were published at [73]:

» [doi.org/10.1016/j.ejpb.2019.11.012](https://doi.org/10.1016/j.ejpb.2019.11.012)



### 3.1.7 <sup>1</sup>H-nuclear magnetic resonance (<sup>1</sup>H-NMR)

#### <sup>1</sup>H-NMR relaxometry

<sup>1</sup>H-NMR relaxometry experiments were performed to determine the polymer-water interaction inside the samples. All NMR measurements were carried out with a Maran DRX2 (Oxford Instruments, Oxford, United Kingdom) 20 MHz <sup>1</sup>H-NMR benchtop spectrometer. The determination of the T<sub>2</sub> relaxation time distribution was performed with a CPMG (Carr-Purcell-Meiboom-Gill) pulse sequence and a relaxation delay time of 15 s. The receiver gain was adjusted to 60. All measurements proceeded with 12000 echoes and 32 scans were averaged per pulse sequence. The collected data were processed with the WinDXP analysis software (Oxford Instruments, Oxford, United Kingdom). To calculate the T<sub>2</sub> relaxation distribution, the inverse Laplace transformation was used.

All samples were prepared in STF pH 7.4 and measured at 34 °C. Previous, the samples were pre-tempered for 10 min to ensure the sample temperature. 1 ml of pure STF, 5 and 20 % (w/v) Pullulan solution were investigated. Furthermore, 180 mg of pure Pullulan fibers and fibers with 1 % (m/m) Gellan Gum content were hydrated in 450 µl STF for 24 h. The fibers were hydrated inside NMR tube.

#### Determination of the diffusion constant

The same samples described during section of the <sup>1</sup>H-NMR relaxometry were investigated during the diffusion experiments, which were performed with the same spectrometer. A pulsed field gradient with a maximal gradient strength of 0.922 T/m and a diffusion time of 400 ms was used. The samples were analyzed at 34 °C after pre-tempering for 10 min.

### 3.1.8 3D printing

During the present dissertation the X350pro 3D printer from German RepRap GmbH (Feldkirchen, Germany) was used to print polylactic acid matrices (PLA). The printed matrices were used to adjust the geometry of the electrospun mesh to the eye curvature *in vivo*. Furthermore, a moistening chamber was printed and used for the development of a new experimental setup that determines the ocular residence time *in vitro*. All models were constructed with the DesignSpark Mechanical 2.0 software.

### 3.1.9 Curvature formation

The human ocular surface is characterized by a curved geometry. Therefore, it is essential that the applied drug delivery system is able to cover the cornea and adapt to the anatomical conditions of the human eye. The electrospun fibers were planar after the spinning process. For the curvature formation spherical disks with 1.5 cm diameter and  $4.3 \text{ mg} \pm 0.52 \text{ mg}$  weight were punched out from the planar mesh. For curvature formation a two-part 3D printed Polylactic acid (PLA) matrix was used (Figure 11). For curvature formation the lens was placed at the bottom part of the matrix. Then the upper shell was joined to the matrix bottom. The lens forming process was done by compressing the matrix moderately for 30 s. After pressure holding the lens was removed carefully and the height  $h$  was measured by reflected light microscopy. Figure 11 displays the computer-aided design model (CAD) of the lens forming matrix and the measured height  $h$ . The determined height  $h$  was used for calculation of the lens curvature by DesignSpark Mechanical 2.0 CAD software [73].

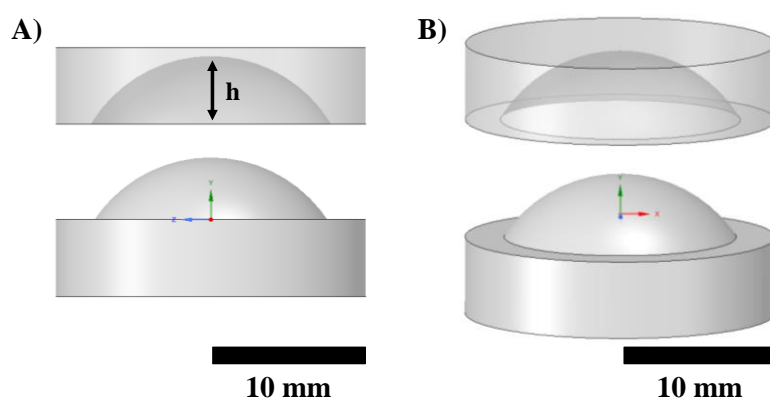


**Figure 11.** Computer-aided design model of the lens forming matrix: A) Side view of matrix with the measured height  $h$ ; B) 3D view of the lens forming matrix.

### 3.1.10 Ocular residence time *in vitro*

The ocular residence time is an important factor which influences the bioavailability, the side effects and the dose application frequency. Therefore, a new *in vitro* model for the determination of the ocular residence time was developed. The setup combines a 3D printed moistening chamber with porcine eyes and multispectral fluorescence imaging (MFSI). The *in vitro* experiments were performed with fresh extracted, non-boiled porcine eyes from a local butcher that guarantee undamaged corneas and best anatomical conditions. The eyes were used within 5 h after extraction and were stored at  $6^\circ\text{C}$  until use. Before the

experiments were performed, they were allowed to acclimatize to room temperature for 30 min. The detailed construction of the moistening chamber and the *in vitro* setup is displayed in Figure 12. The moistening chamber consists of three removable parts, which were connected by screws. The chamber has a moistening tube to ensure reproducible sample moistening with STF, a humidity chamber to guarantee sufficient room humidity and a perforated bottom plate for pressure equalization. The porcine eyes were fixated at a rubber disk in the center of the perforated bottom plate.

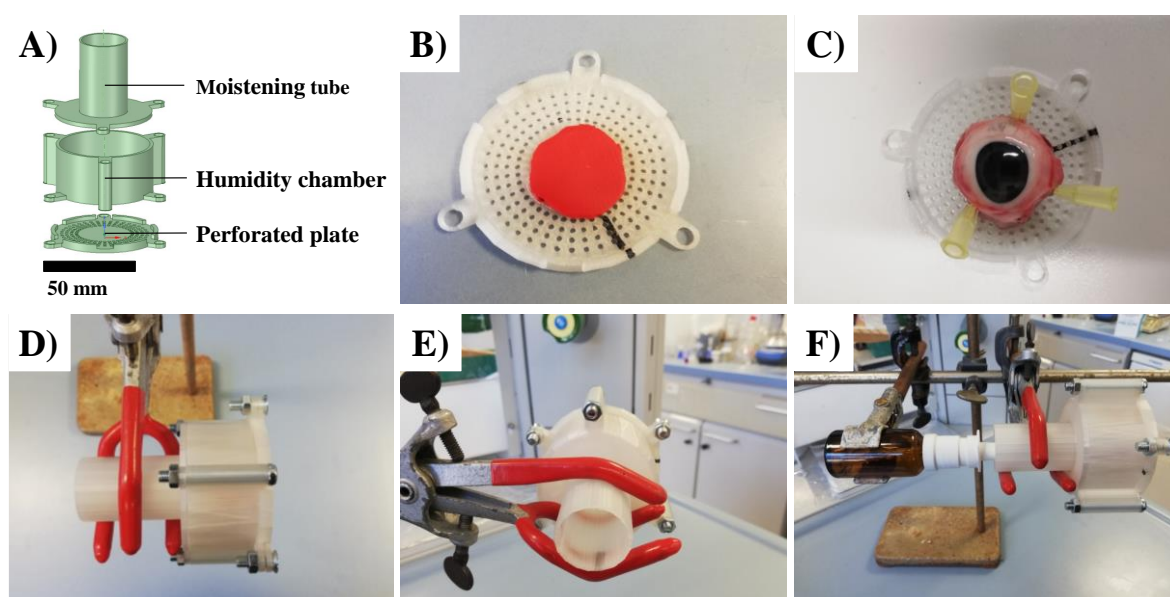


**Figure 12.** A) 3D printed moistening chamber CAD model with removable components: Moistening tube, humidity chamber and perforated bottom plate; B) Perforated bottom plate with rubber disk; C) Fixated porcine eye at the perforated bottom plate; D) Top view of the complete moistening chamber; E) Front view onto the moistening tube of the chamber; F) Experimental setup with spray applicator in vertical position.

Electrospun fibers as well as solutions were investigated. Curved lenses with 1 % (w/w) Gellan Gum loaded with 0.0001 % (w/w) fluorescein sodium and 0.001 % DiR entrapped into PLGA nanoparticles were investigated. The curved lenses had 1.4 cm diameter and a weight of  $4.2 \text{ mg} \pm 0.02 \text{ mg}$ . Before lens application, the ocular surface was wetted with  $30 \mu\text{l}$  of STF. In addition to the fibers aqueous isotone eye drops with a concentration of  $5 \mu\text{g/ml}$  fluorescein sodium were investigated as well. Therefore,  $20 \mu\text{l}$  eye drops were placed at the cornea center of the porcine eye.

After sample application the moistening chamber was assembled and placed in a vertical position. The continuous tear flow was simulated by a spray applicator (20 ml Nasenspray Pumpzerstäuber, Dr. Niedermaier Pharma GmbH, Munich, Germany). The spray applicator

allowed the instillation of  $56 \mu\text{l} \pm 6 \mu\text{l}$  STF per application. In 5 min time intervals STF was sprayed into the chamber. Between the spray applications the fixated porcine eye was removed including the perforated bottom plate. The samples were analyzed with the Maestro<sup>TM</sup> optical imaging system (Cambridge Research & Instrumentation, Woburn, United States). Different optical filter sets were used. For the DiR signal the deep red filter set with excitation wavelength of 671-705 nm, an emission filter of 750 nm long pass and acquisition settings 730-950 nm in 10 nm steps was used. The fluorescein sodium signal was captured with the blue filter set with an excitation filter of 445-490 nm, a long pass filter of 515 nm and a standard acquisition setting of 500-720 nm in 10 nm steps. The samples were automatically exposed. All captured images were processed with the Maestro<sup>TM</sup> software (version 2.10.0). After the imaging process the bottom plate was connected again to the residual components of the moistening chamber and further spray applications were performed.

## **3.2 Nanoparticles**

### **3.2.1 Amphotericin B loaded nanoparticles**

Nanoparticles were prepared according to a modified solvent interfacial deposition method [76]. Thereby, 100 mg poly(lactic-co-glycolic acid) (PLGA) was dissolved in dimethyl sulfoxide (DMSO). Different amounts of AmpB were added to the PLGA solution, leading to different drug-polymer ratios (1:100; 5:100 and 10:100) with a final concentration of 30 mg/ml PLGA. 1 ml of the polymer-drug solution was injected into 12.5 ml double distilled water. The aqueous phase was stabilized with 0.5 % (w/v) polyvinyl alcohol (PVA) (EMPORVE 5-88, Merck KGa, Darmstadt, Germany). Before use, the solvent was filtered through a 0.2  $\mu\text{m}$  polyethersulfone filter (PES, VWR International GmbH, Darmstadt, Germany). For injection, the solution was filled into a 1.0 ml GASTIGHT<sup>®</sup> syringe (Hamilton Germany GmbH, Planegg-Martinsried, Germany) and injected through a Sterican<sup>®</sup> 23 G x 3 1/8'' needle ( $\varnothing$  0.6x80 mm; B. Braun Melsungen AG, Melsungen, Germany). A continuous flow of 50  $\mu\text{l}/\text{min}$  was adjusted by a syringe pump (Pump 11 Elite, Harvard Apparatus, Holliston, United States). During injection, the solution was moderately stirred at 360 rpm with a magnetic stirrer. In Figure 13 the nanoparticle preparation process is illustrated.

To remove residual DMSO, stabilizer excess and non-entrapped AmpB, five purification steps were performed by centrifugal filtration. 5 ml of nanoparticle suspension were filled in a 100 kDa Amicon<sup>®</sup> Ultra 15 ml Centrifugal Filter (Merck Millipore, Darmstadt, Germany) and diluted with 10 ml double distilled water. The suspension was centrifuged by a Centrifuge 5810 R (Eppendorf AG, Hamburg, Germany) with 4000 rpm until the liquid level reached a minimal volume in the filter. This process has been repeated five times.

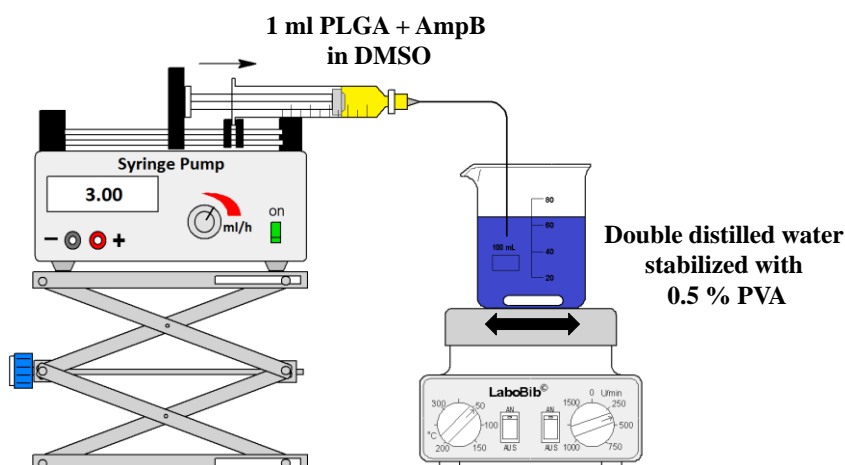


**Figure 13.** Schematic illustration of the nanoparticle preparation process.

### 3.2.2 DiR loaded nanoparticles

20 mg PLGA was dissolved in 3.6 ml acetone and 400  $\mu$ l of a 25  $\mu$ g/ml DiR solution in acetone were added. The solution was injected into 0.5 % (w/v) PVA stabilized double distilled water with a flow rate of 50  $\mu$ l/min. Residual acetone was removed by rotary evaporation (Heidolph VV2000, Heidolph Instruments GmbH & CO. KG, Schwabach, Germany) at 250 mbar at room temperature for 30 min, followed by evaporation at 60 mbar for 30 min. Afterwards, the nanoparticle dispersion was concentrated by centrifugation at 2000 rpm for 75 min. The concentrated dispersion was further utilized for electrospinning.

### 3.2.3 Photon correlation spectroscopy

The nanoparticle size was measured with photon correlation spectroscopy (PCS) using a Zetasizer Nano ZS (Malvern Instruments, Malvern, United Kingdom). The purified and DMSO containing nanoparticle suspension was diluted 1:10 with double distilled water. Before dilution the water was filtered through a 0.2  $\mu$ m PES filter (VWR International GmbH, Darmstadt, Germany). All measurements were performed in 173° backscattering mode with a refraction index of 1.330. An equilibration time of 2 min was applied to ensure

25 °C sample temperature. All measurements were repeated five times with automatic sub run determination (12-16 runs). The Zetasizer software 6.30 was used for calculation of polydispersity index (PDI) and z-average.

### 3.2.4 Nanoparticle tracking analysis

Nanoparticle tracking analysis (NTA) is a novel method that complements the nanoparticle measurement data determined with PCS. Especially the intensity weighted size distribution determined by PCS is very sensitive to larger particles, because the intensity  $I$  of the scattered light is proportional to the sixth power of the particle diameter ( $I \sim d^6$ ). But in contrast to PCS, the calculation of the NTA technique is based on visualization and determination of the moved nanoparticle distance over a defined time interval in two dimensions. The moved distance of each particle is calculated, which results in an exact determination of the number weighted particle size distribution where the intensity  $I$  of the scattered light is proportional to the particle diameter ( $I \sim d^1$ ). More detailed information about the theoretical background and based calculations of the NTA technique is described in Appendix 5.

Two different purified AmpB-PLGA ratios 1:10 and 2:10 were analyzed by the NanoSight NS300 (Malvern Instruments, Malvern, United Kingdom). The nanoparticle suspension was diluted 1:100 with double distilled water which was before filtered through a 0.2  $\mu\text{m}$  PES filter (VWR International GmbH, Darmstadt, Germany). Five different positions of the particle dispersion, filled in a 1 ml syringe (Injekt<sup>®</sup>-F Tuberkulin, B.Braun Melsungen AG, Melsungen, Germany) were analyzed with a 642 nm diode at 25 °C for 60 s. The particle motion was recorded by a sCMOS camera and analyzed with the NTA 3.1 software. The filtered double distilled water was also tested to ensure the absence of particle contamination.

### 3.2.5 Zeta potential

To determine the surface charge of the samples the zeta potential was measured with the Zetasizer Nano-ZS (Malvern Instruments, Malvern, United Kingdom). All samples were analyzed in diluted phosphate buffered saline (PBS) and diluted STF pH 7.4 (1:99). The detailed buffer compositions are listed in Appendix 1. An equilibration time of 120 s was ensured to guarantee a sample temperature of 25 °C. The number of runs was automatically set with a minimum of 10 and a maximum of 100 runs. The zeta potential calculations were

based on the Helmholtz-Smoluchowski model (Equation 1) including the electrophoretic mobility [77].

**Equation 1** 
$$\zeta = E \left( \frac{4\pi\eta}{\varepsilon} \right)$$

$\zeta$	Zeta potential
E	Electrophoretic mobility
$\eta$	Dynamic viscosity of the dispersion medium
$\varepsilon$	Dielectric constants of the dispersion medium

The zeta potential of PLGA-AmpB nanoparticles was investigated. Therefore, the purified nanoparticle dispersions were diluted 1:9 in STF and PBS, followed by the described measurement setup.

### 3.2.6 Drug load and entrapment efficacy

#### High performance liquid chromatography

All quantification experiments were carried out by high performance liquid chromatography (HPLC). The Agilent 1100 Series (Agilent Technologies, Santa Clara, United States) was used for quantification of AmpB. A RP-18 column (EC 250/4 Nucleodur 100-3 C18ec) and an isocratic elution were carried out with a ratio of 60 % mobile phase A and 40 % of mobile phase B. Mobile phase A consists of a 1:1 mixture of methanol and 1.1 g/l EDTA in double distilled water. A flow rate of 0.7 ml/min, a system pressure of 181 bar and an injection volume of 10  $\mu$ l were used for processing. The column was heated up to 30 °C and the substrates were detected by UV/Vis absorption at 405 nm. The signal after 16.7 min of retention was used for drug determination. For quantification AmpB standards were prepared in a 5/95 mixture of DMSO and methanol. The region of quantification was evaluated over a range of 0.1-100  $\mu$ g/ml AmpB. For all quantifications a correlation coefficient of minimum 0.999 was verified. All preparation steps were carried out under light protection and room temperature.

#### Drug load and entrapment efficacy of Amphotericin B loaded PLGA nanoparticles

The purified nanoparticle suspension was freeze dried for 24 h. The detailed freeze dry process is described in section 3.3.2. Ten mg of lyophilisate was dissolved in 0.5 ml DMSO and filled up to 10 ml with methanol. Precipitated PLGA was removed by centrifugation

with 6000 rpm for 10 min (IKA Mini G, IKA®-Werke GmbH & CO. KG, Staufen, Germany). The drug load and the entrapment efficacy were calculated by Equation 2 and Equation 3.

**Equation 2** 
$$\text{Drug load [\%]} = \frac{m_{WS}}{m_{DDS}} * 100\%$$

**Equation 3** 
$$\text{Entrapment efficacy [\%]} = \frac{m_{WS}}{m_{initial}} * 100\%$$

$m_{WS}$  Mass of drug in drug delivery system

$m_{DDS}$  Mass of drug delivery system

$m_{initial}$  Mass of initial used drug

### 3.3 Amphotericin B-Eudragit L-polyelectrolyte complex

#### 3.3.1 Preparation polyelectrolyte complex

The preparation of the AmpB complex was performed by a modified method described previous in the literature with poly( $\alpha$ -glutamic acid) and poly(methacrylic acid) [78,79]. In Figure 14, the polyelectrolyte complex preparation process is schematically visualized.

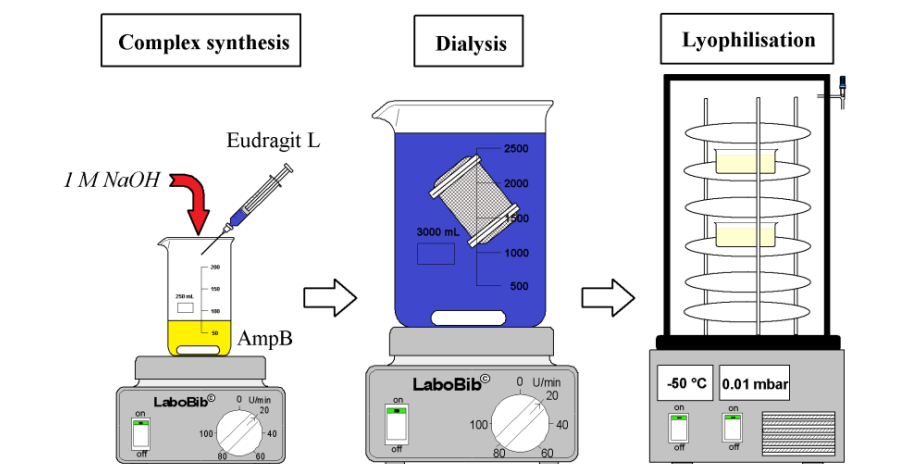


**Figure 14.** Schematic preparation process of the AmpB-Eu L polyelectrolyte complex.

Therefore, three different drug-polymer ratios with 10, 20 and 30 mg AmpB were dissolved in 1 ml DMSO. One ml of a second solution with a concentration of 30 mg/ml Eudragit L100 (Eu-L), a methacrylic acid-methyl methacrylate copolymer (1:1), in DMSO was added to the drug solution. The drug-polymer mixture was stirred with a magnetic stirrer at 600 rpm for 1 h. Afterwards 200  $\mu$ l of 1 M aqueous sodium hydroxide was added under magnetic



stirring at 1200 rpm with a drop rate of  $1 \text{ s}^{-1}$ , followed by dropwise addition of 1 ml 0.2 M aqueous sodium hydroxide under stirring. The obtained solution was dropped again in 12 ml of double distilled water under magnetic stirring with 600 rpm, followed by stirring at 200 rpm for 1 h. After stirring, the AmpB-Eu L solution was placed in a dialyses bag (Nadir<sup>®</sup> Dialysis Tubing 10-20 kDa, Carl Roth GmbH + Co. KG, Karlsruhe Germany) and was dialyzed in 3 l of double distilled water for 24 h. After dialysis the AmpB-Eu L solution was freeze dried. Further details of the freeze drying process are described in section 3.3.2.

### 3.3.2 Lyophilisation

All samples were frozen in liquid nitrogen ( $-196 \text{ }^{\circ}\text{C}$ ) until the solution was completely solidified. The freeze drying process was carried out with a Christ Alpha 2-4 freeze dryer (Martin Christ Gefriertrocknungsanlagen GmbH, Osterode am Harz, Germany) connected with a Vacuubrand RC 6 vacuum pump (Vacuubrand GmbH, Wertheim, Germany) for 24 h. A pressure of 0.06 mbar was applied to the vacuum chamber.

### 3.3.3 UV/Vis-spectroscopy

Spectral information about the prepared complex and aggregation state of AmpB was gained with the UV-1800 spectrometer from Shimadzu (Duisburg, Germany). Therefore, the extinction spectra from 300-450 nm were recorded. Doubled distilled water, methanol, PBS and STF were used as sample solvents. If a solvent mixture was used it is described in the relevant section. The spectra were processed with the UVProbe software version 2.61 (Shimadzu Corporation, Duisburg, Germany).

### 3.3.4 Attenuated total reflection infrared spectroscopy

The molecular interaction of AmpB, Eu-L and the AmpB-Eudragit L polyelectrolyte complex (AmpB-Eu L) was analyzed by attenuated total reflection infrared spectroscopy (ATR-IR). For the measurements the FT-IR spectrometer IFS 28 from Bruker (Billerica, U.S.) was used. The collected data were analyzed with the OPUS 4.2 software. The measurements were performed with 32 scans and a  $2 \text{ cm}^{-1}$  resolution. All samples were measured on a zinc selenide crystal with 1.3 mm diameter from PIKE Technologies (U.S.). The angle of incidence and reflection was adjusted to  $45^{\circ}$ . The spectra of pure AmpB, Eu-L, three different drug-polymer ratios of the complex (1:3, 2:3, 3:3) and a physical mixture (2:3) were investigated.

### 3.3.5 Drug load of polyelectrolyte complex

10 mg of complex was dissolved in 50 ml mixture of methanol-double distilled water (1:1), followed by quantification with HPLC. The calculation of the drug load (Equation 2) and the detailed HPLC performance were described in the previous section 3.2.6. The entrapment efficacy of the polyelectrolyte complex was calculated by Equation 4.

$$\text{Equation 4} \quad \text{Entrapment efficacy [\%]} = \frac{m_{\text{AmpB load}}}{m_{\text{AmpB theoretical}}} * 100\%$$

$m_{\text{AmpB load}}$  = Mass of AmpB in the sample

$m_{\text{AmpB theoretical}}$  = Mass of AmpB theoretical value

### 3.3.6 X-Ray powder diffraction

X-Ray powder diffraction was carried out with a STOE STADI MP (STOE & Cie GmbH, Darmstadt, Germany) diffractometer. The diffractometer was equipped with a molybdenum anode (50 kV, 30 mA) and a germanium (111) monochromator. The monochromator allowed transmission of molybdenum  $K_{\alpha}$  radiation at 0.071073 nm. All experiments were performed in transmission mode with rotating samples. The transmission mode was performed from  $2\theta = 5-40^{\circ}$  in  $0.5^{\circ}$  steps. Each step was captured over 60 s using a DECTRIS MYTHEN 1K Strip Detector. The STOE WinXPOW software was used to process the diffraction patterns. All samples were cryo milled under liquid nitrogen (CryoMill, Retsch GmbH, Haan, Germany) before capturing the diffraction diagram. The cryo milling process consists of three cycles of 1 min precooling phase (5 Hz) with liquid nitrogen and a 2 min milling phase with a milling frequency of 15 Hz.

### 3.3.7 Differential scanning calorimetry

The thermal behavior was analyzed with differential scanning calorimetry (DSC), using a DSC 821 (Mettler-Toledo GmbH, Gießen, Germany) with closed aluminum pans. 5 mg of sample was first heated from 0-240 °C with a heat flow of 5 K/min. After recording of the first heating curve, the cooling curve was recorded with a flow of -10 K/min. The second heating curve was performed with 5 K/min. An empty aluminum pan was used as reference. The data were processed with the software STAR SW Version 6.0.

### 3.3.8 Zeta potential

The detailed description of the zeta potential measurement parameters, apparatus and data processing were described previous in section 3.2.5. For the determination of the zeta potential of the polyelectrolyte complex 10 mg of each complex (1:3, 2:3, 3:3) was dissolved in 2 ml double distilled water. Afterwards the solution was diluted to 0.5 mg/ml in diluted PBS pH 7.4 and STF pH 7.4. The obtained solutions were characterized immediately after preparation.

## 3.4 Nanofiber characterization

### 3.4.1 Drug load of Amphotericin B loaded nanofibers

30 mg fibers (with / without sodium cholate addition and AmpB-PLGA nanoparticle loaded fibers) were dissolved in 1 ml DMSO. 100  $\mu$ l dissolved fibers were mixed with 900  $\mu$ l methanol. The dispersion was mixed for 2 min with the vortex mixer (IKA-VIBRO-FIX, Janke & Kunkel KG, Staufen, Germany). Afterwards, the precipitated polymer was removed by centrifugation for 10 min (IKA Mini G, IKA<sup>®</sup>-Werke GmbH & CO. KG, Staufen, Germany). The obtained supernatants were analyzed by HPLC.

For the drug load of AmpB-Eu L complex loaded fibers, 10 mg of polyelectrolyte complex loaded fibers were dissolved in 2 ml double distilled water. 0.5 ml of this solution was diluted to 1 ml with methanol. After vortex mixing the solution was centrifuged to remove precipitated polymer. The obtained supernatant was analyzed by HPLC and the drug load of each sample was calculated by Equation 2 in section 3.2.6.

### 3.4.2 Heat induced stress test

The impact of heat and the electrospinning process onto the AmpB-Eu L complex has to be investigated to gain information about the complex stability. Therefore, a complex (3:3) solution was prepared with a concentration of 0.1 mg/ml in double distilled water. 2 ml complex solution were placed in 4 ml vials followed by storage at room temperature as well as at 40, 65 and 80 °C in a water bath for 10 min. In addition, 10 mg complex loaded fibers loaded with AmpB-Eu L (3:3) complex were dissolved in 50 ml double distilled water without any heat influence. After sample treatment the UV/Vis spectra of each sample were recorded during an extinction range from 300-450 nm with the UV-1800 spectrometer from

Shimadzu (Duisburg, Germany). The spectra were processed with UVProbe software version 2.61 (Shimadzu Corporation).

### 3.4.3 Plate diffusion assay

The antimycotic effect of the developed drug delivery system was investigated by the performance of a plate diffusion assay. All experiments were carried out with *Issatchenkia orientalis* (syn. *Candida krusei*, Leibnitz-Institute DSMZ German Collection of Microorganisms and Cell Cultures GmbH, Braunschweig, Germany). The freeze dried strain was reactivated by 0.5 ml of autoclaved universal medium for yeasts (Appendix 1). After 30 min of swelling 0.25 ml of cell suspension was transferred into 5 ml of universal medium, followed by mixing in an end-over-end mixer at 25 °C under light protection for 24 h. For cultivation, an agar containing universal medium was used (Appendix 1). The medium was autoclaved and poured into hot petri dishes. After cooling to room temperature 0.25 ml of yeast suspension was pipetted to the agar plate and spread homogenously.

10 µl of a 100 µg/ml AmpB dissolved in 2 % DMSO-methanol and 10 µl of the blank solvent mixture were placed onto the seeded petri dish. Different fiber formulations were investigated as well. Therefore, Pullulan-Gellan Gum fibers, sodium cholate containing fibers (without AmpB), AmpB-sodium cholate loaded fibers and AmpB-Eu L polyelectrolyte complex loaded fibers were investigated. The electrospun meshes were cut into samples with 1.5 cm diameter and 4 mg weight. The applied lenses were hydrated by the residual moisture of the agar. After instillation the loaded petri dishes were incubated at 25 °C for 24 h, followed by analysis of the inhibition zone.

### 3.4.4 Electron beam sterilization

To investigate the sterilization influence of the drug delivery system, samples were treated with e<sup>-</sup>-beam. All samples were irradiated with 25 kGy at room temperature. The electron beam was performed by a linear accelerator MB 10-30 MP (Mevex, Stittsville, Ontario, Canada) at 10 MeV of the Leibnitz Institute of Surface Engineering (Dr. Wolfgang Knolle, Leipzig, Germany). The repetition rate of the accelerator was 460 Hz with 8 µs pulses, using a scanning frequency of 3 Hz and a scanning width up to 60 cm. The dose was determined with a graphite calorimeter with an error of 5 %. The residual content of pure AmpB, AmpB-Eu L complex (3:3) and the complex loaded fibers was determined after sterilization by HPLC (section 3.2.6). Furthermore, the impact of the e<sup>-</sup>-beam treatment on the molecular

weight of pure Pullulan and Gellan Gum was investigated. The detailed investigation was performed according to section 3.4.5.

### 3.4.5 Asymmetrical field-flow-field fractionation

Asymmetrical field-flow-field fractionation (A4F) is a powerful method to determine the particle size distribution, concentration of nanosize samples and to analyze the molecular weight of macromolecules [80,81]. A4F is based on the streaming sample inside a channel, where a cross-flow is applied. Dependent from the applied cross-flow a deceleration of larger particles on a stationary porous membrane takes place and the particles are fractionated by size. Smaller particles are able to move in the channel and elute first. For particle detection, different detectors based on refractive index, UV- or multi angle light scattering (MALS) can be used. In Figure 15 the basic principle of the A4F is illustrated.

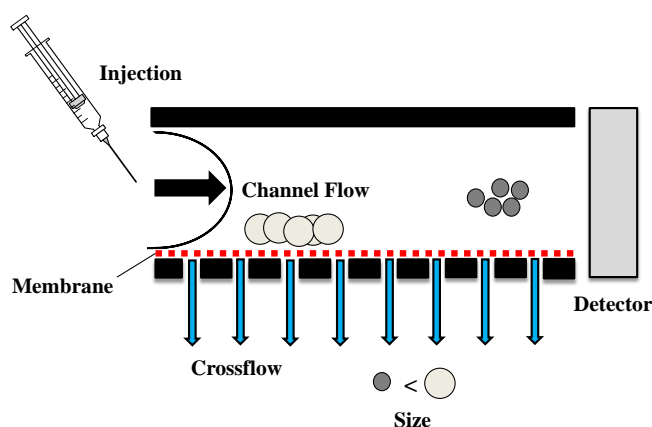


**Figure 15.** Schematic illustration of the asymmetrical field-flow-field channel fractionation of different particle sizes.

The sterilization impact on the molecular weight of Pullulan and Gellan gum starting material was analyzed by A4F combined with a Multi Angle Light Scattering in cooperation with Prof. Dr. Judith Kuntsche from the University of Southern Denmark. Therefore, an Eclipse 3+ separation system from Wyatt Technology Europe (Dernbach, Germany) was used. The A4F was connected to an isocratic pump (Aligent 1200). A Multi-angle laser light scattering detector (DAWN Heleos II) and a differential refractive index detector (Optilab rEX) were used. An AF4 short channel with an effective length of 153 mm with a 350 W spacer and a PES 10 kDa membrane was utilized. All samples were eluted with a detector flow of 1 ml/min, a focus flow of 2 ml/min and a inject flow of 0.2 ml/min. Pullulan and Gellan Gum, both as sterilized and untreated starting material, were dissolved to 2 mg/ml in

0.02 % aqueous sodium azide. The A4F was performed with MilliQ-water preserved with 0.02 % sodium azide as well. A DAQN Helios II as light scattering instrument was connected to the system. The data were processed by Astra 6 software (Wyatt Technology Europe, Dernbach, Germany). For data analysis, the Debye model for Pullulan and the Random coil model for Gellan Gum were used. A more detailed description of the theoretical background of molecular weight determination by A4F is attached in Appendix 6.

### **3.4.6 Cytotoxicity *in vitro*: hTCEpi differentiation-assay**

17000 htCEpi cells (human limbal stem cells) were seeded into 24 Well inserts with a pore size of 4  $\mu\text{m}$ . The Cells were incubated for 7 days at 37 °C and 5 % CO<sub>2</sub> in culture media (KGM-2 Bullet Kit, Lonza, Basel, Switzerland). Followed by addition of 1.15 mM calcium chloride\*2 H<sub>2</sub>O to the culture media. The cells were incubated for 14 days as an air lifted model. After incubation a multilayered cornea layer was obtained. At day 21, 40  $\mu\text{l}$  of 0.5 mg/ml AmpB eye drops and 0.62  $\mu\text{g/ml}$  diluted (with 0.9 % sodium chloride) eye drops (Amphotericin B 50 mg, Pulver zur Herstellung einer Infusionslösung; Bristol-Myers-Squibb) were placed on the air lifted side of the assay. In addition, electron beam sterilized disks with 5 mm diameter of blank fibers and AmpB-Eu L complex loaded fibers (0.68 % AmpB) were investigated. All samples were incubated for one day at the described conditions. After one day of incubation, an immunocytochemical assay with KI-67 antigen as a proliferation marker was performed, followed by microscopic determination of positive cells. Therefore, the amount of KI-67 positive cells has been determined related to the whole amount of imaged cells. The results were further differentiated into positive cells in totality of the cellular layers and positive cells in wing as well as basal cell layer. The described experiments were performed in cooperation with Dr. Joana Heinzemann and Prof. Dr. Arne Viestenz from the department of Ophthalmology at the Martin-Luther-University Halle-Wittenberg.

### **3.5 Ocular residence time *in vivo***

The ocular residence time *in vivo* is one of the major challenges in drug delivery and has to be investigated next to the *in vitro* experiments. Hence, a pilot study with three human volunteers was performed to gain detailed information about the behavior of the drug-free Pullulan-Gellan Gum fibers as ocular drug delivery system *in vivo*.

All experiments were performed under supervision and clinical responsibility of Prof. Dr. Arne Viestenz the Leader of the Department of Ophthalmology at the Martin-Luther-University Halle-Wittenberg. Before the experiments were performed, all volunteers were informed about possible risks, side effects and accepted a declaration of agreement of the experimental design. All volunteers were allowed to escape from the experiments by their own at any point of time during the investigations.

Two different formulations were investigated: Electrospun nanofibers with 1 % (m/m) Gellan Gum loaded with 0.005 % (m/m) fluorescein sodium and isotone eye drops with 0.001 % (m/v) fluorescein sodium. The eye drops were prepared by dilution of the commercial available Fluorescein ALCON 10 % with 0.9 % sterile sodium chloride to 0.001 % dye content. The fiber preparation and curvature adjustment was performed according to section 3.1.3 and 3.1.9. The prepared lenses weighed  $4.3 \text{ mg} \pm 0.52 \text{ mg}$  and were prepared with 1.4 cm after curvature formation. Fiber sterility was ensured by electron beam treatment at room temperature with 25 kGy (section 3.4.4). Immediately before human application, the 1.4 cm curved lenses were punched-out to 0.8 mm diameter. Aseptic preparation of the eye drops ensured the absence of microbiological contaminations in solution. Three volunteers (2 male; 1 female) between 40 and 55 years participated in the performed study. Previously, the initial physiological ocular conditions of each volunteer were determined by optical coherence tomography (OCT), Pentacam<sup>®</sup> imaging and pH measurements. After determination of the initial ocular state, the eyes of the volunteers were anesthetized with one drop of Oxybuprocainhydrochloride 4 mg/ml (Conjucain<sup>®</sup> EDO<sup>®</sup>, Bausch&Lomb GmbH, Berlin, Germany). After 5 min of anesthesia, the samples were applied while the volunteers rested in a horizontal position. Immediately after sample application, the OCT images were captured over a period of 30 min in 5 min intervals. The Pentacam<sup>®</sup> images were captured in 15 min intervals. All *in vivo* experiments were performed in cooperation with Prof. Dr. Arne Viestenz and his research group from the department of Ophthalmology at the Martin-Luther-University Halle-Wittenberg.

### 3.5.1 Optical coherence tomography

OCT is a non-invasive method to gain a two dimensional cross-sectional image by optical light scattering of the tissue microstructure *in vivo* [82]. In clinical practice OCT is used during diagnosis of different ocular diseases like glaucoma, age-related macular degeneration, neovascularization and pathogenic alteration of blood vessels during diabetic

retinopathy [83–86]. The ocular residence time was determined with the SPECTRALIS® OCT (Heidelberg Engineering GmbH, Heidelberg, Germany) what allows Scanning-laser-fundus imaging combined with OCT imaging. The Heidelberg Eye Explorer 1.9.17.0 software was used for image processing. The OCT images were captured with an infrared (IR) laser light source with a wavelength of 812 nm and an output power of 0.30-0.80  $\mu$ W (high resolution). The scan angle was adjusted to 30° and the laser power to 100 %. A sensitivity of minimum 83 % was ensured for all measurements. The OCT images had a x-y-size of 1536 px\*1536 px (16.7 mm\*16.7 mm).

For visualization and quantification of the fluorescence signal the BluePeak autofluorescence mode (BAF) was used. Therefore, a fluorescein scanning angiography (FA) laser with a wavelength of 486 nm and output power of 0.23-0.31  $\mu$ W (high resolution) was used to examine the anterior segment of the eye. A scan angle of 30° with a minimum sensitivity of 90 % and a laser power of 100 % was applied. The BAF images had a x-y-size of 1536 px\*1536 px (16.7 mm\*16.7mm). Quantification of the fluorescence signal was performed by processing the grayscale images with the ImageJ software (version 1.52a, National Institutes of Health, United States).

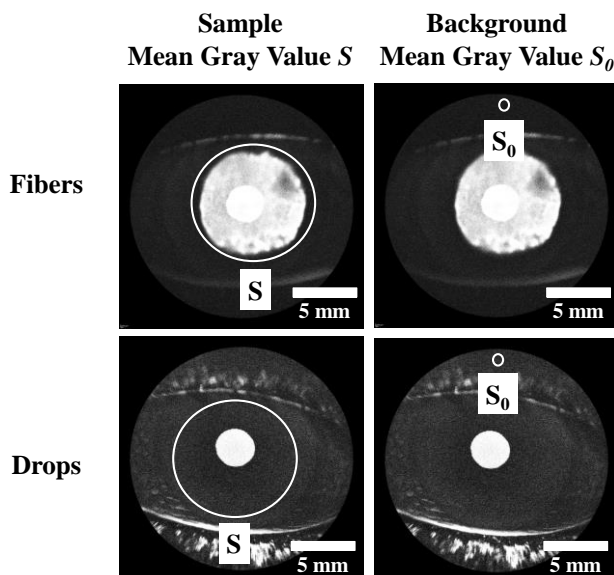


**Figure 16.** Analysis and fluorescence quantification of BluePeak autofluorescence mode (BAF) images of fluorescein sodium loaded fibers and eye drops: background mean gray value ( $S_0$ ); Sample mean gray value ( $S$ ).

At first, the captured images were transformed into 32 bit grayscale image, followed by placement of two different regions of interest. One region was placed in the center of the



ocular image to determine the sample mean gray value  $S$ . The second region was set to the background of the image to calculate the background mean gray value  $S_0$ . Figure 16 illustrates exemplary the localization of the placed areas used for determination of  $S$  and  $S_0$  for the applied lenses and the instilled fluorescein sodium eye drops in the BAF image. The fluorescence signal localized in cilia and saccus conjunctivae were neglected during the quantification procedure. The mean fluorescence intensity  $MFI$  was calculated from the determined gray values  $S$  and  $S_0$  by Equation 5.

**Equation 5** 
$$MFI = \frac{S - S_0}{S_0}$$

MFI	Mean fluorescence intensity
S	Mean gray value drug delivery system
$S_0$	Mean gray value background

### 3.5.2 Pentacam® imaging

The topography of the anterior corneal surface was investigated with the Pentacam® (OCULUS Optikgeräte GmbH, Wetzlar, Germany), based on a rotating Scheimpflug camera. The system allows the investigation of the cornea topography like curvature, refractive power and corneal thickness [87,88]. During this research the Pentacam® imaging was used to determine the thickness of the untreated cornea as well as of the lens loaded cornea.

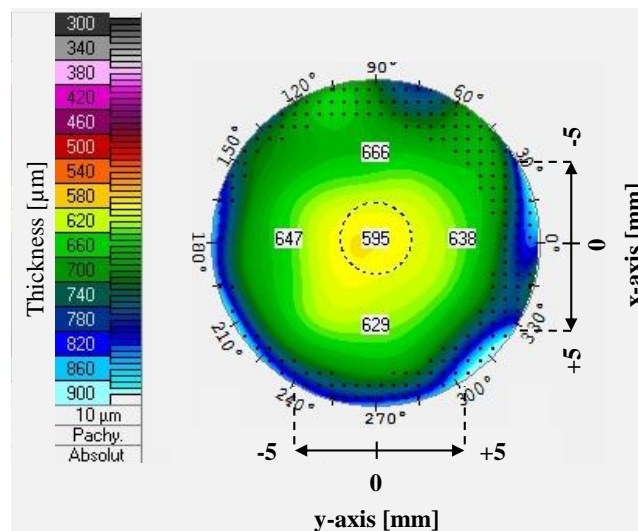


**Figure 17.** Exemplary Pentacam® image with localized measurement points used for cornea thickness determination in vivo: Cornea center (dotted area) and four measurement regions in 5 mm distance from the cornea center in vertical ( $x$ ) and horizontal ( $y$ ) axis.

The thickness of the cornea center and the thickness of four points in 5 mm distance in horizontal and vertical position from the corneal center was determined. Figure 17 displays an exemplary Pentacam<sup>®</sup> image which illustrates the local distribution of the analyzed regions. The eyes of all patients were investigated before and after lens application over a period of 30 min in 15 min intervals. The gel thickness was determined by subtraction of the untreated cornea thickness from the value after fiber application.

### 3.5.3 Tear pH measurement

The influence of the sample onto the physiological tear fluid pH was determined with pH sensitive Blema-Strips<sup>®</sup> (Aristo Pharma GmbH, Berlin, Germany) previous and 60 min after lens instillation. The pH stripes ensure a reliable detection of the pH in the range 5.6-8.0. The strips allow a pH resolution in 0.3 pH steps with a scale-reading precision of  $\pm 0.1$  pH units.

### 3.5.4 Photographic pictures

All photographic pictures of sample preparation and lens application during the *in vivo* experiments were taken with a Nikon D70S from Nikon GmbH (Düsseldorf, Germany) with 6.1 Mpx.

## 3.6 Software

The present thesis was written in Microsoft word 2010 (Microsoft Corporation, Redmond, U.S.). All citations were processed with Mendeley Desktop Version 1.19.4 (Mendeley Ltd. Elsevier Inc., New York, U.S.). Data analysis and graphic plots were performed with OriginPro 2019 (OriginLab Coporation, Northampton, U.S.). Illustrations of the Graphs were made with Microsoft Power Point 2010 (Microsoft Corporation, Redmond, U.S.). Chemical structures were drawn with ACD/ChemSketch Version 12.01 (Advanced Chemistry Development, Toronto, Canada).

## 4 Results and Discussion

### 4.1 Formulation development and characterization

#### 4.1.1 Rheology of electrospinning solutions

The rheological behavior of the spinning solutions is essential for the preparation of ultrathin nanofibers. During the electrospinning process, different zones with characteristic shear forces treat the spinning solution. The transport of the polymer solution by the syringe pump into the spinning system and especially the region inside the Taylor cone, where the fiber thinning takes place, is characterized by intensive shear forces. Fiber formation occurs when the molecule interaction is sufficient to overcome the surface tension of the solution. A minimal entanglement concentration of the used polymer is essential for fiber formation. Each kind of polymer shows, depending on the molecular structure and molecular weight, different entanglement concentrations. Therefore, rheology measurements in rotation mode were performed to elucidate the rheological properties of the polymer solutions.

Figure 18 displays the viscosity profiles of different Pullulan and Gellan Gum solutions. A) Shows the profile of the Pullulan solutions at various shear rates. The magnification of the lower concentrated solutions is displayed in B). All solutions are prepared in double distilled water and all concentrations are given in % m/v. The viscosity of 4 % Pullulan is approximately constant at 0.01 Pas over the complete shear rate and can be noted as a newton fluid. 8 % Pullulan had a viscosity of 0.06 Pas at  $1 \text{ s}^{-1}$  and 0.04 Pas at  $1000 \text{ s}^{-1}$ . 10 % Pullulan is characterized by a viscosity of 0.12 Pas at the beginning and 0.08 Pas in the end of the shear process. Both solutions showed an immediate decrease about 33 % of the initial viscosity. Higher Pullulan concentrations are characterized by an increase of the initial viscosity. 15, 17.5 and 20 % Pullulan solutions showed different viscosity profiles compared to the lower concentrated solutions. Before the viscosity of the solution decreased the viscosity stayed constant and a plateau was formed under treatment with lower shear rates. The viscosity of the 15 % Pullulan solution decreased from 0.5 Pas at  $1 \text{ s}^{-1}$  to 0.3 Pas at  $1000 \text{ s}^{-1}$ , which is a reduction about 40 %. The 17.5 % Pullulan solution had an initial viscosity of 0.9 Pas at  $1 \text{ s}^{-1}$  and reached 0.5 Pas at  $1000 \text{ s}^{-1}$ . Therefore, the viscosity decreased about 44 % of the initial value. The initial viscosity of 20 % Pullulan was 1.62 Pas at  $1 \text{ s}^{-1}$ , after treatment at  $1000 \text{ s}^{-1}$  the viscosity decreased to 0.6 Pas with a reduction of 63 %. All three Pullulan solutions showed a shear thinning effect by increasing the polymer

concentration. In contrast to this 15-20 % are characterized by a plateau of the measured viscosity from 1-10  $s^{-1}$ , followed by viscosity decrease.

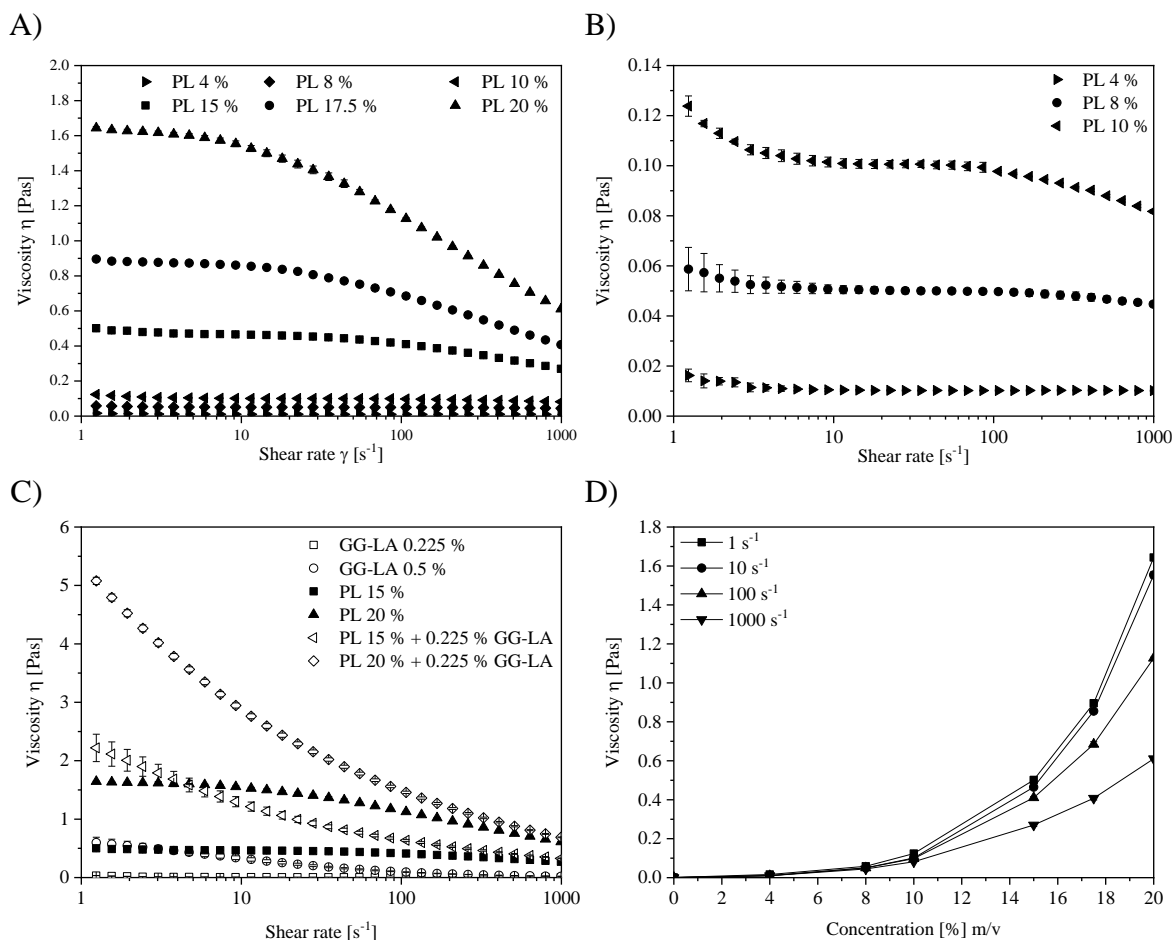


**Figure 18.** Shear rate dependence of viscosity  $\eta$  during rotation rheology: A) Viscosity dependence of different Pullulan (PL) solutions; B) Magnification of 4, 8 and 10 % Pullulan solution; C) Viscosity dependence of Pullulan, Gellan Gum LA (GG-LA) and blended solutions; D) Viscosity dependence of Pullulan concentration at various shear rates (mean  $\pm$  SD,  $n = 3$ )

The Pullulan molecules form random coils in solution. Higher polymer concentrations increase the number of random coils and entanglement formation between the polymer chains, what results in a rise of the solution viscosity. The viscosity plateau of the Pullulan solutions  $\geq 15$  % at low shear rates is caused by entanglement disruption and immediately replacement by new formed entanglements [89]. When the disruption by shear forces exceeds the polymer entanglement replacement, the viscosity decreases.

To assess the influence of the *in situ* gelling agent, the pure Gellan Gum was analyzed in different concentrations. Therefore, pure Gellan Gum solutions with a concentration of 0.225 % and 0.5 % as well as blended mixtures with Pullulan were investigated. In Figure

18 C) the impact of the *in situ* gelling agent on the viscosity is displayed. 0.225 % Gellan Gum is characterized by a viscosity of 0.03 Pas at  $1 \text{ s}^{-1}$  and 0.02 Pas at  $1000 \text{ s}^{-1}$ . 0.5 % Gellan Gum had a viscosity of 0.6 Pas at  $1 \text{ s}^{-1}$  and at 0.02 Pas at  $1000 \text{ s}^{-1}$ . These data represent a reduction of the initial viscosity of about 97 %. The enormous decrease of the Gellan Gum solution viscosity is caused by the chemical structure of the polymer. The  $\beta$ -D-glucuronate unit of the polymer is characterized by carboxylic functions, which allow anionic carboxylate formation in aqueous media. The electrostatic repulsion of the anionic carboxylate prevents polymer chain interaction and entanglement formation. Therefore, the viscosity reduction of the Gellan Gum solution takes place immediately after applying shear forces [56]. The data of 0.5 % Gellan Gum illustrates that the shear thinning effect of the solution is higher than the effect of the 15-20 % Pullulan solutions. In comparison to the pure Pullulan solution,  $\geq 15$  % Gellan Gum showed in the beginning no viscosity plateau. Instead Gellan Gum underlied immediately a shear thinning effect after shear forces treatment. The anionic nature of Gellan Gum and the low extent of entanglements predict the inability of fiber formation during electrospinning.

Next to the pure polymer solutions, two different Gellan Gum / Pullulan blended solutions were investigated. 0.225 % Gellan Gum blended with 15 and 20 % Pullulan. It was observed (Figure 18 C) that the viscosity of the 0.225 % -15 % blend was 2.2 Pas at  $1 \text{ s}^{-1}$  and 0.3 at  $1000 \text{ s}^{-1}$ . The 0.225 %-20 % blend had a viscosity of 5.0 Pas at  $1 \text{ s}^{-1}$  and 0.7 Pas at  $1000 \text{ s}^{-1}$ . Both samples showed a high shear thinning effect immediately after shear start. Compared to the viscosity of the pure Pullulan solutions the viscosity of the blended solutions increased and the initial plateau at lower shear rates disappeared caused by the Gellan Gum addition. The increase of the viscosity after Gellan Gum addition can be explained by the interaction of the hydrophilic polymers. The increased amount of polymer chains enables entanglement formation and induce the rise of the solution viscosity.

In Figure 18 D), the viscosity profiles of the different concentrated Pullulan solutions at various shear rates 1, 10, 100 and  $1000 \text{ s}^{-1}$  are displayed. From 0-10 % Pullulan no differences of the viscosities were detected for different shear rates. The 15 % Pullulan solution showed that the viscosity varies with the applied shear rate. The viscosity at  $1$ - $100 \text{ s}^{-1}$  showed no differences with a viscosity around 0.4-0.5 Pas, but at  $1000 \text{ s}^{-1}$  the viscosity decreased to 0.27 Pas. With further increase of the Pullulan concentration to 17.5 and 20 % the distinction in viscosity at different shear rates increase as well. During

electrospinning the solution viscosity inside the Taylor cone is the critical factor for fiber formation. Inside the Taylor cone shear rates of 100-1200 s<sup>-1</sup> take place depending on the applied voltage and needle diameter [56,90]. Sufficient polymer chain entanglements at the acting shear rates are required for fiber formation. It seems to be, that the amount of entanglements at 1000 s<sup>-1</sup> of the  $\geq 15\%$  pure Pullulan solutions is sufficient for fiber formation by electrospinning. It can be assumed that the viscosity necessary for fiber formation is between 0.1 Pas and 0.27 Pas. The results of the rheology experiments cannot be transferred to other polymer solutions like PLGA in methylene chloride or PVA in water for example. The viscosity depends strongly on the polymer itself and especially on the solvent-polymer interaction. The fact that Gellan Gum has a huge shear thinning effect in the observed solutions and the corresponding viscosity at higher shear rates predicts that Gellan Gum is not able to form fibers by itself.

#### 4.1.2 Optical characterization of the electrospun products

Electrospinning is a complex manufacturing process, which allows the preparation of polymer fibers in the upper nm and lower  $\mu\text{m}$  range. Many parameters affect the spinning process and allow modification of the obtained product. The parameters can be differentiated into formulation and processing parameters. The formulation parameters include all effects on the spinning formulation caused by the used substances and solvents. The kind of polymer and the used solvent influence the solution viscosity, surface tension and conductivity [91-93]. The parameters adjusted during electrospinning process like solution flow rate, applied voltage and emitter-collector distance have an impact onto the electrospun product as well [74,75,94]. Additionally, a variation of the needle diameter or combination with a coaxial spinning setup allow modification of the product properties [95]. The suitable spinning parameters and formulation composition have to be screened in detail to reach electrospinning of uniform fibers. As consequence it is necessary to determine empirically the spinnability of each formulation.

Figure 19 displays the light microscopic images of the obtained products of different spinning solutions. A) and B) show exemplary the results of the spinning process with 0.4 % and 0.6 % Gellan Gum solution. All pure Gellan Gum solutions resulted in detaching droplets from the emitter tip without drying. Large amounts of liquid Gellan Gum solution accumulated at the collector plate. Comparable results are also described in the literature, that pure Gellan Gum does not allow fiber formation via electrospinning [56]. The polymer

structure affects the electrospinnability. As described during the section before, electrostatic repulsion of the carboxylic groups of Gellan Gum prevents chain entanglement inside the polymer stream. As consequence, the polymer jet breaks up and continuous fibers cannot be formed. By increasing the applied voltage, the control over the process was lost. These results demonstrate that fiber formation with pure Gellan Gum solutions is not possible, what correlates with the assumptions from the determined viscosity profiles.

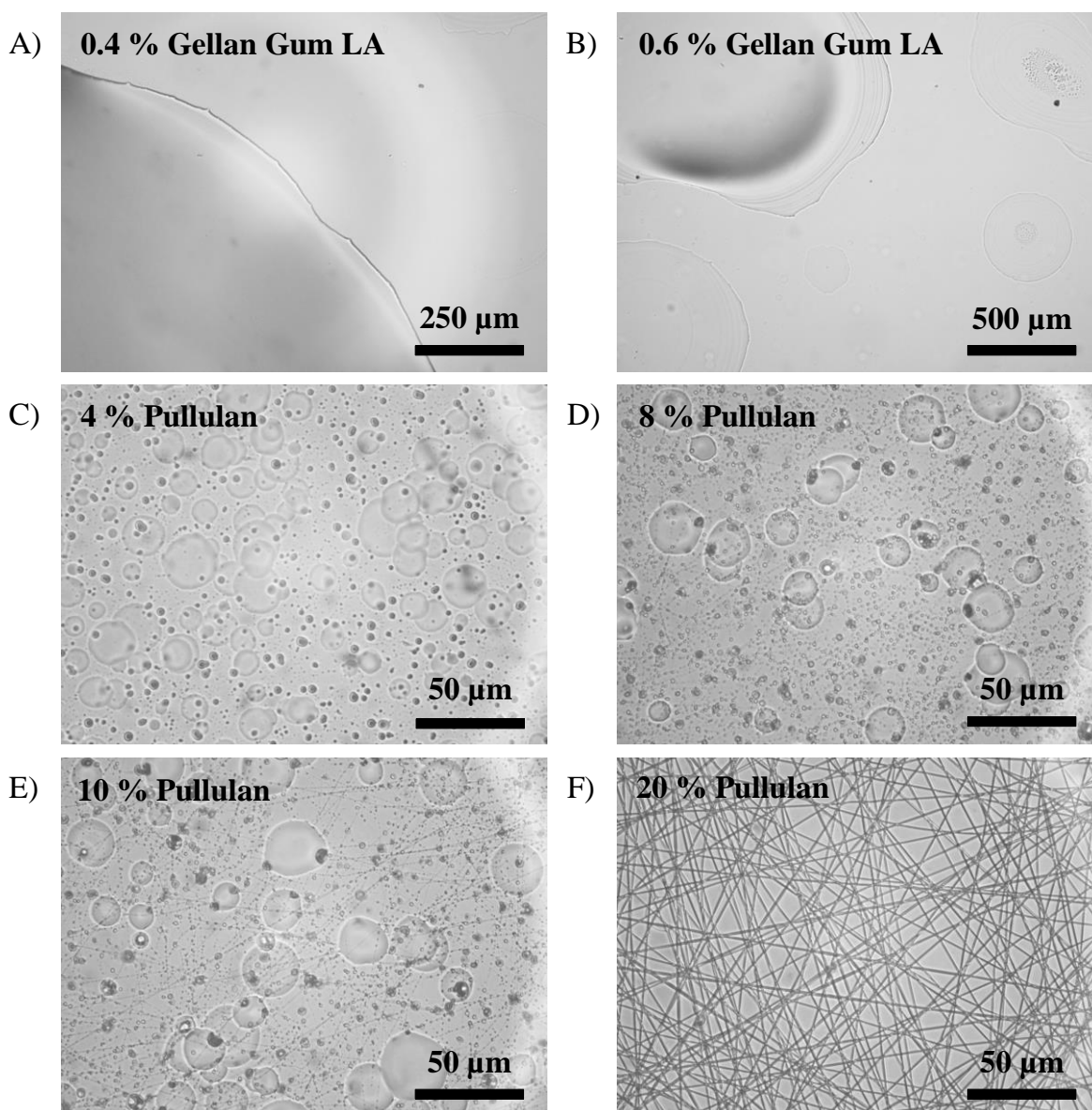


**Figure 19.** Light microscopic characterization of the electrospun products at different magnifications as outcome of different spinning solution compositions (% w/v). The polymers were dissolved in double distilled water and were electrospun.

To improve the spinnability of Gellan Gum, Pullulan seems to be a promising polymer, because of its rheological behavior and lack of charged groups. Therefore, different ratios of

Pullulan and Gellan Gum were electrospun. Figure 19 C-F displays the images of the obtained products after electrospinning of 4, 8, 10 and 20 % pure Pullulan solutions. The image of the 4 % Pullulan solution (C) is characterized by droplets and particles, which were formed during the spinning process in randomized orientation. By increasing the polymer concentration to 8 % Pullulan (D) the amount of particles increased and the particles started to align in lines or rows, but without any connection to each other. A further increase of the Pullulan concentration to 10 % (E) resulted in formation of beaded fibers. In the background, droplets detached from the emitter tip are visible. The obtained particles are connected over solidified polymer linkages, also non-continuous connections of the particles were observed. A solution which flows through a capillary shows, caused by the surface tension, a break up into smaller droplets similar to the spinning process [96]. These droplets dried during flight and particles were obtained. The polymer stream ejected from the Taylor cone was not able to prevent stream break up. As consequence short fibers with few connections were obtained. The surface tension of the solution is the driving force to minimize the solution surface and as consequence particles or beaded fibers are formed. The main reason for fiber preparation is the competition of the surface tension and the viscoelastic force of the solution to prevent jet break up during electrospinning [93]. After increasing the Pullulan concentration to 20 % uniform fibers were obtained (Figure 19 F). In comparison to the lower Pullulan concentrations described before, the viscoelastic forces of the polymer solution are sufficient to prevent breakup of the polymer stream. After fiber formation with pure Pullulan, different amounts of Gellan Gum were added to the Pullulan solution and were tested for fiber preparation. In Figure 20 all investigated spinning formulation compositions were classified by the electrospun products and were differentiated into droplets, beaded-fibers, fibers with stable and unstable spinning conditions. An unstable process means formulations which do not allow continuous fiber preparation, because of detaching droplets from the Taylor cone. Solutions with  $\geq 15$  % Pullulan and 0.225 % Gellan Gum allow fiber formation under stable conditions. The plotted data illustrate, that fibers were observed when the Gellan Gum amount was  $\geq 0.3$  % in the spinning solution, but the process became unstable. During spinning of these Gellan Gum solutions the electrostatic repulsion of the anionic polymer cannot be compensated by the copolymer addition. In consequence liquid drops start detaching from the Taylor cone onto the spun mesh. This spinning process prevents further scale up and continuous manufacturing of the fibers for all following fabrication steps. A list



of the investigated spinning solutions and their detailed composition with the correlating results are listed in Appendix 2.

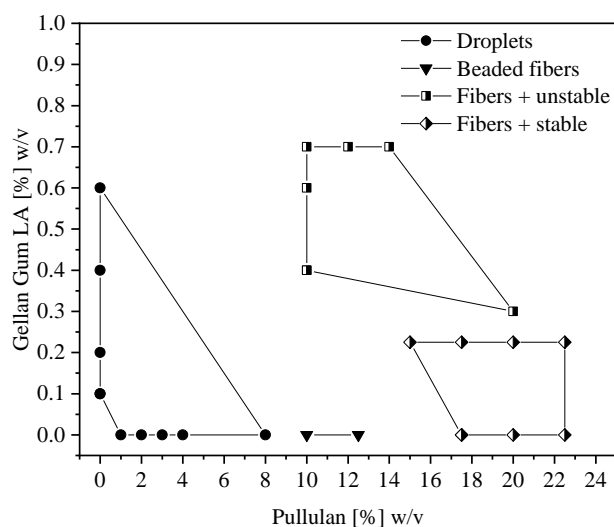


**Figure 20.** Impact of composition of the polymer solutions on the results of the electrospinning process.

The potential formulations which allowed formation of uniform fibers in combination with a stable electrospinning process were further investigated by ESEM to determine the exact fiber size distribution. In Figure 21 the ESEM images of three different formulations containing 0.225 % Gellan Gum and their correlating fiber diameter distribution are displayed. All fibers showed a smooth appearance without structural irregulars with diameter in the middle nanometer range. The average fiber diameter of the 15 % Pullulan-0.225 % Gellan Gum spinning formulation is 318 nm, for the 17.5 % Pullulan-0.225 % Gellan Gum 393 nm and for 20 % Pullulan-0.225 % Gellan Gum 398 nm. With increasing Pullulan concentrations, the mean fiber diameter increased as well. The Pullulan influence becomes more evident when we consider the median of the formulations. The median of the distributions increased as well from 315 nm to 387 nm to 397 nm by increasing the amount of the Pullulan. In fact, the polymer amount which is transported during time by the polymer stream rises with increasing the Pullulan concentration, which induce formation of fibers with higher diameters [97]. Electrospinning as a special kind of spray drying process is strongly affected by ambient conditions like room temperature and room humidity. Each electrospinning experiment was performed at relative humidity < 70 %. At higher moisture contents the drying process was disturbed especially for 15 % and 17.5 % Pullulan containing formulations. The formulations prepared from the 20 % Pullulan-0.225 % Gellan

Gum solution was not sensitive to higher room humidity and allowed continuous reproducible fiber preparation independent from the ambient conditions. Hence, further fiber characterizations were performed with the 20 % Pullulan-0.225 % Gellan Gum formulation. In the following sections this formulation is described as 1 % Gellan Gum containing Pullulan fibers, because of the Gellan Gum content in solid state.

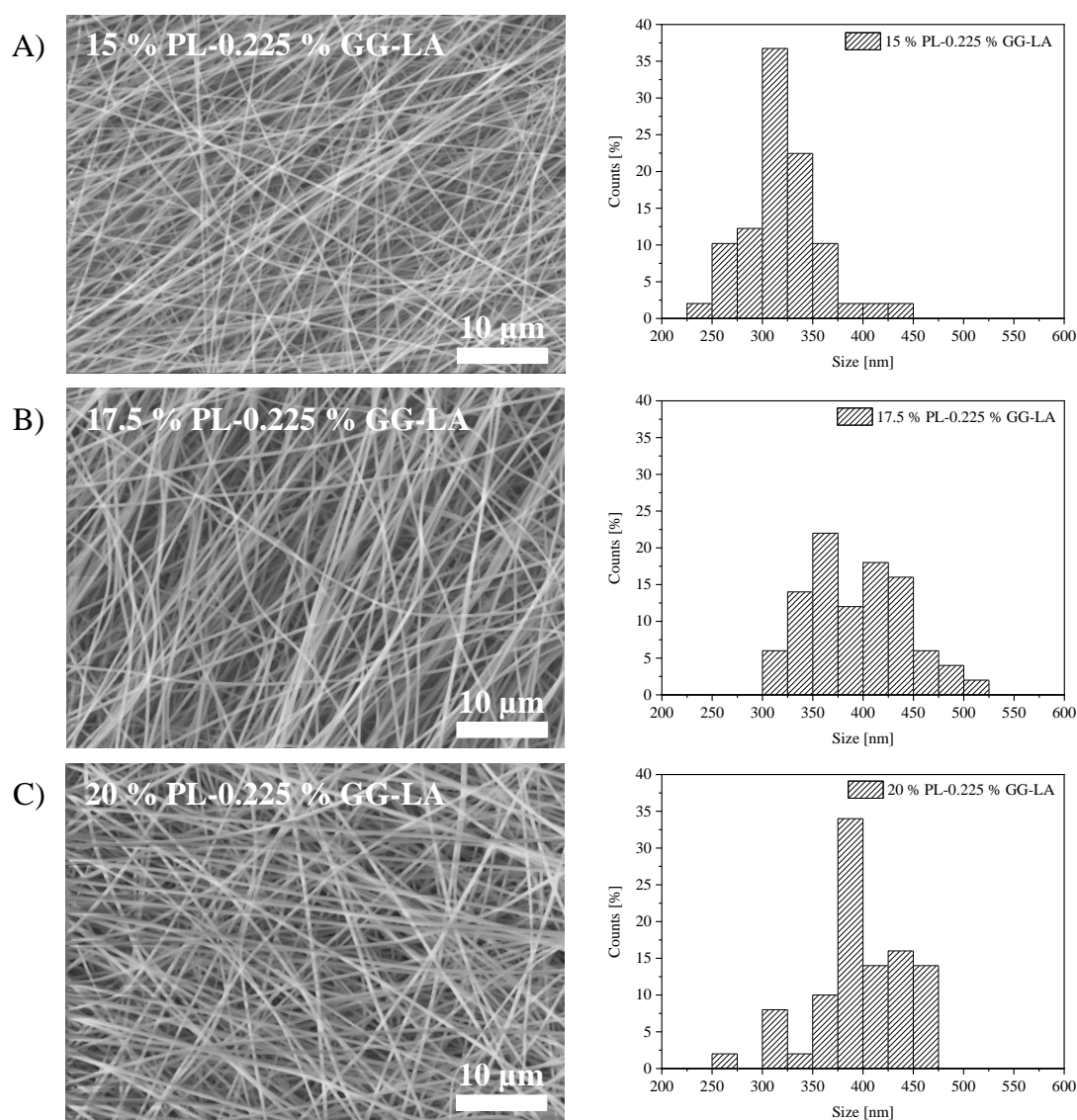


**Figure 21.** Environmental scanning electron microscope images of Pullulan (PL)-Gellan Gum (GG-LA) fibers prepared from blended spinning solutions with varying polymer content and the correlating fiber diameter size distribution.

#### 4.1.3 Water content

The residual water content of the electrospun fibers is an essential product quality parameter, because it impacts the mechanical properties and the chemical stability. Therefore, the

moisture content of the educts as well as in the electrospun fibers containing 1 % Gellan Gum were determined. The results are displayed in Figure 22.

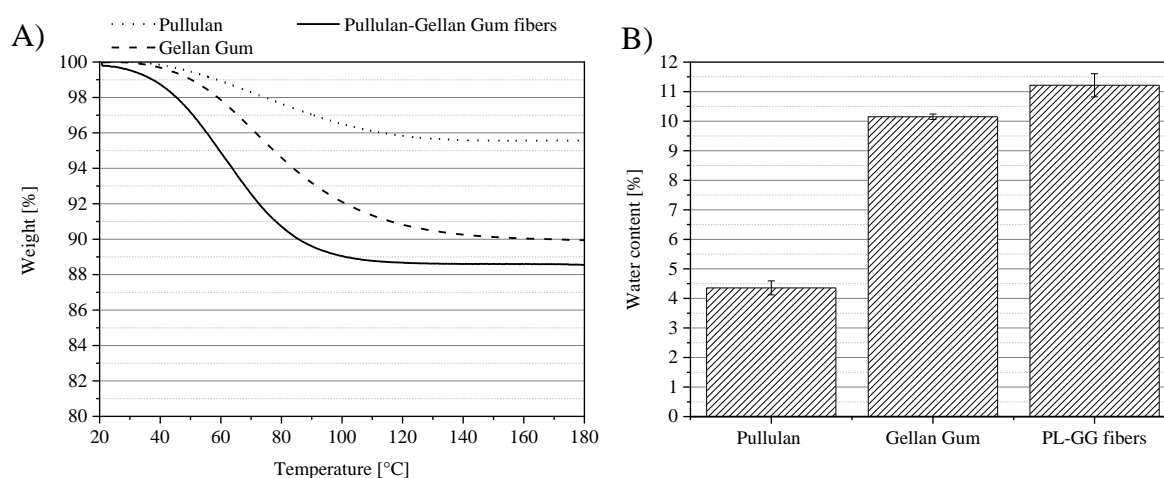


**Figure 22.** Thermogravimetric analysis of Pullulan and Gellan Gum educts compared with the moisture content of the 1% Gellan Gum containing Pullulan fibers (PL-GG fibers): A) Sample weight over a temperature ramp; B) Water content at 150 °C (mean  $\pm$  SD,  $n = 3$ ).

All samples showed a characteristic loss of mass which began after starting the increase of the temperature. The mass loss is caused by the evaporation of water. The mass of the samples stayed constant at 150 °C. Therefore, the mass loss of the samples at 150 °C will be compared to gain information about the residual water content. The unprocessed Pullulan had a water content of 4.4 %, Gellan Gum of 10.2 % and the electrospun fibers 11.2 %. After the electrospinning process, the fibers contained 1 % more moisture compared to the Gellan Gum starting material. These illustrates, that further drying after the electrospinning process was not necessary to reach thermodynamic stability of the fibers.

#### 4.1.4 Rheology of *in situ* gelled nanofibers

To gain information about the viscoelastic properties of pure Pullulan fibers and Gellan Gum blended fibers, the samples were investigated by oscillation rheology. In the following section the results of the described experiments will be discussed. It is well known, that the temperature influences strongly the viscoelastic properties of semi-solids, therefore all samples were investigated at 34 °C correlating to the ocular surface temperature *in vivo* [98]. In addition, the effect of cation free and cation containing gelling media were investigated. Pure Pullulan and Gellan Gum blended fibers were hydrated once with double distilled water as well as with STF. Before, the amplitude sweep was performed to determine the linear viscoelastic region (LVR). These results are discussed in Appendix 3.

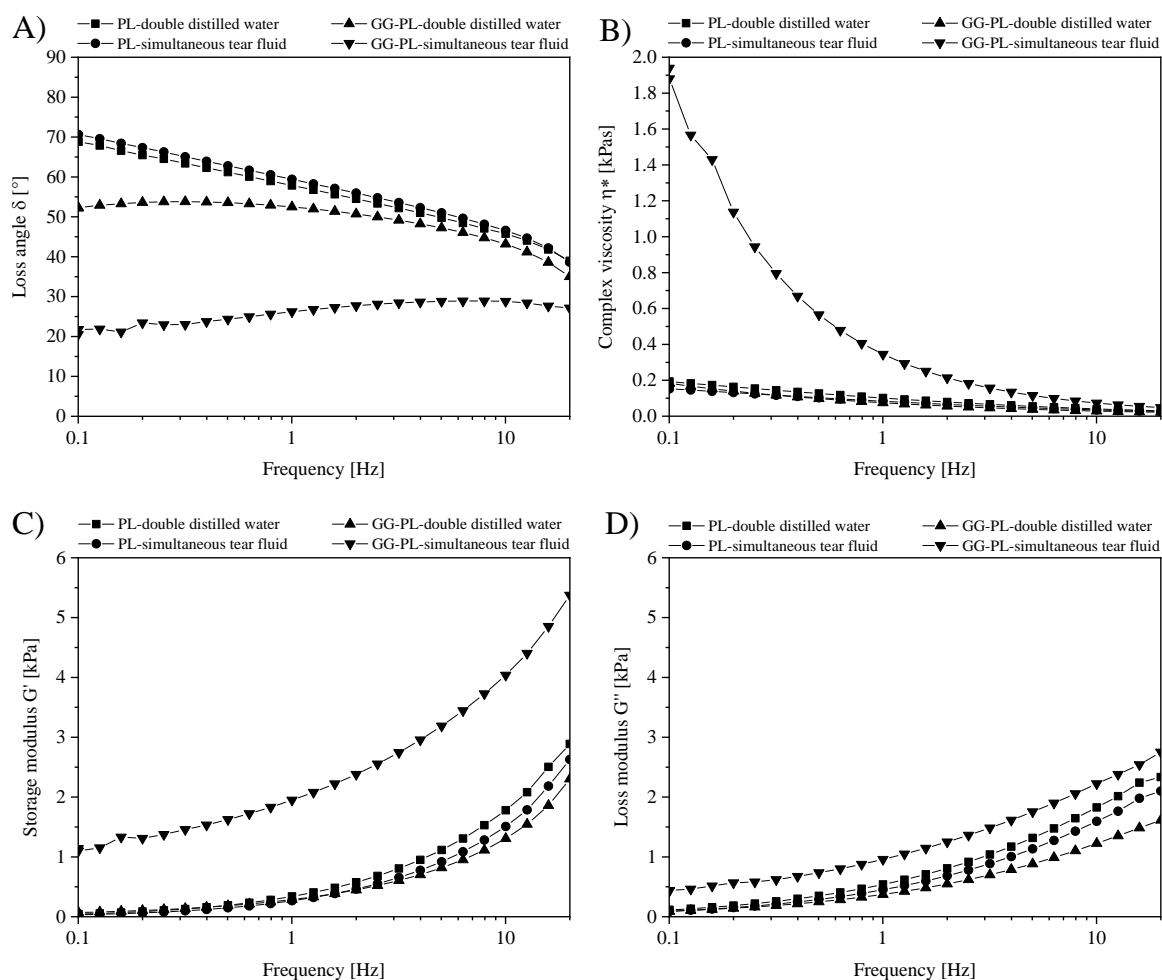


**Figure 23.** Rheological properties (obtained by a frequency sweep) of pure Pullulan and 1 % Gellan Gum blended fibers in double distilled water and STF pH 7.4 at 34 °C: A) Loss angle  $\delta$ ; B) Complex viscosity  $\eta^*$ ; C) Storage modulus  $G'$ ; Loss modulus  $G''$  ( $n = 3$ ).

In Figure 23 the results of the frequency sweep are displayed performed at 0.4 % deformation. It is obvious that storage modulus  $G'$  and loss modulus  $G''$  increased for all samples with increasing the shear frequency. The elastic modulus  $G'$  of the Gellan Gum blended Pullulan fibers hydrated with STF is higher in comparison to the other samples. This suggests that the elastic amounts caused by the Gellan Gum addition increased by hydration with STF. The loss angle  $\delta$  of pure Pullulan fibers in each hydration media decreased from 70° to 40° at higher frequencies (Figure 23 A). The loss angle  $\delta$  of the Gellan Gum containing fibers hydrated with double distilled water is lower with 52.5° at 0.1 %. This illustrates that the Gellan Gum content without addition of any ions, modifies the viscoelastic properties of the system as well. It is assumable that the difference is caused by the molecular interactions between Pullulan and Gellan Gum, similar to the results in the previous described rheology section (4.1.1). Gellan Gum blended fibers hydrated with cations had a loss angle  $\delta$  of 20°

at lower frequencies and  $30^\circ$  at higher frequencies. The loss angle  $\delta$  determined by the frequency sweep allows differentiation of the analyzed structure into a gel or a viscoelastic fluid. Gels are characterized by a loss angle  $\delta$  with typical values  $< 45^\circ$ . Values  $> 45^\circ$  indicate a dominating viscous behavior [99]. The Gellan Gum containing fibers, which were hydrated with STF are characterized by a gel-like behavior. In contrast, pure Pullulan fibers show, neither with double distilled water nor with STF, a loss angle  $\delta$  in that range [73]. The described data represent that the electrospinning process transfers the liquid Gellan Gum solution into a solid state, in which the gelling agent is still active and allows gel formation by ion contact. During the rapid electrospinning process the hydrated state of the Gellan Gum in solution becomes transferred into a solid form.

In addition to the gel formation, affect the viscosity profile of the drug delivery system the physiological tolerance of the applied gel. From Figure 23 B) a shear thinning effect of the Gellan Gum blended fibers was observed. At 0.1 Hz the complex viscosity  $\eta^*$  of the STF gelled fibers was 1.92 kPas, with an increase of the shear frequency the viscosity  $\eta^*$  decreased to 0.05 kPas. No other formulation, neither with double distilled water nor with STF showed similar complex viscosities. Considering the fact, that the Gellan Gum blended fibers show a shear thinning effect at higher frequencies, predict a reduced irritation potential compared to solid drug delivery systems like contact lenses or inserts. The acting shear forces at the cornea surface depend on the movement and activity of the eye. When the eye lid is open and the acting shear force is caused by the gravitation, a shear rate of  $1 \text{ s}^{-1}$  can be assumed. During blinking, the shear rate can increase to  $10000 \text{ s}^{-1}$  or higher [100]. Under this aspect it is necessary that the viscosity of the ocular system changes. The Gellan Gum blended fibers show a shear thinning effect with increasing shear rate, which allows adaptation of the gel to the lid-cornea interspace. After blinking, when the gel is not treated with shear forces the viscosity of the system increases again. The increasing viscosity during periods without blinking contributes to a prolonged ocular residence time with less cornea irritation. Through the complex viscosity characteristics, the influence of the cations onto the gelling behavior becomes also more obvious. The Gellan Gum containing fibers hydrated with double distilled water had viscosities equal to the pure Pullulan fibers under absence of cations.

#### 4.1.5 $^1\text{H}$ -nuclear magnetic resonance

To gain information in addition to the performed rheological investigations,  $^1\text{H}$ -NMR relaxometry and diffusion experiments were carried out. In General, these experiments allow a deep insight into the dynamic properties of the water-polymer interactions in aqueous media. NMR allows differentiation of  $T_1$  and  $T_2$  relaxation times. The  $T_1$  relaxation time is well known as longitudinal or spin-lattice relaxation.  $T_1$  is the time which is necessary after an electromagnetic pulse to reach the initial equilibration state of the magnetic species. During resonance the spin interacts with neighboring molecules by dipol-dipol interactions for example. After a  $90^\circ$  pulse, the initial phase coherent spins start dephasing and the transversal magnetization decreases. The decay of transversal magnetization is characterized by the  $T_2$  relaxation time [101].

At first, the results of the relaxometry experiments will be discussed. The  $T_2$  relaxation time enables differentiation between various water species inside the system into mobile and more immobilized molecules. A higher value of the  $T_2$  relaxation time indicates lower binding strength of water and enables free motion of the molecules. Instead, a lower  $T_2$  is characteristic for stronger immobilized water species or samples with higher viscosities [102,103]. In Figure 24 A) the results of the  $T_2$  relaxometry are displayed

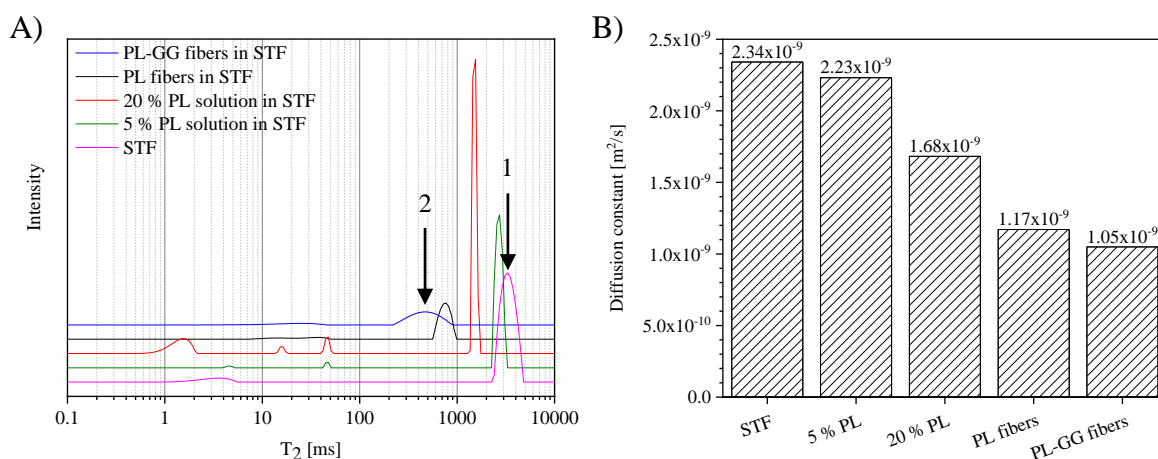


**Figure 24.**  $^1\text{H}$ -NMR experiments of pure STF, 5 % and 20 % Pullulan solution, pure Pullulan fibers and 1 % Gellan Gum-Pullulan blended fibers in STF. All measurements were performed at 34 °C in STF pH 7.4. All concentrations are given in % [w/v]: A)  $T_2$  relaxation time distribution; B) Determination of the diffusion constant ( $n = 1$ ).

For reliable discussion it is necessary to match the obtained  $T_2$  signals to the corresponding proton species, because all components of the investigated samples contain NMR active protons. Pure STF pH 7.4 showed two different  $T_2$  signals, which correlate with two water

species with various mobility. One intense signal at 3293 ms (arrow 1) and a low, broad signal at 3.6 ms. In general, free movable water species are characterized by  $T_2$  relaxation times higher 1000 ms. The free movable water signal shifts to higher or lower relaxation times dependent from the applied temperature.  $T_2$  relaxation times in the lower ms range correlate with stronger water-surface interactions [102]. With rise of the proton interaction, the  $T_2$  relaxation is accelerated. In contrast to liquid systems, where the water can move free, the protons of solid samples are completely relaxed during the described experiments and cannot be determined during the present experimental setup. Therefore, the performance of solid-state NMR experiments are necessary [104,105]. The  $T_2$  relaxation time is affected strongly from the liquid-solid interaction and from the aggregation state as well. The signal at 3.6 ms of STF is caused by bound water to the glass surface of the NMR tube [106]. The signal at 3293 ms (arrow 1) is caused by the main water fraction in the system and correlates with  $T_2$  described in the literature and is characteristic for free movable water in STF [102]. The 5 % Pullulan solution shows three different signals in the  $T_2$  distribution. Two signals with low intensity at 4.6 ms and 47.7 ms were detected as well as the main proton fraction at 2724.6 ms. The  $T_2$  signal at 4.6 ms is caused by water, which is bound to the surface of the tube as well and correlates with the  $T_2$  signal at 3.6 ms of pure STF. The fact, that the amount of surface interacting protons is very low in comparison to the unbound water fraction, results in a decrease of NMR sensitivity and explains the slight difference of the  $T_2$  relaxation time. The signal at 47.7 ms which was not detected in the pure STF distribution is caused by added Pullulan. This signal might come from the polymer protons itself or tightly bound water protons to the polymer [105]. The main proton fraction resulted at 2724.6 ms from the free movable water and shifted to lower  $T_2$ , because the water mobility is reduced by Pullulan addition. By further increase of the Pullulan concentration to 20 %,  $T_2$  decreased to 1542.4 ms. Additionally, three signals with low intensities were obtained at 1.67, 16.3 and 44.8 ms. To assign the determined signals in detail to the acting proton species, further investigations with deuterated Pullulan, Gellan Gum and water would be necessary. But in the present case, the influence of the polymer content on the  $T_2$  between 100 ms and 1000 ms is more interesting for discussion, because of the degree of immobilization of water inside the samples. Pure Pullulan fibers with STF showed a further decrease of the main water signal to 769.6 ms, after Gellan Gum addition to the nanofibers the main water fraction signal becomes more reduced to 464.2 ms with intense broadening (arrow 2). With the rise of the Pullulan concentration,  $T_2$  of the main water fraction

decreased, which indicates a stronger immobilization inside the polymeric network. Pullulan as polysaccharide is characterized by a high content of hydroxyl groups, which are able to interact with the water molecules by dipolar interactions. As consequence, a higher immobilization of water inside the systems was observed. A further decrease of the water mobility was obtained after Gellan Gum addition to the fiber matrix. The  $T_2$  distribution started broadening, because rising of potential water-polymer interactions. The hydrogen bond formation caused by the hydroxyl groups, the anionic nature of Gellan Gum and the stereochemistry of the polymer chains play a major role during the obtained  $T_2$  distribution. Nevertheless, the difference between pure Pullulan and Gellan Gum containing fibers illustrate that water is more immobilized after Gellan Gum addition. Which is caused by the fact that ionic interactions are quite strong and have also a longer distance compared to dipolar interactions. The NMR data are in line and complementary with the discussed results of gel formation during the rheological experiments.

In addition to the relaxometry, the diffusion constant  $D$  of water inside the samples was analyzed. The diffusion constant provides information about the diffusion velocity inside the polymer network. The  $T_2$  relaxation time of the protons lower 100 ms (Figure 24 A) is shorter than the diffusion time of 400 ms during the diffusion experiments, because of this these protons are completely relaxed and were not detected during the experiments. In this case only protons with  $T_2$  relaxation times higher than the applied diffusion time are detectable. Figure 24 B) displays the data of the diffusion experiments. Pure STF had a diffusion constant of  $2.34 \times 10^{-9} \text{ m}^2/\text{s}$ , 5 % Pullulan  $2.23 \times 10^{-9} \text{ m}^2/\text{s}$  and 20 % Pullulan  $1.68 \times 10^{-9} \text{ m}^2/\text{s}$ . Pure Pullulan fibers had a diffusion constant of  $1.17 \times 10^{-9} \text{ m}^2/\text{s}$  and Gellan Gum containing fibers  $1.05 \times 10^{-9} \text{ m}^2/\text{s}$ . With an increase of the polymer amount the diffusion constant decreases as well. The diffusion constant  $D$  of the Gellan Gum blended fibers is lower than  $D$  of pure Pullulan fibers. The network formed by Gellan Gum-Pullulan prevents more free motion and diffusion of the water, compared to the pure Pullulan fibers. This illustrates the stronger immobilization of water inside the *in situ* formed gel. The diffusion coefficient of the entrapped drug inside the gel affects next to the diffusion of water the release of APIs. Drug release from the hydrogel is controlled by the density and pore size of the polymer network caused by cross-linking, polymer chain interactions and the diffusivity of the drug. Furthermore, the physicochemical properties like charge, molecular weight and



size affect the release of APIs. A decrease of the diffusion coefficient inside gels leads to prolonged release times [107,108].

#### 4.1.6 Curvature formation

The geometry of the drug delivery system influences the application, bioavailability, release profile, therapeutic efficacy and the extent of side effects. Hence, a dosage form with adapted geometry is necessary especially for treatment of the ocular surface with inserts or contact lenses [17,109,110]. The adjustment of the geometry to the physiological and anatomic conditions *in vivo* is essential to increase the ocular residence time and bioavailability. This illustrates, that the contact between the drug delivery system and the ocular surface is important to reach a sufficient therapeutic efficiency.

As guidance, the anatomic dimensions of porcine eyes were used. Anatomy and geometry of the porcine eye are quite similar to the human eye [73]. It is described that the horizontal diameter of the porcine bulb is 14.9 mm and the vertical diameter is 12.4 mm [111,112]. The human curvature is reported to range between 7.10-8.75 mm [113]. After electrospinning the prepared meshes were punched out to spherical slices with 15 mm diameter. Immediately after the electrospinning process, the spun fibers were planar with approximately 50 mm diameter. The planar structure and the large size of the prepared sample are not suitable for cornea application, because of the flat structure the mesh do not fit to the curvature of the eye and prevent homogenous distribution at the ocular surface. With the lateral protruding excess of the planar mesh at the cornea surface, the lid blink would shear-off the drug delivery system from the eye.

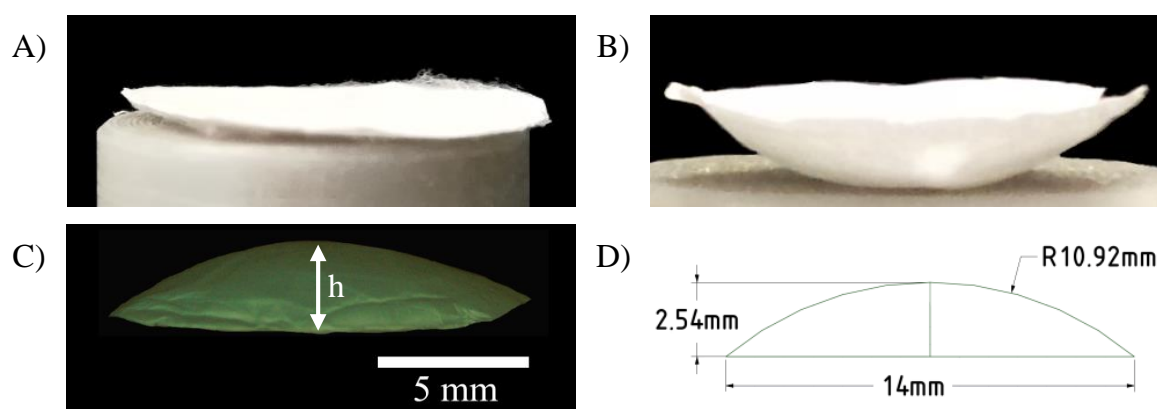


**Figure 25.** Different images of the electrospun lens: A) Planar lens before curvature formation; B) Lens after curvature formation; C) Reflecting microscope image of the lens after curvature formation; D) Determination of the lens curvature via DesignSpark Mechanical software.

In Figure 25 A) the planar punched out mesh with 15 mm diameter is displayed. The mesh curvature was adjusted with a 3D printed matrix described previously. Figure 25 B) displays the lens after curvature formation with the 3D printed matrix. Differences between the lens geometry before and after curvature formation are clearly visible in the images A) and B). The electrospun lens is flexible enough to adapt to the 3D printed matrix and sufficient malleable to allow dimensionally-stability after forming. The flexibility of the fibers is sufficient to prevent breaking during the forming process. Caused by curvature formation and lens bowing, the diameter of the lens decreased from 15 mm to 14 mm. With 14 mm diameter the lenses were precise adapted to the size of the porcine eyes used in the following *in vitro* experiments. Determination of the lens curvature was performed by the reflecting microscope. One of the captured images is displayed in Figure 25 C) with the measured height  $h$ . A height of  $2.54 \text{ mm} \pm 0.38 \text{ mm}$  was measured in the images. The lens diameter and the measured height  $h$  were used to construct a lens with DesignSpark Mechanical 2.0 CAD software and to calculate the curvature of the lenses (Figure 25 D). By lens construction, the curvature was determined to 10.92 mm [73]. The prepared curvature is sufficient to apply the drug delivery system to the porcine and human eyes. To ensure the lens application to the human eye during the *in vivo* experiments the prepared lenses had to be adjusted to 8 mm diameter with similar curvature described in the present section.

#### 4.1.7 Nanoscale 3D x-ray imaging

The ESEM images discussed previously confirmed that the electrospun fibers form a three dimensional network in the middle nanometer range. Nano-CT allows the 3D visualization of the fibers by phase contrast occurred by varying interactions between x-ray radiation and the fiber material [114,115]. The obtained x-ray radiation phase shift induces the contrast that is used for detection. Nano-CT is a new non-destructive method, which gives more information about the three dimensional inner structure of the samples in addition to the information of the standard methods mercury porosimetry and gas adsorption [73,115]. Considering the *in vivo* application, the speed of hydration with the physiological tear fluid is essential for the *in situ* gelation process. In practice, the lens is instilled into the eye and has to be hydrated immediately after tear fluid contact. Hence, detailed information about the inner structure like porosity, pore interconnectivity, fiber alignment, surface area and size distributions are necessary. Figure 26 displays different virtual cuts of the 1 % Gellan Gum containing fibers.

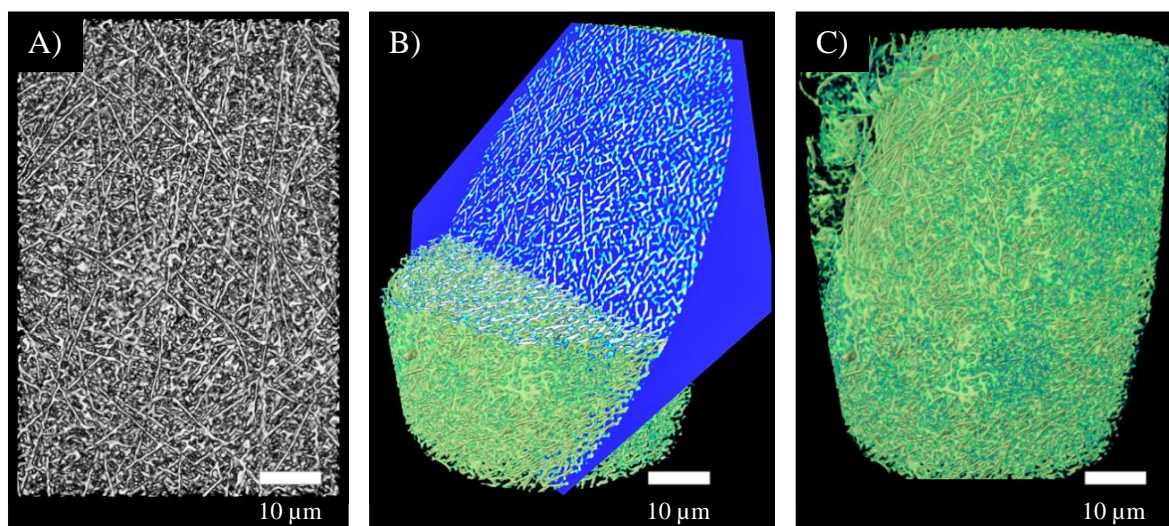


**Figure 26.** Virtual cut of an exemplary sample composed of 1 % Gellan Gum containing Pullulan fibers: A) Volume after single cut is shown; B) Binarization of the image with pseudo-colored fibers in green, the virtual cut in blue; C) Entire volume of investigated sample.

Figure 26 A) shows a single cut of the fiber image. This image illustrates that the fibers had an anisometric orientation inside the prepared lens, because different cross sections of fibers are visible. Some fibers are sectioned longitudinal and others in cross section. Considering the electrospinning process, these results are plausible, because the polymer jet which was ejected from the needle tip and underlies a lateral deflection, caused by different physical instabilities of the polymer stream and fibers in planar, randomized alignment were obtained. A three-dimensional reconstruction of the fibers, followed by image processing enabled the estimation of the porosity of the samples to be  $85.5 \% \pm 0.5 \%$ . Furthermore, the pore interconnectivity was equal to 99 % [73]. These results make clear, that nearly all pores are connected to each other, in contrast to a sponge structure where the pores are observed as individuals. Considering the spinning process, the formed polymer stream solidifies as fibers, depositing layer by layer so that all interspaces are connected to each other. High porosity and pore interconnectivity enables fast water penetration and gelling of the fibers, which are key aspects for the following application. In addition to the pores, the surface area of the sample influences the hydration velocity. The surface area of the electrospun fibers was estimated to  $7.9 \mu\text{m}^2/\mu\text{m}^3$ .

In Figure 27 the calculated fiber size distribution of the nano-CT measurements is displayed. The average fiber diameter was determined to  $317 \text{ nm} \pm 42 \text{ nm}$ . In contrast to the ESEM measurements, where the mean fiber diameter was  $398 \text{ nm} \pm 44 \text{ nm}$ , the fibers in the nano-CT measurement are smaller. The difference between the diameters can be explained

by the various imaging techniques. ESEM is a 2D and nano-CT is a 3D imaging method. ESEM allows imaging of the sample surface as well as the average diameter, but the diameters of only 100 fibers were measured. The result of the nano-CT instead allows investigation of the whole fiber samples in x-y-z orientation, but it is a time-consuming technique. The measurement time of one Pullulan-Gellan Gum sample was 9 h and also similar time was necessary to perform the qualitative dataset processing after the measurement. However, nano-CT provides a 3D datasheet that enables the estimation of the average diameter of the fibers in all three directions and takes account into the variability of the fiber diameter in all three directions. In that case, nano-CT is able to produce more statistically relevant quantification of the data compared to other methods.

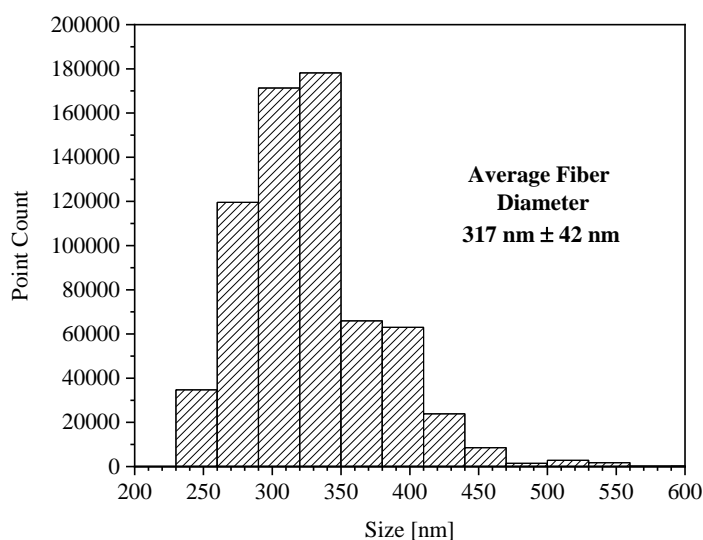


**Figure 27.** Fiber size distribution of 1 % Gellan Gum containing Pullulan fibers determined with nanoscale x-ray 3D imaging.

In Figure 28 A) a gray scale image of the analyzed Pullulan-Gellan Gum mesh is displayed. In B) the gray scale image is colored into size fractions from 128 nm to 400 nm. The main fiber size fraction in the image is colored in green which correlates with 317 nm. Less fibers are displayed in blue and in red. These images illustrate the homogenous distribution of the fiber size distribution in three dimensions and underline an observed narrow size distribution. Nano-CT is an innovative method to produce volumetric data of samples with sizes in nanometer range. It has the limitation, that the produced dataset has to be in the  $\mu\text{m}$  range and therefore, imaging of the whole electrospun lens with 14 mm diameter and 4 mg weight information is not possible. However, the consistency of the obtained results for fiber diameter and porosity for three different samples with the same composition support the

determined data. These data show that phase-contrast based nano-CT is a suitable technique for Pullulan nanofiber imaging to gain information about the size distribution, surface area, porosity, pore interconnectivity and 3D structure inside the samples.

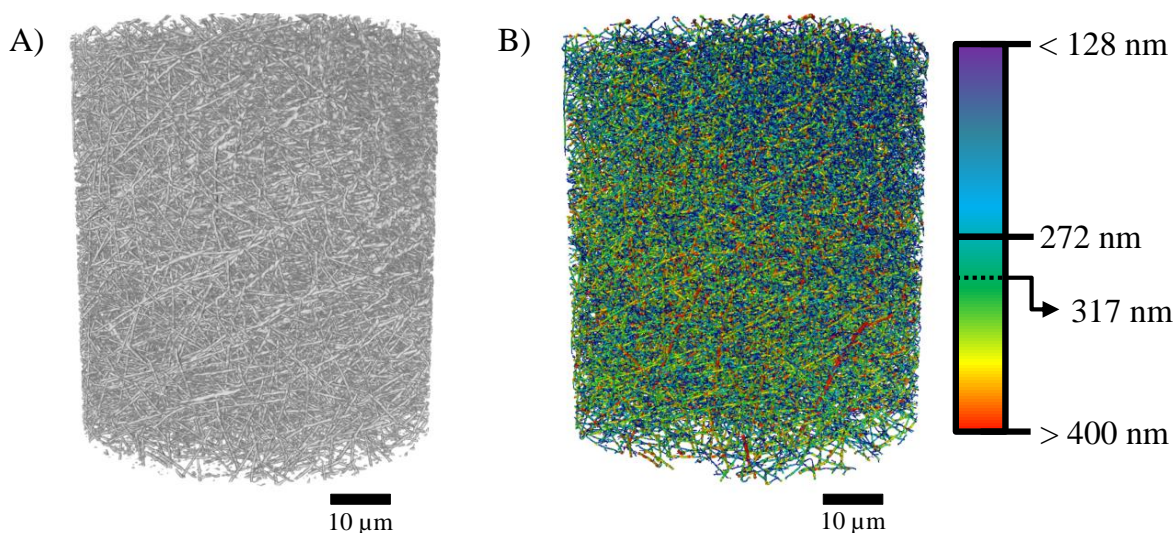


**Figure 28.** X-Ray 3D image of Pullulan fibers containing 1 % Gellan Gum: A) Gray scale image; B) 3D fiber size distribution in various colors including the mean fiber diameter at 317 nm.

#### 4.1.8 Ocular residence time *in vitro*

The ocular residence time is a major task for ocular drug delivery systems. A prolonged residence time at the ocular surface increases the bioavailability, reduces side effects and the instillation frequency. A decrease of the application frequency will lead to better patient compliance and satisfaction. This is the reason why high adapted *in vitro* models for the determination of the ocular residence time are essential for development of new drug delivery systems. Until the present day, no suitable *in vitro* model is available which mimic the exact physiological conditions of the human eye. Hence, the residence time has to be determined often *in vivo*. The most common used method *in vivo* is based on gamma scintigraphy [116]. But because of critical ethical aspects, *in vivo* experiments come along with high costs and analytic effort. Further, those costs and effort occur in the late state of a research. Nevertheless, insufficient ocular residence time is an exclusion criterion of new ocular drug delivery systems. Therefore, it is necessary to gain information about the ocular residence time during the early state of the research, which allows improvement and adaptation of the drug formulation. Hence, suitable *in vitro* models are necessary to reduce the number of *in vivo* experiments and contribute to an early decision about which formulation might be a promising candidate for further investigations.

The physiological barriers of the human eye, especially the cellular structure, the low tear volume of 7.0-9.7  $\mu\text{l}$  and rapid tear turnover from 1.0-1.2  $\mu\text{l}/\text{min}$  are high challenging tasks for *in vitro* mirror of the *in vivo* situation [117,118]. Only a few *in vitro* models are available to determine the ocular residence time. In the literature the tear-turnover apparatus is described [119]. During this experimental setup a planar multilayer of immortalized cornea epithelial cells (iHCEC) are seeded onto a transwell polycarbonate filter. The cell loaded transwell is placed into a thermostat bath with 34 °C. The tear flow is simulated by a peristaltic pump, followed by HPLC analysis of the sample concentration. A simple cellular structure with a missing 3D ocular anatomy, ocular curvature, vertical model position and the use of high tear fluid volumes do not allow exact simulation of the ocular conditions. Furthermore, this method does not allow air liquid interaction of the samples to mimic the real conditions of cornea surface and only liquid dosage forms can be analyzed.

Another *in vitro* model to determine the mucoadhesive properties of particulated formulations in nanometer size is based on the measurement of the zeta potential and turbidity. Therefore, the nanosized systems are mixed with negatively charged mucin, followed by determination of the zeta potential and the turbidity after incubation at defined temperatures. The alteration of the zeta potential and turbidity based on the mucin interaction is correlated with the mucoadhesive properties of the system [120]. The described model is based on the mucin-drug delivery system-interaction and do not consider the cellular aspects like membrane complexity, tear volume, tear turnover, bulbus anatomy and lid blink. Furthermore, the described model is only suitable for investigations of colloidal dispersions like liposomes or nanoparticles. These formulations are able to interact electrostatically with mucin, which can be determined by zeta potential measurement. Especially the impact of non-electrostatic mucoadhesive forces between the drug delivery system and mucin (e.g. caused by disulfide bonds or steric interaction) cannot be detected by examining the alteration of the zeta potential.

An alternative *in vitro* model, that determines the mucoadhesive properties described in the literature, is based on the interaction of the drug delivery system with extracted porcine ocular cornea or intestinal mucosa. The extracted tissue is fixed at a half cut falcon tube, which is placed in 45° angle into an incubation chamber with 100 % relative humidity and temperature at 37 °C. After tissue fixation, the drug delivery system is marked with a fluorescence dye and loaded to the cellular layer. The layer is rinsed with tear fluid buffer at



constant flow rates. The rinsed buffer is collected in defined time periods and quantified by fluorescence [121,122]. Different aspects of this experimental setup have to be discussed. First, the applied tube curvature and the 45° position are not comparable to the anatomical eye orientation *in vivo*. Furthermore, this model does not allow the evaluation of the 2D sample distribution over the cellular layer. But in contrast to the prior described *in vitro* models, this experimental setup enables the investigation of drug delivery systems independent from size and allows determination of the cellular interaction with sensitive fluorescence quantification.

To overcome the described disadvantages of the available *in vitro* models, a new and innovative model was developed to reach a higher *in vitro-in vivo* correlation. Figure 29 displays the components of the developed 3D printed moistening chamber for *in vitro* experiments.

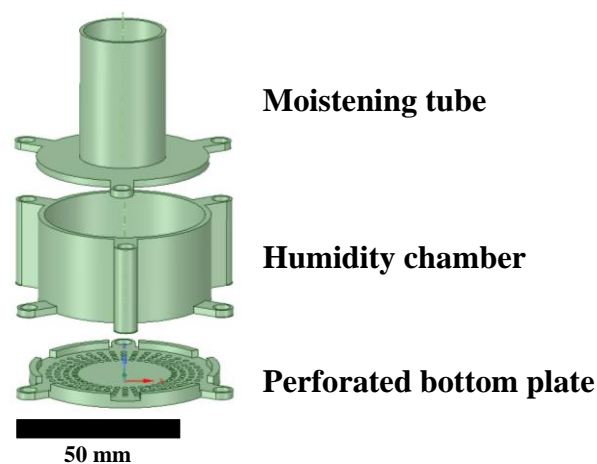


**Figure 29.** Scheme of the components of the 3D printed moistening chamber.

The system contains a moistening tube which allows STF instillation via spray application. The moistening tube is connected with a humidity chamber which prevents rapid evaporation of the applied STF to ensure sufficient relative humidity inside the chamber. A perforated bottom plate with a rubber disk placed at the center shuts the chamber at the opposite side. The rubber disk allows fixation of the porcine eyes. The use of fresh extracted porcine eyes ensures high quality simulation of the physiologic ocular conditions with intact cornea, cellular structure and eye curvature in combination with vertical position of the moistening chamber. Pressure equalization inside the moistening chamber during spray application is allowed by the perforated bottom plate. All elements are connected with screws, which ensure a fast removal of the eye loaded bottom plate for a quantification by multispectral

fluorescence imaging (MSFI). The manufacturing process of the chamber by 3D printing ensures individual adaptation of the chamber geometry like perforation degree, bottom plate diameter and length of moistening tube. Reproducibility, low price and quick manufacturing make the developed moistening chamber a promising model for further experiments. The tear flow was simulated *in vitro* with 56  $\mu$ l STF per spray application. Combination of the moistening chamber with MSFI allows fluorescence quantification as well as information about the spatial distribution of samples and will expand the known *in vitro* models for ocular residence time. On the other hand, the developed model does currently not allow the adjustment of the physiological temperature, but this challenge can be overcome by using a heating jacket which covers the moistening chamber during the *in vitro* experiments. It is well known that physicochemical properties like viscosity are strongly affected by the applied temperature. The moistening chamber could not replace indispensable *in vivo* experiments, but the model allows differentiation of the drug delivery systems independent from the size in an early state of research and contributes to a reduction of animal experiments.

Figure 30 displays the fluorescence images of fluorescein sodium eye drops, fluorescein sodium and DiR-PLGA nanoparticle loaded fibers after treatment with different numbers of spray applications. All fluorescence signals are displayed as heat map images and consist as an overlay of the gray scale images. The electrospun fibers allowed application in solid state. After administration of the fibers to the porcine eye, the mesh dissolved quickly and a hydrogel was formed at the cornea surface. In contrast to the *in situ* formed gel the fluorescein sodium eye drops stayed liquid during the performed experiments. The images of the fluorescein sodium eye drops show, that immediately after eye drop instillation ( $t_0$ ) a drop shape distribution at the cornea center was obtained. In contrast to eye drops, both fiber signals showed a larger and more homogenous distribution over the cornea surface. The fluorescein sodium fibers showed at the lower ocular section as well as the DiR signal at the left ocular section regions with higher initial fluorescence intensities ( $t_0$ ). These regions are caused by the spherical anatomy of the bulb. Gravimetric and lateral forces induce sample flow to the side regions of the eye. The dissolved fluorescein sodium loaded fibers show more concentrated spots in the lower part of the bulb. The DiR loaded fibers (Figure 30, right,  $t_0$ ) show higher concentrations at the left bulb section.



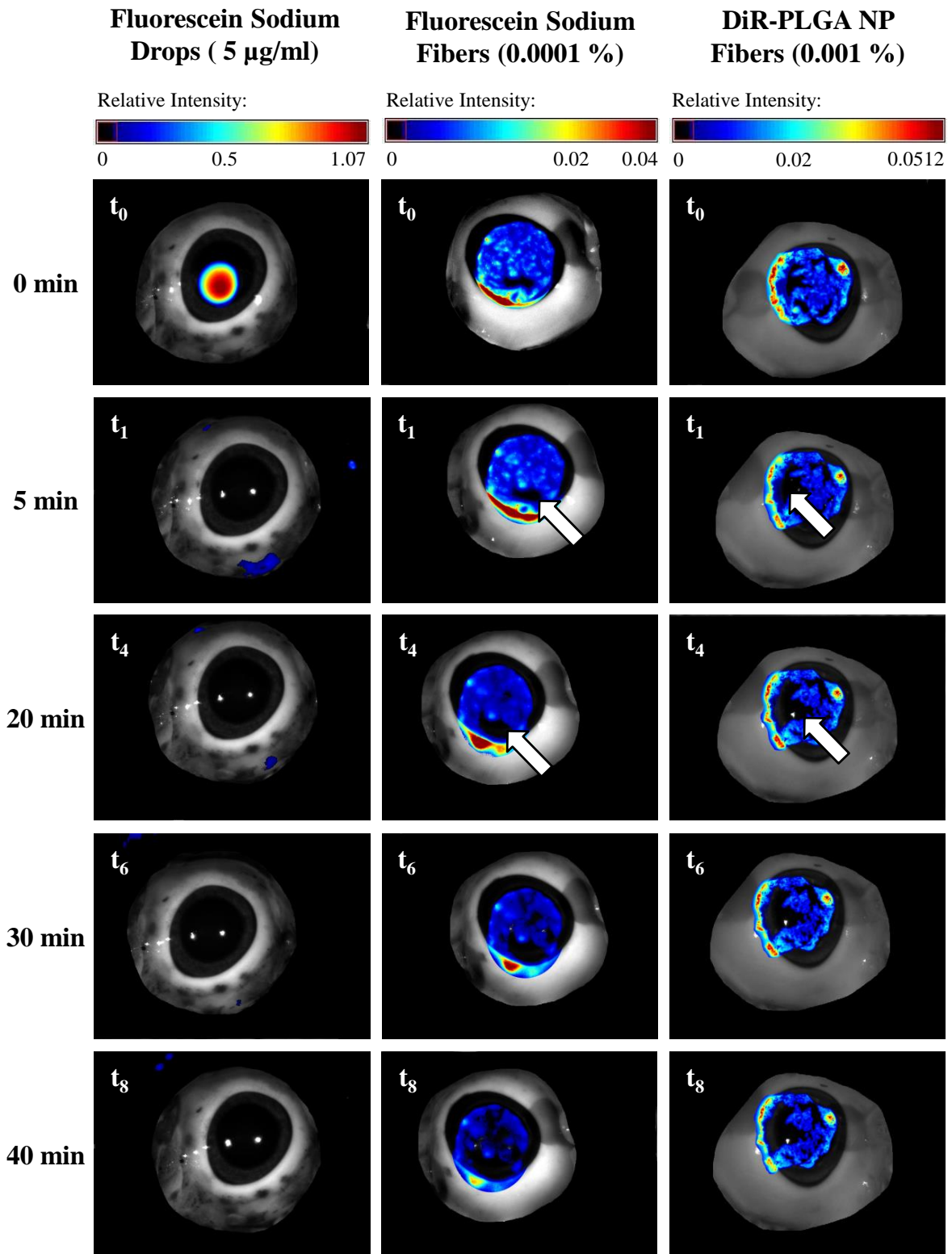


**Figure 30.** Heat map images of porcine eyes treated with 5  $\mu\text{g}/\text{ml}$  fluorescein sodium eye drops (left), 0.0001 % fluorescein sodium loaded fibers (middle) and 0.001 % DiR-PLGA nanoparticle loaded fibers (right) ( $n = 3$ ).

Especially the DiR hot spots located at the left side of the eye are caused by the lateral flow of the gel around the ocular curvature. In contrast to the fiber signal, the eye drop

fluorescence signal disappeared immediately after the first spray application ( $t_1$ ). Just a few fluorescence spots placed out of the cornea center were detected. In contrast to the eye drops, signals of the fiber formulations (Figure 30, middle and right,  $t_1$ ) were still detected, which underline further gel contact to the ocular surface. Over time, the gel containing fluorescein sodium as well the DiR showed regions without signals (Figure 30, middle and right, arrows), which increased over time. After the spray application, the signal decrease was not homogenous. Caused by the electrospinning setup the fiber deposition at the collector plate is randomly, triggered by different regions of isolation at the collector surface. Hence, the thickness of the electrospun mesh can vary over the sample. To overcome these problems an electrospinning setup with other collecting units like the rotating drum or mandrel collector can be used to gain more homogenous mesh thickness [123–125]. In addition to homogenous sample thicknesses, the rotating collector units allow exact one direction fiber alignment. After eight spray applications ( $t_8$ ) the DiR and fluorescein sodium signal were still detected. The signal intensity of the fiber hot spots located at the side section of the porcine eye decreased in progression with the moistening process. It is well known that the viscosity of the drug delivery system affects the ocular residence time and the bioavailability. Therefore, semi-solid dosage forms were applied to the eye to prolong the residence time. Higher viscosities increase the resistance of drug delivery systems against the spray application [116,126,127]. The low viscous fluorescein sodium eye drops showed no resistance against the treatment with STF.

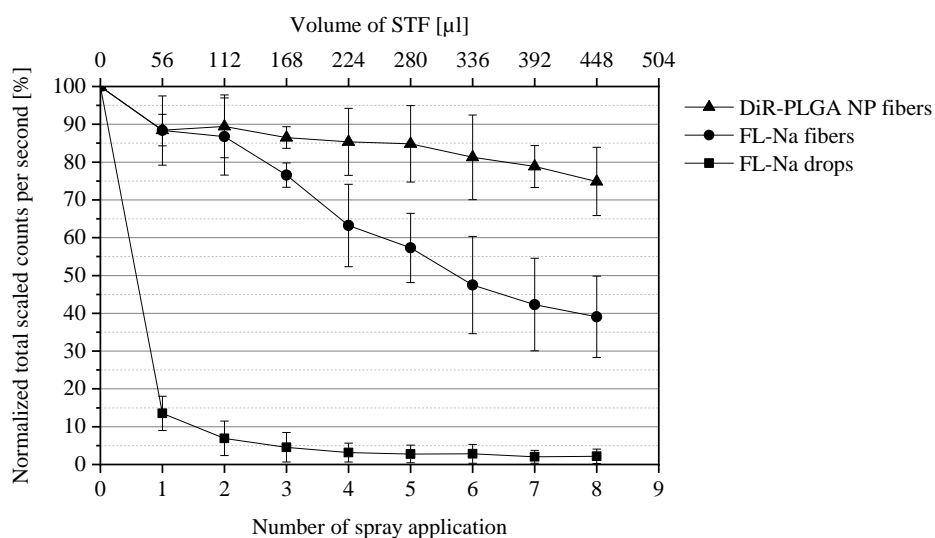


**Figure 31.** Fluorescence quantification of residual fluorescein sodium (FL-Na) and DiR-PLGA nanoparticle loaded Pullulan-Gellan Gum nanofibers and fluorescein sodium loaded eye drops (mean  $\pm$  SD,  $n = 3$ ).

In addition to the fluorescence images, which provided information about the local distribution of the drug delivery system, the fluorescence signal was quantified. These data are displayed in Figure 31. The eye drops showed after the first spray application a decrease to 15 %, after two applications to 7.5 % and after three applications to 5 % of the initial signal. The fluorescein as well as the DiR signal of the fibers showed a decrease to 88 % of the initial signal after the first spray application. After two applications, both signals stayed constant. After the third application, the residual signal intensities of DiR and fluorescein sodium in the fibers drifted apart. Fluorescein sodium reached a value of 76 % and DiR stayed constant at 86 %. As consequence of the following eight spray applications, fluorescein sodium reached 40 % and DiR reached 75 % of the initial signal intensity. These results illustrate, that the electrospun fibers increase the ocular residence time in comparison to conventional eye drops.

The entrapment of PLGA nanoparticles into fibers is sufficient to prolong the ocular residence time *in vitro*, compared to the formulation with the fluorescein sodium signal. The clearance of the investigated samples depends on the physicochemical properties of the entrapped dye. Fluorescein sodium as hydrophilic dye was faster removed from the cornea surface as the lipophilic DiR entrapped inside PLGA nanoparticles. Hence, the partition coefficient ( $\log P$ ) of the used dyes affects the ocular residence time and contributes to the ocular clearance. Since there are no experimental determined  $\log P$  values for DiR described in the literature, a predicted partition coefficient was used. All  $\log P$  values were predicted by [www.molinspiration.com](http://www.molinspiration.com) using the simplified molecular-input line entry system (SMILES) to guarantee equivalent prediction properties [128]. The predicted  $\log P$  of DiR is 10.6, what underlines the high lipophilicity of the dye. In contrast to DiR, fluorescein sodium is a more hydrophilic dye with a  $\log P$  of 0.92 [128–130]. Theoretical predicted values deviate from the experimental determined values. Fluorescein for example shows in experimental setups a partition coefficient in octanol-water of -0.08 at pH 7.5. Nevertheless, the predicted values are sufficient to compare the physicochemical properties *in vitro* [131]. The distribution between the water phase and the epithelia surface during the spray application will affect the clearance by STF. Is the water-dye interaction reduced, is the rinsing effect and clearance reduced as well. During the experiments, the release of DiR from the PLGA nanoparticles cannot be completely excluded because of the high water content of the hydrogel. But the DiR release can be neglected, considering the high lipophilic

properties of dye as well as the short incubation time of the dye loaded nanoparticles. Therefore, the determined fluorescence signal correlates with the availability of the nanoparticles at the cornea surface and not with the released dye molecules outside the particles in a meaningful manner. In general, different mechanisms for mucoadhesivity or ocular residence time were discussed for covalent and non-covalent binding polymers in literature. The non-covalent binding polymers were categorized in neutral, anionic and cationic ingredients. Anionic polymers like Gellan Gum or polyacrylic acid (-COOH) as polar ingredients are able to form hydrogen bonds between the carboxylic groups and the surface structures of the oligosaccharides of the mucus [132]. In addition to hydrogen bond formation, the carboxylic groups of Gellan Gum increase the absorption of water from the covered mucus layer which result in a higher penetration depth into the mucus [133]. The increased ocular residence time for the Gellan Gum containing fibers can be explained by interplay of hydrogen bond formation of the carboxylic groups, swelling and the rising viscosity at the ocular surface. In contrast to the described non-covalent binding polymers contain the covalent binding polymers chemical groups, which react with components of the mucus layer. Especially thiol containing polymers like chitosan-N-acetyl cysteine or chitosan-thioglycolic acid, allow reversible chemical reactions with the physiological thiol groups containing mucus under formation of disulfide bonds which result in an increase of the mucoadhesive properties [134–136].

## **4.2 Drug loaded electrospun nanofibers**

### **4.2.1 Nanoparticle loaded nanofibers**

#### **4.2.1.1 Nanoparticle characterization**

In the following section the size distribution of different nanoparticle formulations will be discussed. Therefore, the mean hydrodynamic diameter (z-average) and the polydispersity index (PDI) of different PLGA-AmpB formulations are displayed in Figure 32 A). The figure shows different ratios of AmpB and PLGA before and after purification. The z-average of the 1:100 ratio was 129.8 nm and the PDI was 0.058. After increasing the AmpB ratio to 1:20, the z-average increased to 203.4 nm and the PDI to 0.209. The highest added amount of AmpB (1:10) showed a diameter of 251.9 nm and a PDI of 0.239. All samples contained DMSO immediately after preparation. DMSO as non-volatile solvent cannot be removed by evaporation, the particles had to be purified by centrifugal filtration. Because of the high purification effort, the DMSO containing nanoparticle dispersions were

analyzed first to gain information about the particle size distribution. By increasing the amount of initially used drug, the mean size of the particles increased as well as the PDI.

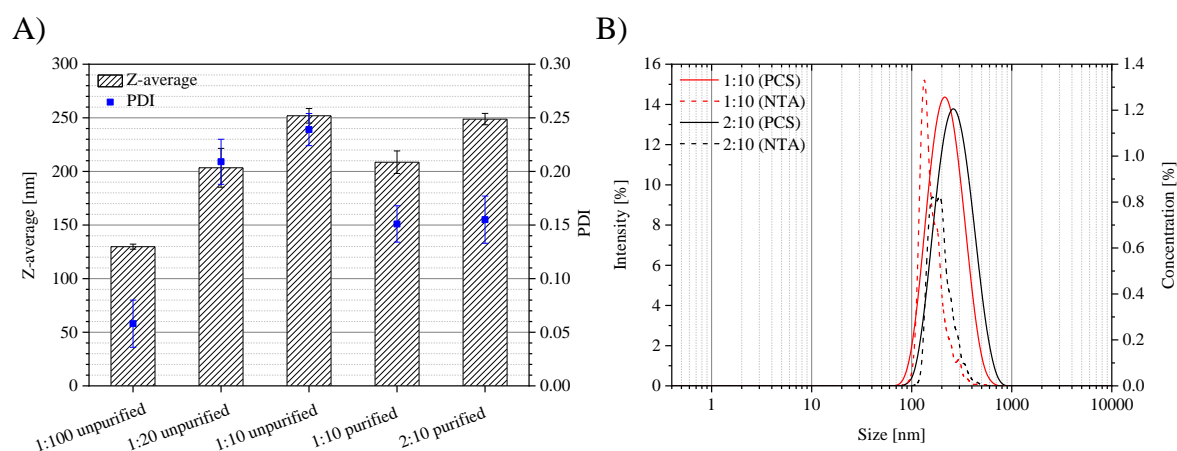


**Figure 32.** Results of the nanoparticle size determination: A) Z-average and PDI of the dynamic light scattering experiments (PCS) of different AmpB-PLGA nanoparticle formulations before and after purification; B) Nanoparticle size distribution of purified AmpB-PLGA 1:10 and 2:10. Size distribution determined by dynamic light scattering (PCS) (solid lines) and nanoparticle tracking analysis (NTA) (dashed lines) (mean  $\pm$  SD,  $n = 3$ ).

For nanoparticle stabilization, surface active ingredients like PVA, Poloxamer 188 or blended surfactants are necessary to prevent particle agglomeration [76]. PVA ensures steric stabilization of the nanoparticle dispersion and allows irreversible association of PVA to the particle surface [137]. The amphiphilic AmpB may compete with PVA at the PLGA-water interface during precipitation. As consequence, an increase of z-average and PDI was observed. After nanoparticle purification, the z-average of the 1:10 ratio is 208.6 nm with a PDI of 0.15. The ratio of 2:10 showed a z-average of 248.8 nm and a PDI of 0.155 [138]. With increased drug load, the particle size increased as well. It is remarkable that after the purification steps the PDI of the nanoparticle dispersion decreased. Reasons for this are the performed purification steps, where non-entrapped AmpB and PVA excess were removed. In Figure 32 B), the size distribution determined by PCS and NTA of purified nanoparticle dispersions are displayed. Both techniques illustrate that each particle size distribution is monomodal without particles larger than 1000 nm. The data of the NTA as well as the PCS show a size shift to larger particles after increasing the initial amount of AmpB, which correlates with the previous discussed results. In Table 7 the drug load, entrapment efficacy and size distribution of the purified nanoparticle are summarized. The NTA measurements show that the mean diameter of the 1:10 ratio is 179.5 nm and of the particles with the higher

ratio it is 213.2 nm [138]. The diameter determined by NTA and PCS differ, because of different measurements principles and particle size calculation models.

**Table 7.** Characteristic values of different AmpB-PLGA nanoparticle ratios (1:10 and 2:10) after purification (mean  $\pm$  SD,  $n = 3$ ).

	Drug load [%] m/m	Entrapment efficacy [%] m/m	Z-average PCS <sup>a</sup> [nm]	Mean Size NTA <sup>b</sup> [nm]	$\zeta$ -Potential [mV]	
					STF	PBS
					pH 7.4	pH 7.4
<b>1:10</b>	3.9 $\pm$ 0.47	40.15 $\pm$ 2.15	208.6 $\pm$ 10.5	179.5 $\pm$ 7.5	-0.79 $\pm$ 0.14	-0.72 $\pm$ 0.14
<b>2:10</b>	7.2 $\pm$ 0.58	37.09 $\pm$ 5.09	248.8 $\pm$ 5.3	213.2 $\pm$ 18.7	-0.74 $\pm$ 0.47	-0.69 $\pm$ 0.22

<sup>a</sup> Photon Correlation Spectroscopy

<sup>b</sup> Nanoparticle Tracking Analysis

During PCS, the intensity weighted hydrodynamic diameter was used, where particles with larger sizes  $d$  were weighted higher than smaller particles, which results in a proportional increase of the measured intensity  $I$  to the six power of the particle diameter ( $I \sim d^6$ ). In contrast to PCS, NTA detects the diffusion lengths of single particles and transforms the determined diffusion distance into the particle size. The size calculated equal to this method is more independent from light scattering phenomena, because the number weighted particle size distribution is determined ( $I \sim d^1$ ). Compared to PCS, NTA has advantages regarding size resolution. However, it does not detect materials below 20 nm and requires high dilution in order to obtain and to track single particles, which move independently from each other. Because of the fact, that only a few particles (e.g. 50-70) are monitored, the statistical power of NTA is smaller compared to PCS. The NTA results show that the distribution width increases by increasing the amount of initial added drug, which correlates with the slightly increase of PDI determined in the PCS experiments. The drug load of the purified nanoparticle formulations increased with the initial added drug from 3.9 % to 7.2 %. The entrapment efficiency showed no difference between both drug-polymer ratios with 40.15 % (1:10) and 37.09 % (2:10). 60 % of the initial used AmpB was outside the PLGA particles and was removed by the described purification steps.

The zeta potential of the AmpB loaded nanoparticles is given in Table 7 as well. Amphiphilic, non-charged polymers like PVA are well known for their charge shielding effect during nanoparticle stabilization. As consequence of this phenomena, the prepared

nanoparticles were charged neutral [139,140]. No influence of the used buffer systems PBS and STF was recognized at pH 7.4.

## 4.2.2 Eudragit L-Amphotericin B-polyelectrolyte complex

### 4.2.2.1 UV/Vis-spectroscopy

To gain information about the polyelectrolyte complex formation the UV/Vis spectra of the unprocessed drug and the complex were investigated. The absorption spectrum of AmpB varies depending on the aggregation state of the drug. The monomeric form is characterized by four different absorption maxima with the highest at 405-409 nm [141]. Caused by their chemical structure, the AmpB molecules are able to interact with each other by hydrophobic, polar or ionic forces. Hence, the increase of the drug concentration induce a hypsochromic shift of the absorption with an absorption maximum at 328 nm to 340 nm what is assigned to formation of dimers [142]. Depending on the molecular interaction with lipids, surfactants or polymers AmpB shows also a shift of the absorption spectrum to other wavelengths. The commercial drug formulation Fungizone<sup>®</sup>, which consists of AmpB, sodium desoxycholate as solubilization agent and of different buffer ingredients, shows in aqueous solution an absorption maximum with a broad band at 328 nm [143,144].

Figure 33 shows the absorption spectrum of monomeric AmpB dissolved in methanol, AmpB-Eu L polyelectrolyte complex (3:3) dissolved in double distilled water and the complex dissolved in a 50 % v/v mixture of methanol-water.

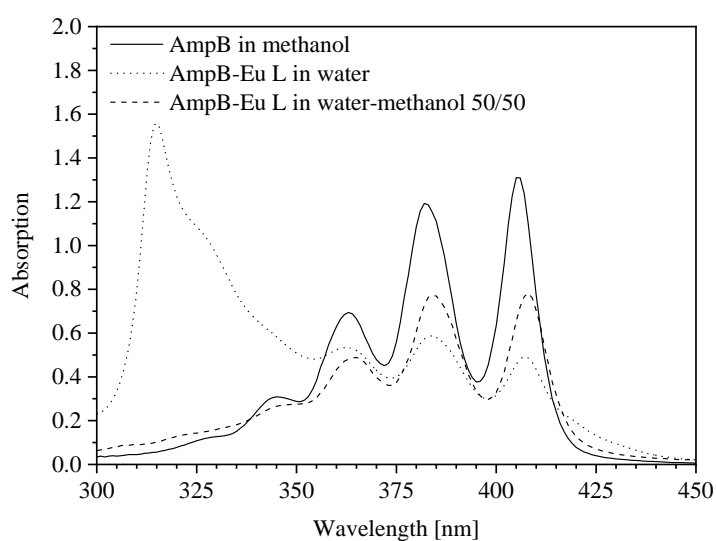


**Figure 33.** Absorption spectra of monomeric AmpB in methanol, AmpB-Eu L polyelectrolyte complex (3:3) in double distilled water and in water-methanol 50 % v/v ( $n = 3$ ).

The pure drug dissolved in methanol is characterized by the monomeric AmpB spectrum with four different absorption maxima at 405, 382, 363 and 345 nm. In contrast, the polyelectrolyte complex shows a change of the spectral shape with an extinction max at 315 nm. The difference between the monomer and the complex spectrum illustrates, that complex formation was occurred. These results correlate with previous described experiments in the literature where a non-covalent complex of AmpB with poly( $\alpha$ -glutamic acid) was prepared [78]. Furthermore, it is obvious that the ratio of the extinction maxima at 405, 382 and 363 nm changed after complex formation. The complex solution was diluted with methanol, afterwards the UV/Vis spectrum has been recorded. As consequence, the complex spectrum changed similar to the AmpB monomer spectrum with a lower absorption. These results allow the hypothesis that AmpB was bond non-covalently to Eu-L. This let assume that drug and polymer are connected via cationic-anionic interactions, caused by the amine function of AmpB and the carboxylic function of Eu-L. By addition of methanol the ionic interaction between Eu-L and AmpB was interrupted, which was followed by dissociation of the complex. Another reason for the described phenomena is conceivable. In methanol the solubility of AmpB (2000 mg/l) is higher compared to water (< 1 mg/l, pH 6-7) [68]. Therefore, methanol may act as a co-solvent where the drug starts solvation in the surrounding medium what results in changing to the described monomer spectrum.

#### 4.2.2.2 ATR-IR-spectroscopy

To gain a deeper insight into the molecular organization of the AmpB-Eu L complex ATR-IR spectroscopic investigations were performed. Therefore, different AmpB-Eu L ratios, physical mixtures and the pure educts were analyzed. The carboxylic group of Eu-L is able to bind with positive charged functions like the amino function of AmpB at neutral pH during complex formation. Eu-L is well known for complex formation with positive charged drugs and polymers like Naltrexone, Carteolol, Eudragit E or Chitosan [145–148].

The recorded ATR-IR-spectra of the described samples and the corresponding wavenumbers are displayed in Figure 34. Remarkable differences between the drug-polymer complex, the physical mixture and the pure educts were found. AmpB showed at  $3369\text{ cm}^{-1}$  stretching vibrations  $\nu$ (-OH) and  $\nu$ (N-H). Eu-L showed bands at  $1722\text{-}1705\text{ cm}^{-1}$  which are characteristic for  $\nu_{\text{as}}$ (C=O) in ester and in carboxylic groups, these bands are highlighted by the red box (Figure 34).



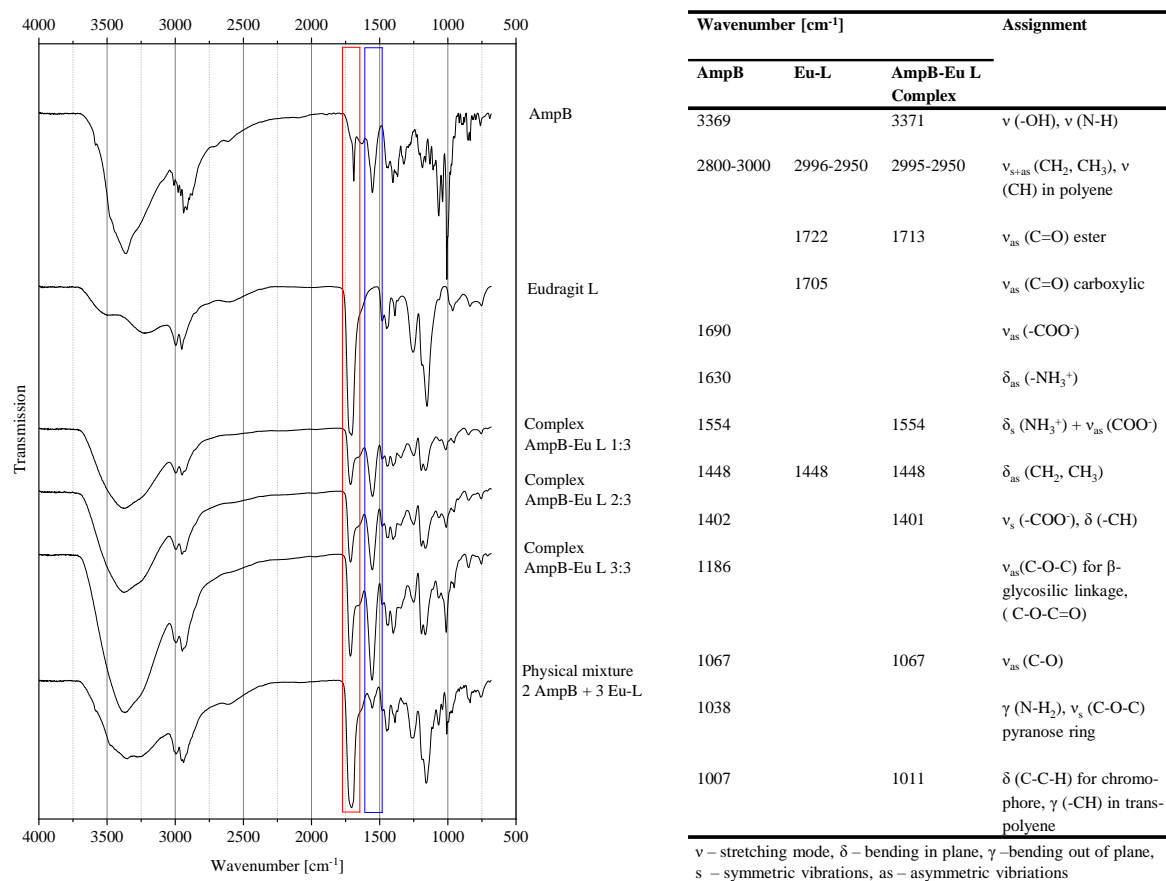


**Figure 34.** ATR-IR spectra of pure AmpB, Eu-L, AmpB-Eu L physical mixture (2+3) and the prepared polyelectrolyte complex at different initial used drug-polymer ratios. The detailed wavenumbers are listed in the table on the right ( $n = 1$ ) [138,149,150].

After complex preparation the spectrum showed a reduced transmission of this band and an increase of the band at  $1554\text{ cm}^{-1}$ . The band at  $1554\text{ cm}^{-1}$  is based on bending in plane  $\delta_s$  (NH<sub>3</sub><sup>+</sup>) as well as stretching vibration  $\nu_{as}$  (COO<sup>-</sup>). These characteristic vibrations are highlighted in blue. The similar band, in comparison to the different complexes with rising drug-polymer ratios 1:3, 2:3 and 3:3, which were initially used, characterizes the ATR-IR spectrum of AmpB. This band increased more than the band of pure AmpB. It has been described in previous researches also that this band results from the ionic interaction between -NH<sub>3</sub><sup>+</sup> of chitosan and -COO<sup>-</sup> of Eu-L during investigation of a polyelectrolyte complex [147]. The chemical structure of chitosan as well as AmpB is characterized by a secondary amino function and allows equal reactions with Eu-L. AmpB enables formation of ionic interactions with other AmpB molecules by itself, based on its amphoteric nature, which results in the band at  $1554\text{ cm}^{-1}$ . But the band at  $1554\text{ cm}^{-1}$  is much higher after complex formation what underlines that the amount of -NH<sub>3</sub><sup>+</sup> and -COO<sup>-</sup> interaction increased with polymer binding. Furthermore, it is important to discuss the results captured

form the physical mixture. The mixture showed a band at  $1540\text{ cm}^{-1}$ , which had a lower transmission compared to all drug-polymer ratios of the complex, what underlines the complex formation via non-covalent linkage between AmpB and Eu-L. The fact that AmpB is able to form dimers or aggregates by its amphiphilic and amphoteric structure, illustrates why dialyses as a purification step is necessary. The pore size of the membrane was 100 kDa and prevent AmpB-Eu L complex diffusing out of the system, whereas dimers and aggregates have been removed over time.

#### 4.2.2.3 Drug content and zeta potential

The formation of the polyelectrolyte complex consisting of AmpB and Eu-L was prepared to reach sufficient drug load of the electrospun fibers. Therefore, the polyelectrolyte complex had to be investigated in more detail. In Table 8 the results from the drug load, entrapment efficacy and zeta potential measurements are displayed.

**Table 8.** Drug load, entrapment efficacy and zeta potential of Amphotericin B-Eudragit L polyelectrolyte complex ( $n = 3$ , mean  $\pm$  SD).

AmpB-Eu L Ratio <sup>a</sup>	Drug load [%] <sup>b</sup>	Entrapment Efficacy [%] <sup>b</sup>	$\zeta$ -Potential [mV]	
			STF (pH 7.4)	PBS (pH 7.4)
1:3	$3.83 \pm 0.16$	$15.34 \pm 0.67$	$-32.9 \pm 2.55$	$-31.05 \pm 0.21$
2:3	$11.02 \pm 0.36$	$27.54 \pm 0.89$	$-32.3 \pm 0.36$	$-32.1 \pm 2.26$
3:3	$28.91 \pm 0.70$	$57.83 \pm 1.40$	$-39.4 \pm 1.64$	$-39.97 \pm 2.96$

<sup>a</sup> initial used AmpB-Eu L ratio

<sup>b</sup> m/m

Rising amounts of initial used AmpB increased the drug load of the complex from 3.83 % to 28.91 % of the highest drug-polymer ratio. The entrapment efficacy increased as well from 15.34 % of the 1:3 ratio, to 27.54 % of the 2:3 ratio and to 57.83 % of the 3:3 ratio. A higher amount of initially used AmpB increased the drug load as well. The amphoteric structure of AmpB allows formation of dimers and oligomers based on ionic interactions with other AmpB molecules. Unbound monomers ( $M_w$  924.1 g/mol) or oligomers were removed by dialysis purification, because all ingredients with a molecular weight  $< 100$  kDa are able to pass the dialysis membrane. The main fraction of the drug molecules bond to Eu-L ( $M_w$  125000 g/mol) were not able to pass the membrane [151]. Dialysis was performed during complex preparation over 24 h to remove the residual content of DMSO [152,153]. In addition, the zeta potential is listed in Table 8. All measurements showed that the complex

is loaded negative in PBS as well in STF ranging from -31.05 to -39.97 mV. Both buffers were investigated to gain information about the ionic influence onto the complex charge, but no difference was observed. At pH 7.4 the carboxylic functions of the complex are charged negative and induce negative zeta potential of the complex as well [138].

#### 4.2.2.4 X-ray powder diffraction

The crystalline and amorphous state of drugs entrapped into drug delivery systems affect the release, storage stability, solubility and physicochemical properties of the systems [154,155]. X-ray powder diffraction was performed to gain information about the physicochemical structure of AmpB inside the polyelectrolyte complex. Diffraction patterns of the starting material were investigated as references. Diffraction patterns were only observed when x-ray radiation interacts with the crystal lattice of the sample and if the diffraction conditions by Bragg's law were confirmed. The results in Figure 35 show that AmpB as educt was characterized by crystalline properties in solid state [156].

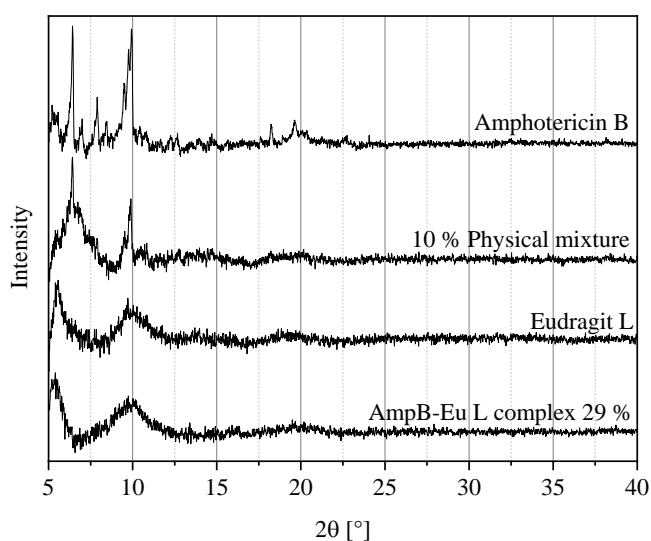


**Figure 35.** X-ray powder diffraction of pure Amphotericin B, 10 % physical mixture, Eudragit L and Amphotericin B-Eudragit L polyelectrolyte complex (29 %) ( $n = 1$ ) [138].

On the other side, Eu-L showed no diffraction patterns, what underlines the absence of crystalline domains inside the sample. The polymer chains are arranged in amorphous state caused by the chemical structure [157]. In the diffraction diagram broad signals are visible between 5-12.5°, these phenomena are too broad to be reflexes. In contrast to the polymer the physical mixture showed corresponding to AmpB main reflexes at 6° and 10°. These results show that the crystalline amount of AmpB can be determined in Eu-L blended mixtures with AmpB concentrations  $\geq 10\%$ . In contrast to the physical mixture, the

AmpB-Eu L polyelectrolyte complex showed no diffraction patterns, which illustrates that AmpB was transformed into amorphous state. Techniques like lyophilisation, used during complex preparation can also be applied for amorphous encapsulation of drugs into polymer matrices [158]. However, the determined shift of the UV/Vis absorption spectrum of the complex as well as the pure AmpB in section 4.2.2.1 exclude that the drug was embedded amorphous in the Eu-L matrix. Before complex formation, AmpB is able to form crystal lattices caused by its amphiphilic nature. After binding to Eu-L the distance of the AmpB molecules increased and the formation of crystal lattices is prevented.

#### 4.2.2.5 Differential scanning calorimetry

In the following chapter the thermal behavior of the complex and the educts were investigated. Therefore, the DSC profiles during two heating cycles were recorded. These are shown in Figure 36.

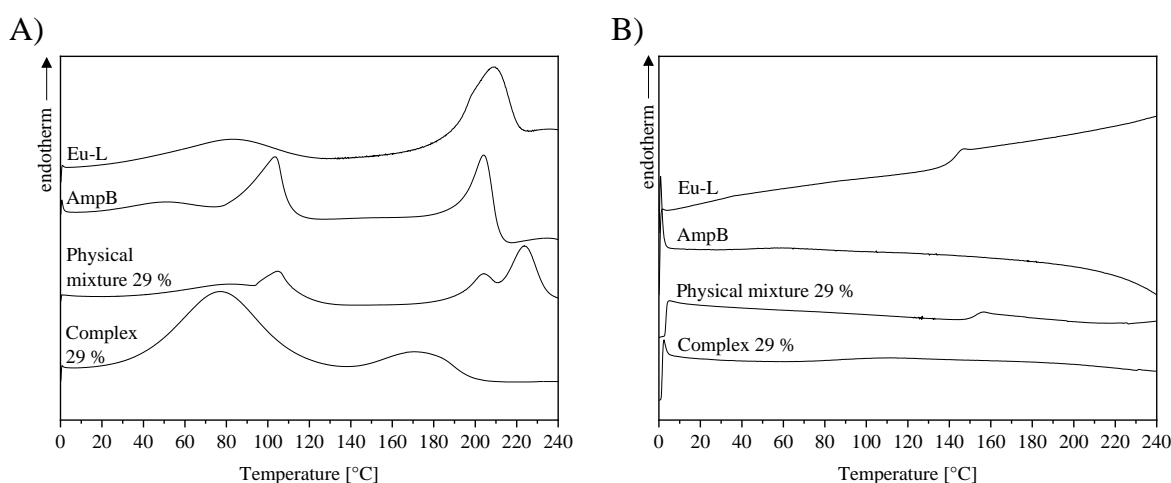


**Figure 36.** Differential Scanning Calorimetry of pure Amphotericin B (AmpB), Eudragit L (Eu-L), polyelectrolyte complex (Complex 29 %) and a physical mixture: A) First heating curve; B) Second heating curve [138].

During the first heat (A) pure Eu-L showed two endotherm peaks at 83 °C and 208 °C. The broad endothermic phenomenon at 83 °C is induced by evaporation of adsorbed water to the Eu-L powder surface. The second endotherm event at 208 °C started at 180 °C and ended at 220 °C. In the present case this thermal event results from endothermic relaxation of the polymer, caused by storage temperatures below the glass transition temperature. According to the fact that after the first heating cycle the observed peak disappeared, the described hypothesis of polymer relaxation is confirmed. After reheating in Figure 36 B), the previous bond water of the Eu-L sample was removed and the endotherm peak at 83 °C disappeared.

Furthermore, a glass transition of Eu-L at 143 °C was detected. In contrast to the polymer, AmpB showed during the first heating cycle two endotherm peaks, one at 103 °C and the other one at 204 °C, which correlate with the results described in literature [159,160]. The thermal event at 103 °C is based on a color transformation of AmpB from bright-yellow to brown orange [161]. It is well known that AmpB start degradation at temperatures over 200 °C without melting [156]. Therefore, it is assumable that the peak at 204 °C indicates the heat induced degradation of the AmpB. The process of degradation is based on the fact, that no thermal effect in the second heating curve was found (B). The DSC data of the physical mixture showed three different endotherm peaks at 103, 204 and 224 °C during the first heat (A). From the previous described results, the peaks at 103 °C and 204 °C are assigned to AmpB and the peak at 224 °C to Eu-L. After the first heating cycle the physical mixture showed a glass transition at 153 °C correlating with the DSC profile of Eu-L. Furthermore, the disappearance of the AmpB peaks were observed (Figure 36 B). The thermic behavior of the complex is different from the DSC profiles recorded from the unprocessed samples. In contrast to pure AmpB and Eu-L, the polyelectrolyte complex showed two broad endotherm peaks, one at 77 °C and the other one at 174 °C. Both peaks are different to the endotherm phenomena of the pure educts. Materials prepared by lyophilization, like the polyelectrolyte complex, are characterized by hygroscopic properties. Hence, moisture from room humidity adsorb to the complex surface. During the DSC measurements the thermal event at 77 °C is caused by evaporation of adsorbed water. The second thermal peak at 174 °C was not characterized by any baseline shift which correlates not with a glass transition. During the second heat, the previous described thermal events were not detected anymore. As the thermal event of the complex was missing during the second heating cycle, decomposition had to be assumed.

For more detailed discussion of decomposition and chemical reaction NMR experiments in combination with mass spectrometry were necessary. But the determined DSC experiments support the x-ray data and provide information about thermal stability and storage conditions of the samples. The developed complex should be stored at temperatures < 20 °C, which were necessary to prevent thermal reaction. Therefore, all samples were stored between 2-8 °C under light protection to prevent thermal reaction.

#### 4.2.2.6 Heat induced stress test

Information about the polyelectrolyte complex stability and resistance against the electrospinning process are necessary to avoid complex decay during nanofiber preparation. To gain an insight into the stability behavior of the polyelectrolyte complex the spectral changes of the UV/Vis spectra after heat treatment were recorded. In addition to the non-processed complex, the complex spectrum after encapsulation into electrospun fibers has been investigated. Therefore, the fibers were dissolved in double distilled water without heat treatment. In the following section the absorption spectra of aqueous complex solutions after incubation at room temperature, 40, 65 and 80 °C for 10 min were recorded. The recorded spectra are displayed in Figure 37.

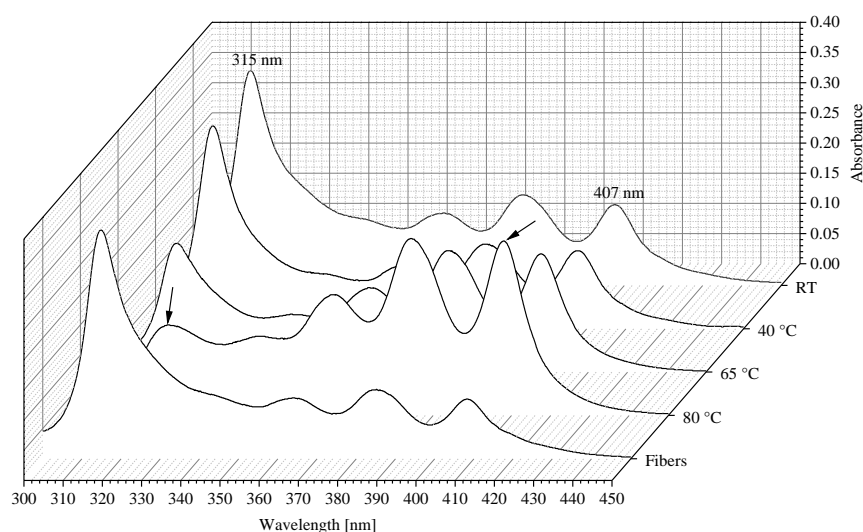


**Figure 37.** UV/Vis spectrum of AmpB-Eu L complex (29 %) dissolved in double distilled water after incubation at room temperature (RT), 40, 65 and 80 °C for 10 min and spectrum of the dissolved polyelectrolyte complex loaded fibers (Fibers) ( $n = 1$ ).

The complex spectrum incubated at room temperature is similar to the described results in section 4.2.2.1. The absorption maximum of the AmpB-Eu L complex was shifted to 315 nm compared to the monomeric AmpB spectrum, which is characterized by the absorption maximum at 407 nm. In progression of the heat induced stress test, it is obvious that the initial complex spectrum underlies spectral changes dependent from the applied heat. The complex absorption maximum at 315 nm decreased and the maximum at 407 nm increased. These results are more remarkable after incubation at 80 °C (Figure 37, black arrows).

The spectral shift illustrates that the AmpB-Eu L complex start converting into the monomeric form of the drug under heat influence. Reasons for structural changes are different. AmpB is, caused by its poor solubility, not able to dissolve in water. Bond to the

Eu-L backbone, the drug is able to dissolve sufficiently. It is well known that after increasing the temperature of the solvent the solubility of drugs increase as well [162]. Hence, the same behavior will be expected for AmpB. As consequence of the applied temperature, the polyelectrolyte complex starts partial dissociation and dissolves as monomeric AmpB in the surrounding media. After dissolving, the complex loaded fibers in water the spectra showed no differences between the unprocessed and the electrospun complex. The electrospun complex showed no increase of the monomer absorption maximum at 407 nm. These results underline sufficient stability of the polyelectrolyte complex against the electrospinning process and allow encapsulation of the AmpB complex into solid polymer fibers, without a decay into AmpB monomers.

#### **4.2.3 Morphology and drug load of the electrospun nanofibers**

In addition to the prolonged ocular residence time, is a homogenous, reproducible product morphology and a sufficient drug load a critical aspect for development of a suitable drug delivery system for treatment of keratomycosis. During the present thesis, different techniques to load electrospun nanofibers with the BCS IV molecule AmpB were described [163,164]. Therefore, blank Pullulan fibers containing 1 % Gellan Gum were loaded with AmpB-sodium cholate, AmpB-PLGA nanoparticles and AmpB-Eu L polyelectrolyte complex (29 %).

The captured ESEM images and the corresponding fiber diameter size distribution data are displayed in Figure 38. All ESEM images show fibers with smooth, homogenous appearance without beads or defects. A stable, continuous electrospinning process was achieved and high quality products were obtained. All samples showed fibers with diameters in the middle nanometer range. Figure 38 A) shows the data of the blank Pullulan fibers containing 1 % Gellan Gum. The modus of the fiber size distribution is 375-400 nm [73]. B) Illustrates the size distribution of the AmpB sodium cholate loaded fibers with a modus of 475-500 nm. C) Shows the results of the investigated AmpB-PLGA nanoparticle loaded fibers. The modus of these fibers increased to 525-550 nm. Figure 38 D) displays an ESEM image loaded with AmpB-Eu L complex (29 %) and the corresponding modus of 375-400 nm.

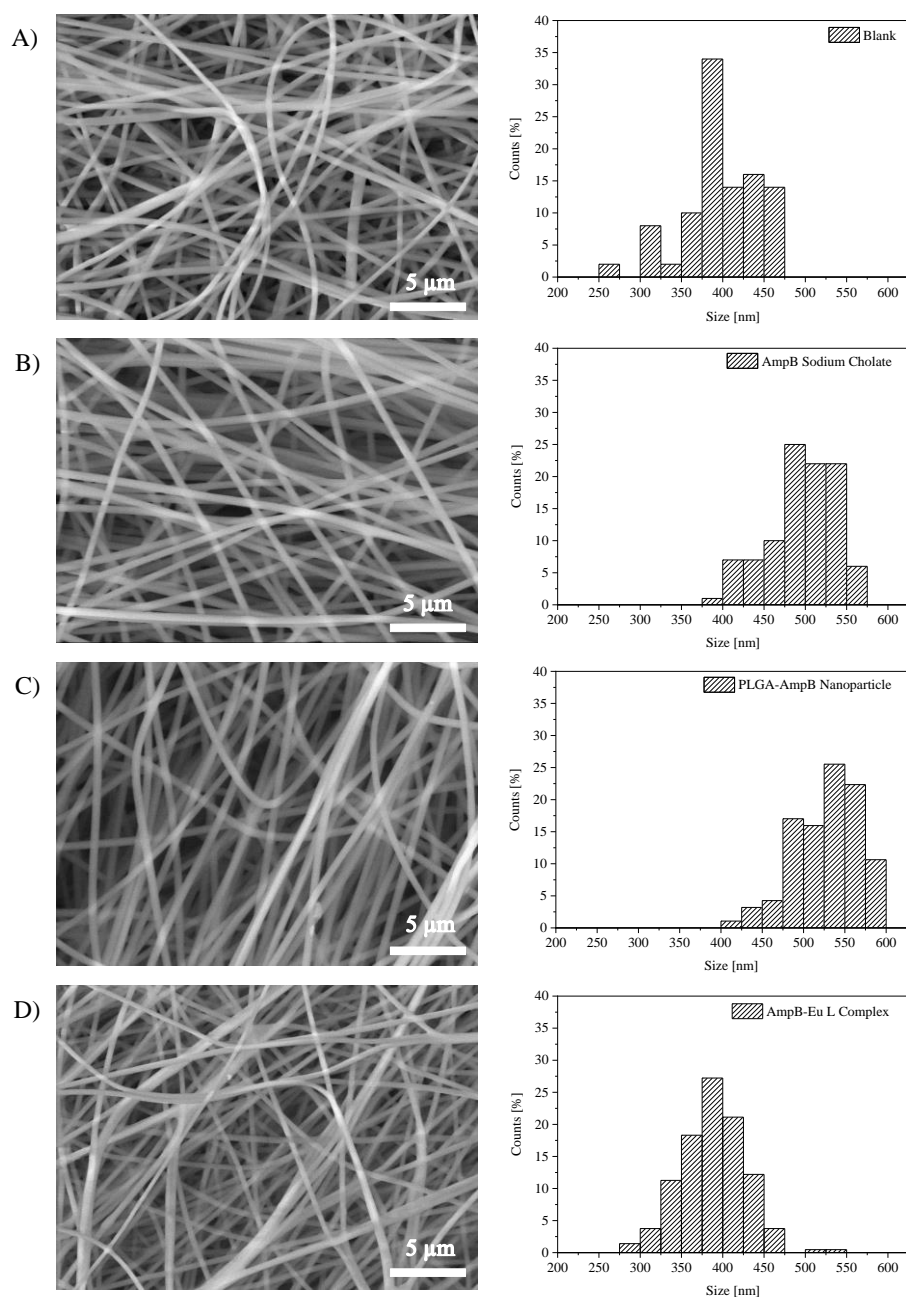


**Figure 38.** ESEM images and corresponding fiber diameter size distribution loaded with different AmpB formulations: A) Blank fibers; B) AmpB-sodium cholate; C) AmpB-PLGA nanoparticle); D) AmpB-Eu L complex (29 %).

To facilitate the comparison of the fiber size, the boxplot of the determined distribution is plotted in Figure 39. The whiskers show the minimum and maximum value of the distribution to gain information about the distribution width. The dependence of the processed AmpB formulation on fiber diameter attracts attention. After addition of AmpB and sodium cholate to the Pullan-Gellan Gum formulation the observed increase of the fiber size can be explained by sodium cholate as an ionic excipient. On one hand, affect sodium cholate, caused by the added cations the ion sensitive Gellan Gum in the spinning solution



and increases by sodium addition the solution viscosity. Hence, the higher viscous spinning solution induce the rise of the of the fiber diameter [75]. On the other hand, increase the addition of sodium cholate the conductivity of the spinning solution, what effects the spinnability as well [92].

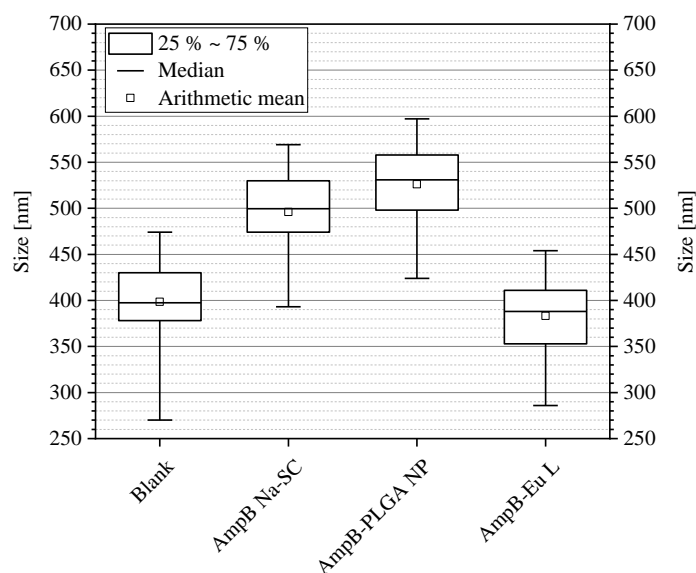


**Figure 39.** Boxplot of the different AmpB nanofiber formulations: Blank fibers; AmpB-sodium cholate (Na-SC); AmpB-PLGA nanoparticle (NP); AmpB-Eu L complex (29%). Whiskers show minimum and maximum.

The nanoparticle loaded fibers show in comparison to the blank formulation a higher fiber diameter. This can be explained by PVA, which was used during the nanoparticle preparation. PVA was added as stabilizing agent to the aqueous phase to prevent nanoparticle agglomeration. The excess of PVA was removed from the nanoparticle dispersion by centrifugal purification (section 3.2.1). But residual PVA localized at the nanoparticle surface is characterized by the polar hydroxyl groups and the non-polar carbon chains. The hydroxyl groups are aligned to the water phase and are able to form hydrogen bonds to the spinning polymers. Therefore, the interactions between Pullulan, Gellan Gum and PVA increased. In addition to the molecular interactions the higher amount of polymer (Pullulan, PLGA, PVA) inside the spinning solution contribute to the rise of the fiber diameter. The neutral zeta potential of the AmpB loaded nanoparticles does not affect the spinning solutions conductivity.

AmpB-Eu L complex loaded Pullulan-Gellan Gum fibers showed no difference in size compared to the blank fibers. The addition of the polyelectrolyte complex leads to the rise

of the amount of polymer in the spinning solution, but this influence becomes neglected by an increased solution conductivity after addition of the negative charged polyelectrolyte complex.

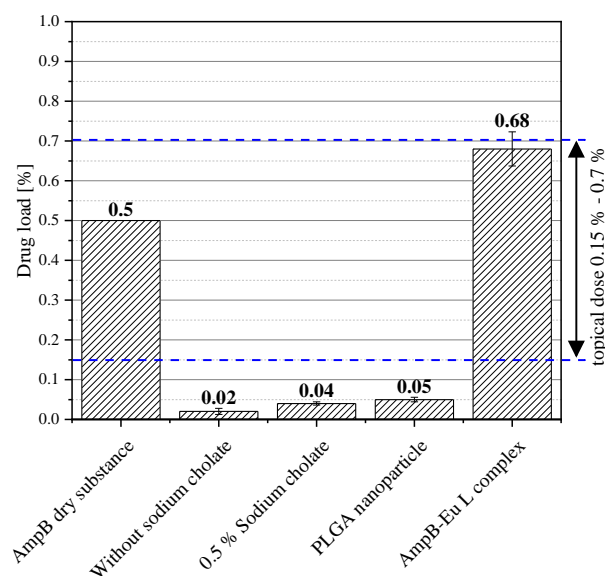


**Figure 40.** Drug load % m/m of different Pullulan-Gellan Gum fiber formulations. Amphotericin B doses used in clinical practices are given as topical dose borders (mean  $\pm$  SD,  $n = 3$ ) [165–167].

The drug load of the prepared nanofibers is essential for the sufficient treatment of fungal keratitis. Therefore, the determined drug load of different AmpB containing formulations is displayed in Figure 40. Within the conventional keratomycosis therapy, the patients are often treated with aqueous AmpB eye drops or ointments. Therefore, off-label used systems with 0.5 % AmpB were used (AmpB dry substance). The applied concentrations used in clinical practice range from 0.15-0.7 % AmpB and are often used in combination with triazole antimycotics like Voriconazole as subconjunctival injection for antifungal therapy [165,166,168]. The fibers loaded with AmpB, without any solubilization agent, result in a drug content of 0.02 %. After addition of sodium cholate to the AmpB solution the content increased to 0.04 %. Encapsulation of AmpB into PLGA nanoparticles, followed by electrospinning reached an AmpB concentration of 0.05 % AmpB. A higher load of AmpB into the polymer fibers was expected by adding sodium cholate and also by encapsulation of AmpB into nanoparticles. Each described formulation showed a slight increase of the fiber drug load, but the drug concentration is 10-25-fold lower compared to the eye drop doses used in clinical practice. From Figure 40 it becomes clear, that the addition of AmpB-Eu L polyelectrolyte complex to the formulation enables the rise of the AmpB drug load to 0.68 %, which is equivalent to the common dose utilized in clinical practice. A reduced AmpB drug

load by preparation of complex loaded fibers can be achieved easily by decreasing the initial added amount of complex, because as described above the AmpB load of the fibers is limited by the water solubility of the drug in aqueous media [69]. Caused by the amphiphilic nature and the low water solubility further ingredients like bile salts or phospholipids are necessary to increase the concentration in aqueous solution. Bile salts as solubilizing agent for AmpB are characterized by high cytotoxic potential. Therefore, the bile salt concentration in ocular drug delivery systems has to be limited [169–171]. Nevertheless, bile salts are used in the market formulation to ensure sufficient solubility of AmpB. As consequence of the cytotoxic effect, further increase of the sodium cholate content > 0.5 % m/m inside the fiber material was prevented to avoid cellular damages of the cornea surface.

### 4.3 Plate diffusion assay

The sufficient antimycotic concentration of AmpB has to be determined to ensure efficient treatment of keratomycosis. Different fungal strains were found as potential pathogens causing keratomycosis, especially fungi species belonging to *Candida*, *Aspergillus* and *Fursarium* [39,167]. To gain information about the relevant AmpB fiber doses, which are necessary to inhibit fungal growing, plate diffusion assays were performed. Therefore, *Issatchenkia orientalis* as risk group 1 fungus (according to German TRBA 460 Einstufung von Pilzen in Risikogruppen Julie/2016) belonging to the species of *Candida* were used during the performed experiments. A modified plate diffusion assay was used to gain information about the antimycotic effect by semi quantification of the inhibition zone.

In Figure 41 images of the plate diffusion experiments are displayed. Based on the low solubility of AmpB in aqueous media, the drug was dissolved in a mixture of 2 % v/v DMSO in methanol. To determine the potential inhibition of the solvent, the pure solvent mixture was investigated as well. Figure 41 shows that the inhibitory zone of the AmpB solution was larger than the zone of the pure solvent. In addition to the liquid solutions, different electrospun fibers were investigated. Blank Pullulan-Gellan Gum fibers containing 0.5 % w/w sodium cholate without AmpB showed a negligible inhibition zone compared to the fluid samples. Different reasons have to be discussed for this observation. It is well-known that bile salts like cholic acid have an antimycotic effect onto *Candida* species [172]. Correlating with the data described in literature, the slight inhibition of the blank lenses resulted from the sodium cholate content inside the fiber matrix. On the other hand, it has to be discussed that the electrospun lenses were applied in dry state to the previous

inoculated plates, whereas the fibers underlie volume contraction, caused by the hydration process. As consequence of the hydration, a spherical region without fungal suspension was obtained around the shrank lens. The fibers loaded with AmpB, containing 0.5 % (w/w) sodium cholate in the fiber matrix showed an inhomogeneous zone with a reduced fungal growth. The inhibition zone indicates a non-sufficient AmpB concentration to treat *Issatchenka orientalis* efficiently. In contrast to this formulation, the complex loaded fibers showed a homogenous zone of inhibition and a clear reduction of fungal growth, which illustrates a sufficient antimycotic effect of the polyelectrolyte complex encapsulated into the fibers.

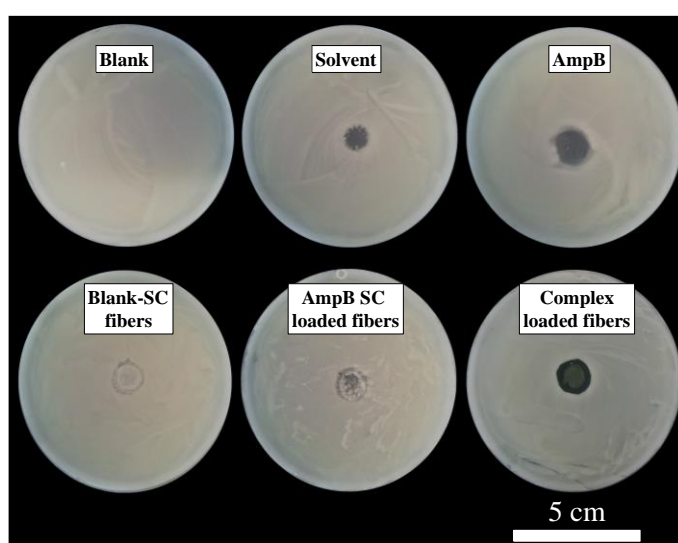


**Figure 41.** Plate diffusion test with *Issatchenka orientalis*: Blank; Solvent (2 % DMSO-methanol), AmpB (2 % DMSO-methanol), Blank SC fibers (0.5 % w/w sodium cholate), AmpB-SC fibers (AmpB loaded sodium cholate); Complex loaded fibers (0.68 % AmpB-Eu L polyelectrolyte complex loaded fibers) ( $n = 2$ ).

Residual components of the hydrated lens can be seen in center of the inhibition zone of the complex loaded fibers. More detailed quantification by measuring the area of inhibition via plate diffusion were neglected for the described experiments. The hydrogel, which is formed after lens hydration may reduce the diffusion inside the matrix, also caused by the increased viscosity and the hydrogel network (see NMR chapter 4.1.5). Small neutral drugs are slightly affected by the mesh size of hydrogels. But with increase of the drug size the diffusion is more affected [173,174]. For complex formation, the size of AmpB ( $M_w$  924 g/mol) increases after binding to the Eu-L backbone ( $M_w$  125000 g/mol) [63,151]. Instead, the liquid formulations were able to diffuse freely inside the agar media and showed a more spreading inhibition zone. As consequence larger inhibition zones for liquid formulations were obtained, caused by the different diffusion velocities inside the agar media. The

described experiments were performed to gain information about the potential antimycotic activity of the drug loaded electrospun lenses, but therefore it is necessary to investigate the solid samples. These experiments allow the conclusion that the AmpB concentration of the sodium cholate loaded fibers was not able to overcome fungal growth. In contrast, the developed polyelectrolyte complex showed a sufficient antimycotic activity against *Issatchenkia orientalis* and its potential ability to treat keratomycosis. Caused by the low drug load of the bile salt containing AmpB fibers these were rejected for further investigations. As consequence, all following experiments were performed with the complex loaded fibers.

#### 4.4 Impact of e<sup>-</sup>-beam treatment

Drug delivery systems for ocular use like eye drops, ointments or inserts have to ensure, next to suitable particle size the absence of pathogen microorganisms. Therefore, the Ph. Eur. describes different suitable sterilization methods to reduce the sterility assurance level (SAL) to  $\leq 10^{-6}$  of ophthalmic dosage forms. The SAL describes the probability that drug units contain infectious microorganisms. Sterilization by dry or wet heat are the often used methods to guarantee sterile conditions of drug delivery systems. Both techniques are based on temperature treatment of the samples. Wet heat at 121 °C for 15 min is used during autoclaving [175]. In contrast to autoclaving, the dry heat sterilization has to be performed for 2 h at 160 °C [175]. Caused by the physicochemical properties of Gellan Gum and Pullulan, the fibers cannot be the sterilized by dry or wet heat. The high temperature exceeds the glass transition temperature ( $T_g$ ) of Pullulan and Gellan Gum. Pullulan for example shows depended form the residual moisture content inside the polymer a shift of the determined glass transition from 38 °C to 59 °C [176]. In preliminary experiments a  $T_g$  of Pullulan was determined to 66.6 °C (3 K/min, -20-130 °C, two heating cycles) by DSC. Hence, the terminal sterilization of the fibers by heat cannot be performed, because softening of the Pullulan above the  $T_g$  takes place. As consequence of the fiber softening, the mesh structure started merging until a plain polymer film was obtained. Softening and merging of the fibers affected the porosity and surface area negatively. Porosity and surface are key factors for the fast hydration process *in vivo*. Additionally to the heat based sterilization techniques, the pharmacopeia lists gamma or electron beam irradiation with doses of 25 kGy to ensure terminal treatment of drug delivery systems [175]. The process is performed at room temperature and seems to be suitable for sterilization of the electrospun fibers.

Alternatively to the described method gas sterilization with ethylene oxide for examples is another potential sterilization technique when all other processes cannot be used, caused by sample degradation [175]. Gas sterilization is suitable for the reduction of microorganisms at the sample surface and does not allow diffusion inside the system. Because of this, gas sterilization is inappropriate for the electrospun fibers. In the following section the impact of electron beam sterilization onto the molecular weight of raw Pullulan and Gellan Gum will be discussed. Figure 42 A) displays the molecular weight  $M_w$  before and after sterilization including the obtained polydispersity index.

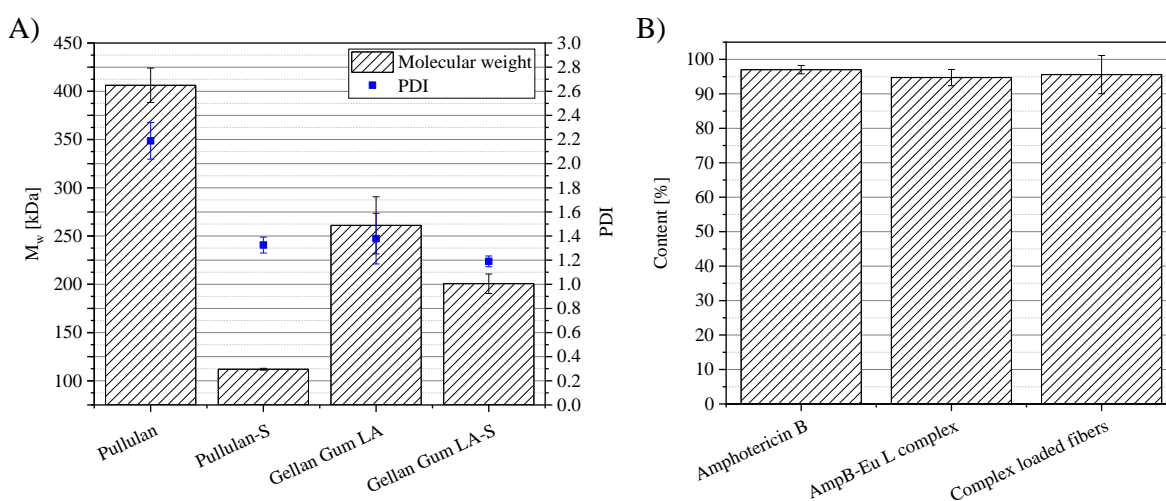


**Figure 42.** Impact of electron beam sterilization onto molecular weight and drug load: A) Molecular weight ( $M_w$ ) and polydispersity index (PDI) of Pullulan and Gellan Gum before and after sterilization (S); B) AmpB content in % m/m of pure AmpB educt and AmpB-Eu L complex and complex loaded after electron beam sterilization (mean  $\pm$  SD,  $n = 3$ ).

Pullulan showed before sterilization a molecular weight of 406 kDa, after irradiation the molecular weight decreased to 112 kDa. The initial molecular weight of Pullulan decreased about 72 %. The PDI of the polymer decreased from 2.19 to 1.33 as well. Instead, Gellan Gum showed an initial molecular weight of 261 kDa and after sterilization 200 kDa was obtained, what correlates with a reduction about 23 %. The PDI showed a slight decrease from 1.38 to 1.19. It is obvious that the electron beam treatment degrades the molecular structure of both polymers, but Pullulan is more affected than Gellan Gum. Because of the high energy impact onto the polymers, chain scissions by radiolysis took place. The degradation of Pullulan for the use *in vivo* can be neglected, because its function as spinning co-polymer does not affect the gelling mechanism strongly. The molecular weight of Gellan Gum as main gelling agent was slightly affected. The major chemical reactions under electron beam treatment are cross-linking and chain scission depending on the applied dose

and environmental conditions. Hence, an increase as well as a decrease of the molecular weight could be expected. In the literature it is described that Pullulan start chemical reactions like formation of carboxyl, oxyketo and carbonyl functions inside the polysaccharide molecules. These were described after  $\gamma$ -irradiation of an aqueous Pullulan solution [177]. Furthermore, it is well known that polymers underlie intense chain scission dependent from the applied irradiation dose and break into shorter fragments [178]. All investigated samples were treated under oxygen atmosphere, room temperature and in solid state. To reduce the extent of chemical reactions the samples can be irradiated under argon atmosphere or vacuum to prevent oxidation [179]. Furthermore, the samples can be cooled for example in liquid nitrogen to decrease the molecular mobility which may prevent molecular scission and reaction, dependent from the drug delivery formulation [180].

Beside the molecular weight, the drug content of the different AmpB formulations after  $e^-$ -beam treatment was investigated. The determined drug load is displayed in Figure 42 B). Therefore, pure AmpB, AmpB-Eu L complex (29 %) and the complex loaded fibers (0.68 %) were investigated before and after sterilization. The AmpB content of the pure drug decreased to 96 % of the initial value after sterilization. The AmpB content of the polyelectrolyte complex decreased after electron beam treatment to 95 % and the electrospun complex to 95.5 %. These data underline the resistance of AmpB as well as the polyelectrolyte complex against electron beam induced radiolysis and as consequence the ability to treat keratomycosis efficiently after sterilization [181].

#### **4.5 Cytotoxicity *in vitro*: hTCEpi differentiation-assay**

Dependent from ocular use, it is necessary to perform cytotoxicity experiments with differentiated cornea epithelium cells to simulate exact histological conditions of the human eye. *In vivo* the ocular surface is characterized by epithelial stem cells located in the limbus, the corneo-scleral junction and differentiate over time into corneal epithelial cells. Under influence of calcium the stem cells are able to differentiate *in vitro* into a multilayered epithelium similar the cornea structure *in vivo*. The used model allows an exact simulation of the physiologic conditions by an air lifted experimental setup correlating with exact *in vivo* conditions. In Figure 43, the results of the fiber toxicity experiments after treatment of stratified epithelium cells are displayed. The toxicity was determined in the basal and wing cell layer as well as over the whole cellular layers.

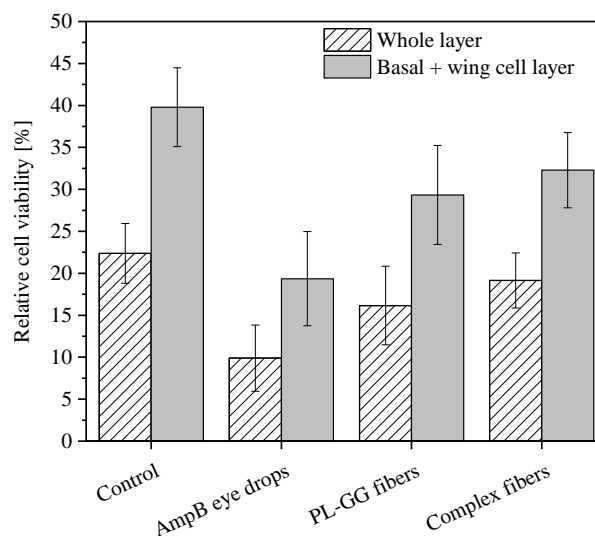


**Figure 43.** Cytotoxicity assays (KI-67) of a multilayered-stratified cornea model with hTCEpi cells: Untreated cells (control), AmpB eye drops, 1 % Gellan Gum-Pullulan fibers (PL-GG) and polyelectrolyte complex loaded fibers 0.68 % (complex) (median  $\pm$  SD,  $n = 4$ ).

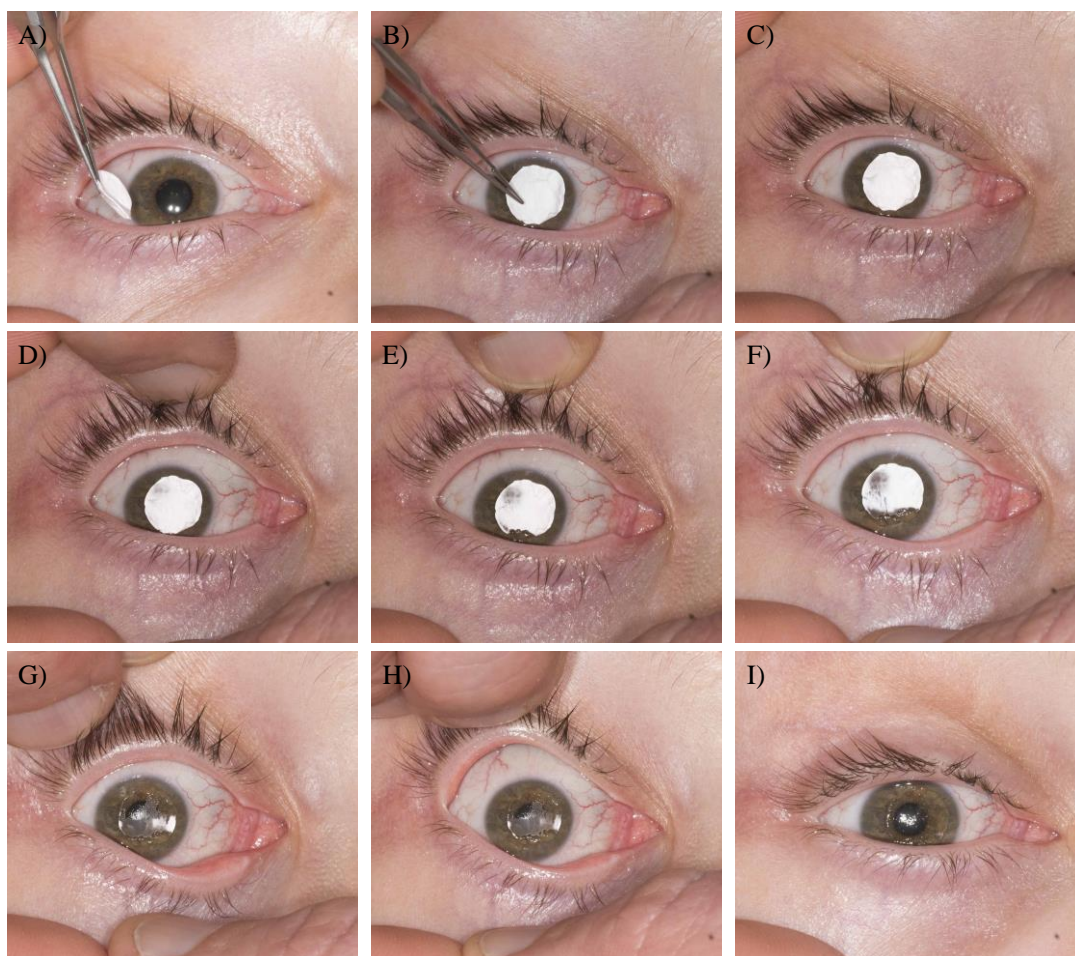
The control group showed that 40 % of proliferating cells in the basal and wing cell layer are KI-67 positive after incubation. The diluted AmpB eye drops, which were used in clinical practice, show a viability of 19 %. The blank as well as the complex loaded fibers showed no difference to each other in number of proliferating cells, but with a slightly decrease between 29 and 32 % in comparison to the control samples. These results illustrate, that the blank fibers as well as the complex loaded fibers showed a slight viability decrease of the cells compared to the untreated cells. But in contrast to the conventional used AmpB formulation, these are less cytotoxic. The commercially available AmpB formulation contains bile salts to ensure complete solubilization of AmpB. Bile salts are well known for their cytotoxic potential in addition to the toxicity of pure AmpB. After complex formation the mobility of the drug is reduced by binding to the polymer. Because of this, the cytotoxicity of similar AmpB formulations like liposomal or other polyelectrolyte systems show an increased cellular tolerance [182,183]. During the performed experiments the complex loaded nanofibers show superiority against the commercial formulation used in clinical practice.

Further cytotoxic experiments like the Resazurin-reduction assay of blank Pullulan-Gellan Gum nanofibers are described in Appendix 7.



#### 4.6 Ocular residence time *in vivo*

*In vivo* experiments are an essential element for the exact determination of the ocular residence time. In the following section the results of the human experimental design will be displayed and discussed in detail. In general *in vivo* experiments with animals like rabbits, rats or zebrafishes were performed previously to evaluate the therapeutic potential of the developed drug delivery system [184,185]. In the present case, experiments with animals were not performed, because the used ingredients Gellan Gum, Pullulan and water are well known as non-toxic components, which correlate with the determined data of the performed cytotoxicity experiments *in vitro*. Furthermore, the utilized dye fluorescein sodium is available as authorized medicinal product and is applied since a long time during clinical practice. The parenteral dye formulation Fluorescein Alcon® 10 % Injektionslösung contains the used dye in a higher dose compared to the described experiments and illustrates the safeness of instillation [186].



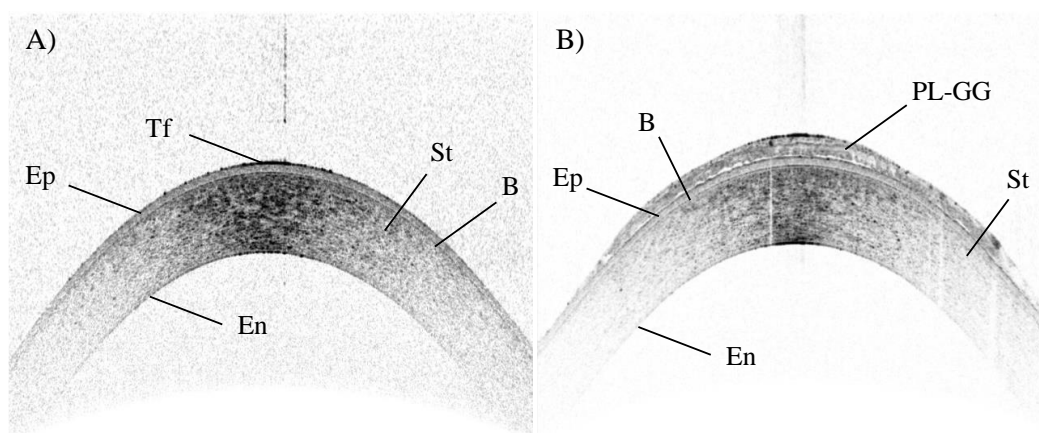
**Figure 44.** Application (A-B) and hydration process (C-I) of sterile Pullulan-Gellan Gum fibers loaded with 0.005 % fluorescein sodium. Photographs were captured during a period of 30 s.

Figure 44 illustrates the application (A-B) and hydration process (C-I) of the drug free electrospun lens exemplary for one volunteer (volunteer 2). Immediately after lens application, the fibers start hydration with tear fluid contact. The lens hydration began in the lower part of the eye (E) and started spreading to the upper part (F) until a transparent gel was formed at the ocular surface (I). The illustrated hydration process was finished after 30 s of application, what allows fast and high comfortable treatment of the patients. High porosity combined with high surface area of the prepared fibers enables fast water penetration into the mesh and accelerates the gel formation process [187].

#### 4.6.1 Optical coherence tomography

In the following section the results of the *in vivo* experiments in humans were described and discussed in detail. OCT as non-invasive *in vivo* imaging method, allowing a deep insight via cross-sectional imaging into biological systems. Before, exemplary OCT images will be commented to facilitate detailed comprehension.

Two different OCT images are displayed in Figure 45. A) Illustrates the blank eye and B) the eye after Pullulan-Gellan Gum lens application. The cross-section of the eye in Figure 45 allows visualization of the tear fluid (Tf) at the cornea surface and the tear fluid covered epithelium (Ep). The optical laser scattering enables the visualization of the bordering stroma (St) and endothelium (En) of the cornea. The stroma and epithelium are confined by the bowman membrane (B). After lens application in Figure 45 B) an additional layer appears in the OCT image. The tear fluid was replaced by the Pullulan-Gellan Gum gel. Immediately after lens instillation the tear fluid was absorbed and used for fiber gelation.



**Figure 45.** Optical coherence tomography image: A) Eye without lens, B) Eye with applied Pullulan-Gellan Gum lens (Ep-Epithelium, Tf-Tear fluid, St-Stroma, B-Bowman membrane, En-Endothelium, PL-GG-Pullulan-Gellan Gum gel).

The OCT images were captured in horizontal as well as in vertical orientation of the eye to gain information about the cross-sectional distribution of the electrospun lens. Figure 46 displays the captured OCT images in each orientation. The dashed line visualizes the located cross-section position of the eye during OCT imaging.

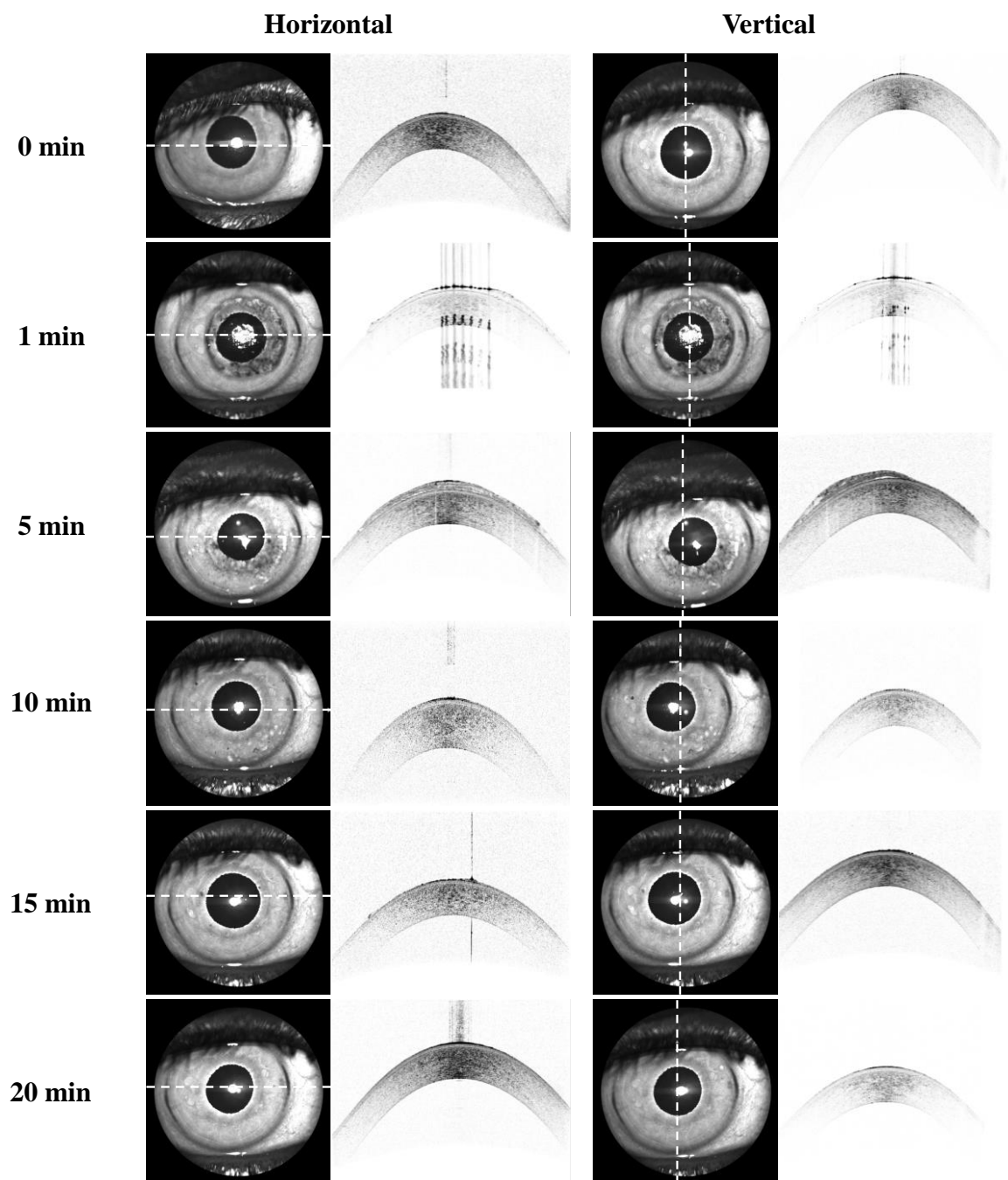


**Figure 46.** Optical coherence tomography images of volunteer 2 before and after instillation of sterile Pullulan-Gellan Gum lens loaded with 0.005 % fluorescein sodium over a period of 20 min. Horizontal and vertical imaging of the eye, the dotted line shows sectional plane.

The eyes were analyzed blank and after lens instillation over a period of 30 min. 1 min after lens instillation, an additional layer at the cornea was detected. The Pullulan-Gellan Gum lens gelled immediately after tear fluid contact. From the image captured after 1 min the homogenous gel distribution over the cornea surface in horizontal as well in vertical position was determined. The gel was detected already after 5 min. After 10 min of application, no residual amounts of gel were detected in the OCT images. Similar results were observed in horizontal and in vertical position of the eye during the investigated period. The absence of the gel after 10 min in OCT image does not indicate that the whole sample was removed from the cornea surface, because of the limitation by the OCT resolution. To avoid subjective evaluation of available gel amounts the incorporated dye fluorescein sodium has been quantified in BAF mode in the following section.

#### **4.6.2 Optical coherence tomography-fluorescence quantification**

To gain an objective evaluation about residual amounts of the drug delivery system and to investigate the potential superiority of the electrospun fibers against conventional eye drops fluorescein sodium was incorporated into the Pullulan-Gellan Gum lens (0.005 % m/m) and into isotone eye drops (0.001 % m/m). Therefore, OCT images in BAF mode were captured after eye drop and fiber instillation over 30 min. Afterwards the mean gray value of the captured images was analyzed to ensure residual sample quantification.

In Figure 47, the images of the eye drops and the fibers are displayed. The bright areas inside the images indicate the fluorescein sodium signal. At first, the results of the fiber application will be discussed. Before lens application, no signal at the ocular surface was detected (Blank). The bright spot located at the ocular center is caused by the reflection and autofluorescence of the pupil. This signal caused by the pupil was neglected for all measurements. 1 min after lens application, a homogenous distribution of the *in situ* formed gel at the cornea center was detected. The gel structure appears homogeneously with slight difference in thicknesses at the right, upper section. This slight difference in fluorescence intensity can be explained by the fiber preparation process similar to the previously performed experiments *in vitro* (section 4.1.8). The used electrospinning setup allows the preparation of randomly orientated fibers in plane. Hence, slight differences between the mesh thicknesses can be obtained. After 5 min of instillation, the lens signal can be still detected. It is obvious that the previous spherical gel shield was deformed and smaller gel structures were distributed over the cornea, driven by the lid blink shear forces. Furthermore,

new spots of fluorescence signal were detected in the fornix conjunctivalis superior and inferior. Caused by the lid shear, gravimetric forces and the rapid tear turnover fluorescein sodium containing amounts of gel were transported into the fornix. The dye concentration inside the fornix acts as depot for the distribution of fluorescein sodium. Hence, each blink forms a new layer of dye distributed over the cornea surface in addition to the attached gel shield.

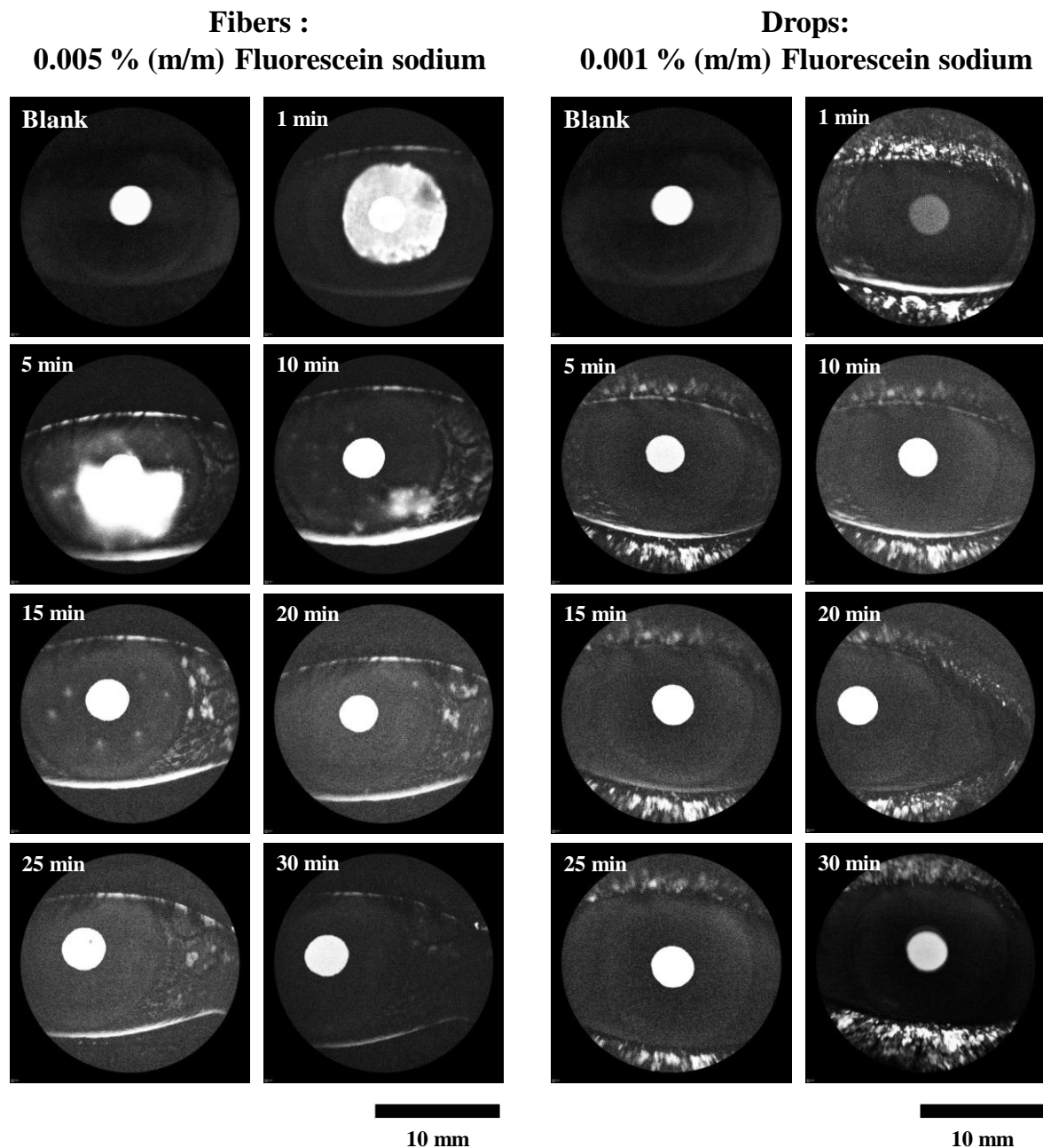


**Figure 47.** Optical coherence tomography (BAF) images of fluorescein sodium loaded fibers (0.005 %) and eye drops (0.001 %) over a period of 30 min (Volunteer 2).

10-15 min after application the major fraction of the gel is transported into the fornix. Nevertheless, gel spots can be still detected, which are distributed over the cornea. In the following interval, the gel signal in the center of the eye disappeared, but residual amounts of fluorescein sodium were detected in the fornix after 30 min. In contrast to the investigated fibers, the eye drops showed a different behavior after instillation. Immediately after drop application, the main fraction is located in the fornix and the whiskers. In contrast to the eye drops, the fibers did not show any dye deposition at the whiskers. The eye drop fraction located at the whiskers is not able to distribute over the eye surface. The fornix signal of the eye drops is weaker compared to the fiber signal. After 15 min only, traces of dye can be detected in the OCT image at the cornea.

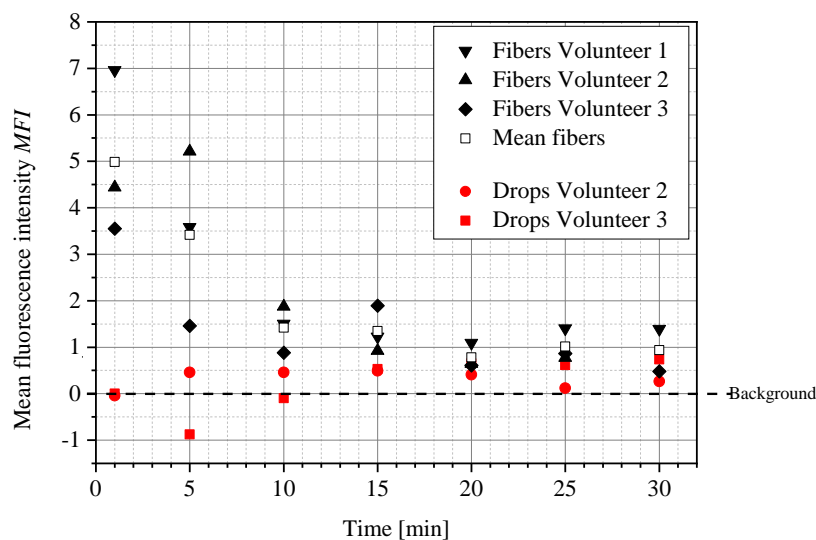


**Figure 48.** *Optical coherence tomography fluorescence quantification of fluorescein sodium loaded Pullulan-Gellan Gum fibers (0.005 %) and eye drops (0.001 %).*

A detailed quantification of the fluorescence signal via analyzes of the gray value is displayed in Figure 48. It shows that the applied fibers had a mean fluorescence intensity *MFI* of 5 immediately after application. This indicates that the measured signal is 5-fold higher than the background signal. After 5 min, the fluorescence signal was 3.5-fold higher. After 20 min, the fiber signal correlated with the background signal and no further differences were obtained. The eye drops showed instead that the signal did not exceed the background level during all measurements. The eye of volunteer 1 was excluded from the eye drop experiment, because a keratoconjunctivitis sicca syndrome (“dry eye”) was diagnosed before. For interpretation of the fluorescence quantification only the fluorescence signal localized at the cornea center was used. The signal in the fornix was neglected,

because the linear concentration-fluorescence correlation cannot be guaranteed. In the literature, similar methods were used to determine the ocular residence time of Gellan Gum *in vivo*. During one research for example, Cyanine 5 as fluorescent dye was added to the Gellan Gum formulation to ensure quantification of the residual drug delivery system. The samples were instilled into cul-de-sac of New-Zealand albino rabbits and the fluorescence image was captured with a Fluobeam<sup>®</sup>. During the described experiments, the ImageJ software was also used for quantification, what underlines the practicability of the performed method [188].

In addition to the determined experimental data, the volunteers were asked about their feelings and impressions during lens instillation to evaluate the acceptability of lens application. All volunteers described the lens as a comfortable feeling with moistening effect at the ocular surface similar to lubricant eye drops. Furthermore, the volunteers were asked about their sight quality. All volunteers described that a clear, non-blurred sight with no irritation effect was observed. Further, they specified that immediately after lens instillation where the lens was not hydrated a white, non-transparent layer covered the eye for a short time (Figure 44 C). But the non-transparent layer cleared rapidly after tear fluid contact to a gel without air-bubbles and homogenous distribution at the cornea surface. After 60 min of experiments, all volunteers described that the moistening feeling existed already even though no residual signal was detected during the OCT experiments. This underlines that a further prolongation of the ocular residence time was achieved in combination with high patient compliance of Gellan Gum-Pullulan fibers. All discussed results underline the superiority of the electrospun fibers against the conventional eye drop formulation. The fibers showed higher local concentration of the model dye at the cornea surface in combination with increased depot effect. The developed *in situ* gelling fibers are a promising system for increasing the ocular residence time *in vivo* and may expand the therapy opportunities to treat ocular diseases.

#### **4.6.3 Pentacam<sup>®</sup> imaging**

The Pentacam<sup>®</sup> as a Scheimpflug camera based system is a powerful, fast and non-invasive method to gain information about the corneal thickness and ocular curvature during clinical diagnosis [87,88,189]. In the present case, the method was used for thickness investigation of the *in situ* formed gel after lens application at the ocular surface. In Figure 49 the results



of the Pentacam® images are displayed. Therefore, the data of three volunteers are shown after 1, 15 and 30 min of lens application.

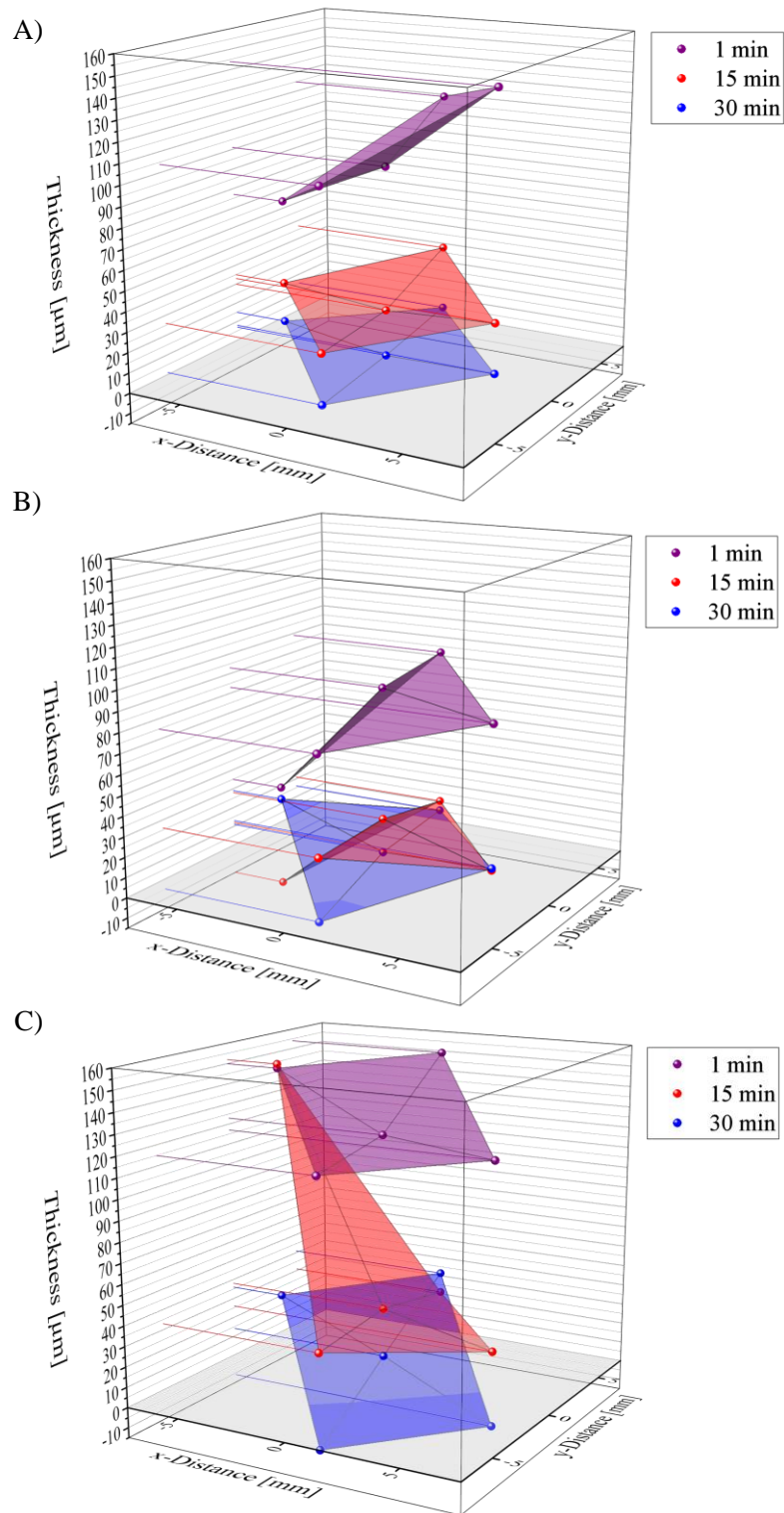


**Figure 49.** Pentacam® imaging of the ocular surface of volunteer 1 (A), 2 (B) and 3 (C). Measured gel thickness dependent from the cornea topography over time.



The thicknesses of five different points distributed over the cornea were investigated described in section 3.5.2. The detailed region localization and their corresponding xy-coordinates of Figure 17 and Figure 49 are listed in Table 9.

**Table 9.** *xy-coordinates of the Pentacam® measurement points distributed over the cornea surface.*

Localization of thickness measurement	x y-coordinates <sup>a</sup>
Cornea center	0 0
5 mm - above cornea center	-5 0
5 mm - below cornea center	5 0
5 mm - left to cornea center	0 -5
5 mm – right to cornea center	0 5

<sup>a</sup> Corresponding coordinates to Figure 17 and Figure 49

The graph shows that the gel thickness in the cornea center is between 90-125  $\mu\text{m}$  immediately after lens instillation. The data of volunteer 1 and 2 illustrate that the gel thickness 5 mm below the cornea center (5|0) is higher compared to the section in the upper part (-5|0) of the eye after 1 min. This can be explained by the shear forces caused by the lid blink. As consequence, the gel was sheared in direction of the fornix conjunctivae and the gel thickness in the upper part decreased. In conflict to this phenomenon, the data of volunteer 3 (Figure 49 C) do not fit to this hypothesis. In this case the gel thickness is inversed, so that the gel layer above the cornea center (-5|0) is thicker. Probably, the ocular anatomy affects the sample flow, caused by the spherical geometry of the eye ball. The spherical anatomy may induces flow to the left, right or upper sections when the lens is not applied exactly into the middle of the cornea center. After 15 min, the layer at the cornea center (0|0) was 30-35  $\mu\text{m}$ . 30 min after application, a layer thickness of 5-15  $\mu\text{m}$  was detected in the cornea center (0|0). These data illustrate that with time the gel thickness at the cornea decreased from the initial value, but a thin layer can be detected after 30 min.

#### 4.6.4 Nanofiber impact onto the physiological tear fluid pH

The pH is an important marker for physiological compatibility of ocular drug delivery systems. A strong pH shift may induce cytotoxic effects and may cause cornea damage. To maintain the physiological pH the ocular tear fluid is characterized by different electrolytes with limited buffering capacity. The main buffering effect is based on a bicarbonate systems [190]. Triggered by strong acidic or basic samples the buffer capacity can be exceeded and

the pH shifts to toxic values. Hence, the effect of ocular formulations onto the tear pH has to be screened during eye researches. A low tear volume of 10  $\mu\text{l}$  is a high challenging task for exact determination of the physiological pH. The most common methods like pH sensitive electrodes and titration need larger sample volumes and made exact pH determination difficult [190]. Other methods like fluorophotometric analysis need dyes like biscarboxyethyl-carboxyfluorescein, where further processing of the tear volume for quantification are necessary. This high effort makes these methods not attractive during the present research [191]. Hence, pH strips seems to be an effective way to evaluate quick and sensitive the influence of the applied lens onto the physiological pH.

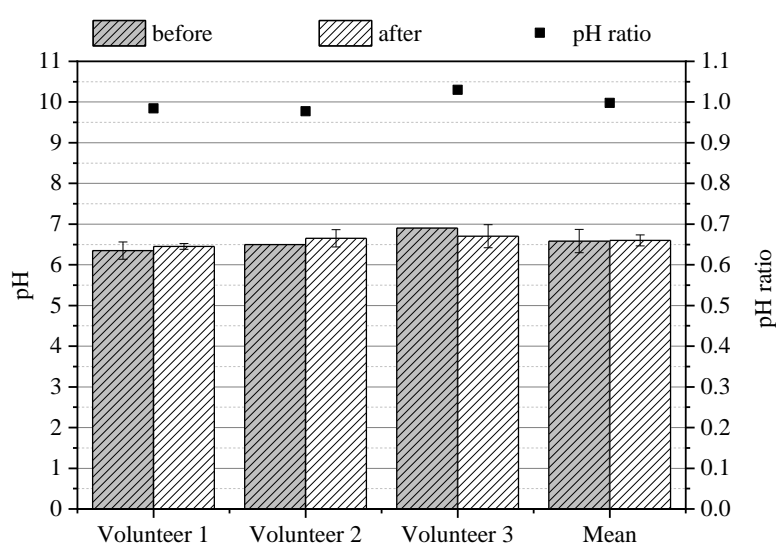


**Figure 50.** Influence of instilled Pullulan-Gellan Gum nanofibers onto the physiological pH before and after lens instillation ( $\text{pH ratio} = \text{pH}_{\text{before}}/\text{pH}_{\text{after}}$ ) (mean  $\pm$  SD,  $n = 2$ ).

The pH was determined before and after lens instillation. In Figure 50, the determined values are displayed. All volunteers showed a tear pH of 6.4–6.9 before instillation. After lens instillation, it was found that the pH was between 6.5–6.7. No difference was observed in the mean pH. In addition to the exact values, the pH ratio is plotted in Figure 50 as well. The mean pH ratio 0.997 illustrates that no effect of the applied lens was observed. In the literature, different pH of healthy humans were determined *in vivo* ranging from 7.1–7.6, therefore high sensitive fluorescence methods and microelectrodes were used [191–193]. The pH determination by pH strips is in contrast a more subjective evaluation of color changes. The methods described in the literature are more sensitive and allow more detailed determination of the tear pH. But the utilized pH stripes are a cheap, fast and sufficient to determine the relative changes of the physiological tear pH.

## 5 Summary and Perspectives

The therapeutic interest of new ocular drug delivery systems is steadily increasing to overcome the biopharmaceutical problems of conventional eye drops. Reduced ocular residence time and high dose frequency are the major challenges for these systems, caused by the fast lacrimal tear turn over. Especially the treatment of ocular infections like the fungal keratitis confronts the medical science with serious problems. Gellan Gum as an *in situ* gelling agent, which is already used in eye drop formulation, is a potential candidate to overcome these therapeutic challenges.

At the beginning of the research, the rheological behavior of the spinning solutions has been investigated to gain information about their viscosity and electrospinnability. It was found that pure Gellan Gum was characterized by an intense shear thinning effect, which prevents fiber formation. The anionic nature of the polymer is not able to form sufficient chain entanglements caused by the induced electrostatic repulsion. After addition of Pullulan, as a spinning co-polymer to the Gellan Gum solution, fiber formation took place. 15-20 % Pullulan showed a sufficient viscosity for electrospinning and enabled the incorporation of 0.225 % Gellan Gum into the fibers. A rise of the Gellan Gum amount in the spinning solution resulted in discontinuous electrospinning processes. The fiber diameter was investigated by ESEM and showed that the size was in the middle nanometer range. With an increase of the Pullulan concentration from 15 to 20 %, with constant Gellan Gum content the diameter of the fibers increased as well. The new Nano-CT method supported these results and showed the high fiber porosity and surface area. Electrospun fibers with approximately 1 % w/w Gellan Gum content as promising candidate were used for further experiments.

During oscillating rheological experiments, the electrospun fibers showed gel-like behavior of the Gellan Gum containing formulation with a loss angle  $\delta < 45^\circ$ , when fibers were hydrated with cation containing STF. This was not achieved with double distilled water. Pure Pullulan fibers moisturized with STF as well as with double distilled water showed properties of viscoelastic fluids. In addition to the oscillation rheology, NMR experiments were performed to determine the diffusion constant  $D$  and the  $T_2$  relaxation time of the fibers. These experiments underline the superiority of the Gellan Gum loaded fibers for use as *in situ* gelling system compared to pure Pullulan fibers.

A high adapted geometry of the drug delivery system to the eye anatomy had to be ensured to reach sufficient therapeutic effect. Therefore, the planar electrospun meshes were punched out to disks with 1.5 cm diameter with 4 mg weight. The disks were successfully formed with a self-constructed 3D printed matrix to achieve a curvature of 10.92 mm. The human curvature value was reported from 7.10-8.75 mm, what predicts high adaptation to the ocular surface.

A new experimental setup for determination of the ocular residence time *in vitro* was developed by CAD modeling. The 3D printed moistening chamber ensured an early differentiation of the mucoadhesive properties of different samples and was able to expand the field of *in vitro* differentiation models. Therefore, MSFI in combination with a 3D printed moistening chamber and fresh extracted porcine eyes was utilized. The developed *in situ* gelling fibers prolonged the ocular residence time compared to conventional eye drops. Furthermore, raised the incorporation of PLGA nanoparticles the ocular residence time compared to the particle free fibers. This illustrates that the partition coefficient of the dyes fluorescein sodium and DiR affects the prolongation as well. The developed lenses distributed homogenously over the cornea surface compared to the eye drops, caused by an increased sample viscosity and higher resistance against the lacrimal drainage in the performed *in vitro* experiments.

AmpB as a BCS IV molecule is a high challenging task for formulation development. The present thesis describes the successful incorporation of AmpB into the fibers under sodium cholate addition, as PLGA nanoparticle dispersion and as Eu-L polyelectrolyte complex. The prepared nanoparticles were investigated with PCS and NTA and showed narrow size distributions with PDI from 0.05-0.25 and z-average diameters from 130-250 nm with neutral zeta potential. The developed polyelectrolyte complex was successful investigated by changes of the UV/Vis and ATR-IR spectra. All results especially the UV/Vis extinction shift from 405 nm of the monomer to 315 nm of the complex spectra as well as the new transmission band at  $1554\text{ cm}^{-1}$  in the ATR-IR experiments indicate that AmpB is non-covalently bound to the carboxylic group of the polymer. The performed DSC and x-ray experiments in combination with the UV/Vis studies illustrated that AmpB is bond amorphously inside the polyelectrolyte complex, what indicates the increased distance between the AmpB molecules, which prevent crystal lattice formation.

The impact of each drug formulation onto the fiber size was investigated by ESEM and showed that the diameters range in the middle nanometer size. The eye drops, which were used off-label in clinical practice, had an AmpB concentration of 0.5 %. The fibers loaded with pure AmpB had a concentration of 0.02 %, the sodium cholate AmpB fibers had 0.04 % and the AmpB loaded nanoparticle loaded fibers had a concentration of 0.05 %. Incorporation of the polyelectrolyte complex into the fibers achieved a drug load of 0.68 % AmpB. The sodium cholate and polyelectrolyte complex loaded fibers were investigated in plate diffusion assays with *Issatchenkia orientalis* to gain information about the antimycotic activity. Only the polyelectrolyte complex loaded fibers show sufficient inhibition concentration of fungal growth. The developed complex loaded nanofibers were tested *in vitro* and showed a reduced cytotoxic potential in a multilayered cornea cell model, compared to the conventional AmpB eye drop formulation, which were used off-label in clinical practice. Furthermore, showed the formulation sufficient chemical resistance against e<sup>-</sup>-beam sterilization.

Pullulan and Gellan Gum as non-toxic pharmaceutical ingredients were used for electrospinning. Hence, a pilot study with three human volunteers were performed with drug-free fibers. Instead, fluorescein sodium was used as marker molecule. The ocular residence time of sterile placebo lenses were investigated with OCT and Pentacam<sup>®</sup> imaging. The OCT experiments showed that after 10-15 min the lens signal from the cornea disappeared and a depot in the fornix was formed. After 30 min, residual amounts of gel were detected in the fornix as well what ensured sufficient drug delivery over this period. In contrast to this, the conventional eye drops showed only slightly detectable amounts of dye in the cornea center after 5 min of instillation. High amounts of dye accumulated in the whiskers and were not able to contribute to the antimycotic therapy. After 15 min no dye signal was detected. Quantification of the OCT experiments underline, that the dye concentration from the eye drops did not exceed the signal intensity of the background. Instead, the fibers reached a 5-fold higher intensity immediately after application. As consequence, the high application frequency of the eye drops can be reduced during the therapy with the *in situ* gelling fibers. The Pentacam<sup>®</sup> images illustrated that after lens application the gel thicknesses of the measured cornea increased in contrast to the untreated eye. To complete the *in vivo* experiments the pH was determined before and after lens application to 6.5 with pH strips. The electrospun fibers showed no impact on the tear pH

after lens instillation and was characterized by good physiological compatibility *in vivo*, correlating with the performed *in vitro* experiments.

During the present work, the first solid *in situ* gelling nanofibers were prepared and characterized based on cation sensitive Gellan Gum for ocular drug delivery. The developed lenses may expand the conventional field of ocular therapies and have high potential to improve the treatment of fungal keratitis in practice. The developed AmpB-Eu L polyelectrolyte complex is able to inhibit the growth of fungal microorganisms. However, it is also interesting as well to quantify the antimycotic efficiency of the unprocessed AmpB in comparison to the non-covalent complex, to get information about the IC<sub>50</sub> values. The present PhD thesis creates a base for further animal experiments and human clinical trials to determine the relevant dose and application frequency of drug loaded fibers, which are relevant for treatment of keratomycosis. For further market establishment of the electrospun lenses, the development of an adapted primary packaging would be necessary, which ensures easy remove of the lens at sterile conditions and ensures storage as well as transport stability of the mechanical sensitive system. The application field of the developed *in situ* gelling system is not limited to the treatment of keratomycosis. The ability to load the fibers with hydrophilic as well as lipophilic drugs make bacterial infections, eye inflammations, glaucoma and age-related macular degeneration to potential fields of nanofiber application. Similar to the ocular therapy is the use of the electrospun formulation as buccal, dermal or nasal system interesting and may expand the field for prospective researches.

## References

- [1] N. Worakul, J.R. Robinson, Ocular pharmacokinetics/pharmacodynamics, *Eur. J. Pharm. Biopharm.* (1997). [https://doi.org/10.1016/S0939-6411\(97\)00064-7](https://doi.org/10.1016/S0939-6411(97)00064-7).
- [2] Q. Luo, J. Zhao, X. Zhang, W. Pan, Nanostructured lipid carrier (NLC) coated with Chitosan Oligosaccharides and its potential use in ocular drug delivery system, *Int. J. Pharm.* 403 (2011) 185–191. <https://doi.org/10.1016/j.ijpharm.2010.10.013>.
- [3] Y. Ohashi, M. Dogru, K. Tsubota, Laboratory findings in tear fluid analysis, *Clin. Chim. Acta.* 369 (2006) 17–28. <https://doi.org/10.1016/j.cca.2005.12.035>.
- [4] J.M. Tiffany, Physiological functions of the meibomian glands, *Prog. Retin. Eye Res.* (1995). [https://doi.org/10.1016/1350-9462\(93\)E0008-R](https://doi.org/10.1016/1350-9462(93)E0008-R).
- [5] K.P. Mashige, A review of corneal diameter, curvature and thickness values and influencing factors\*, *African Vis. Eye Heal.* (2013). <https://doi.org/10.4102/aveh.v72i4.58>.
- [6] M.J. Doughty, M.L. Zaman, Human corneal thickness and its impact on intraocular pressure measures: A review and meta-analysis approach, *Surv. Ophthalmol.* 44 (2000) 367–408. [https://doi.org/10.1016/S0039-6257\(00\)00110-7](https://doi.org/10.1016/S0039-6257(00)00110-7).
- [7] J.B. Randleman, M.J. Lynn, C.E. Perez-Staziota, H.M. Weissman, S.W. Kim, Comparison of central and peripheral corneal thickness measurements with scanning-slit, Scheimpflug and Fourier-domain ocular coherence tomography, *Br. J. Ophthalmol.* 99 (2015) 1176–1181. <https://doi.org/10.1136/bjophthalmol-2014-306340>.
- [8] M.H. Dastjerdi, Z. Sadrai, D.R. Saban, Q. Zhang, R. Dana, Corneal penetration of topical and subconjunctival bevacizumab, *Investig. Ophthalmol. Vis. Sci.* 52 (2011) 8718–8723. <https://doi.org/10.1167/iovs.11-7871>.
- [9] T. Zhang, C.D. Xiang, D. Gale, S. Carreiro, E.Y. Wu, E.Y. Zhang, Drug transporter and cytochrome P450 mRNA expression in human ocular barriers: Implications for ocular drug disposition, *Drug Metab. Dispos.* (2008). <https://doi.org/10.1124/dmd.108.021121>.
- [10] C. Kölln, S. Reichl, mRNA expression of metabolic enzymes in human cornea, corneal cell lines, and hemicornea constructs, *J. Ocul. Pharmacol. Ther.* 28 (2012) 271–277. <https://doi.org/10.1089/jop.2011.0124>.
- [11] J. Inoue, M. Oka, Y. Aoyama, S. Kobayashi, S. Ueno, N. Hada, T. Takeda, M. Takehana, Effects of Dorzolamide Hydrochloride on Ocular Tissues, *J. Ocul. Pharmacol. Ther.* (2004). <https://doi.org/10.1089/108076804772745419>.
- [12] M. Kuwano, H. Ibuki, N. Morikawa, A. Ota, Y. Kawashima, Cyclosporine A formulation affects its ocular distribution in rabbits, *Pharm. Res.* (2002). <https://doi.org/10.1023/A:1013671819604>.
- [13] P. Van Hoogevest, B. De Kruijff, Effect of amphotericin B on cholesterol-containing liposomes of egg phosphatidylcholine and didocosenoil phosphatidylcholine. A refinement of the model for the formation of pores by amphotericin B in membranes, *BBA - Biomembr.* 511 (1978) 397–407. [https://doi.org/10.1016/0005-2736\(78\)90276-6](https://doi.org/10.1016/0005-2736(78)90276-6).
- [14] H.K. Ruiz, D.R. Serrano, M.A. Dea-Ayuela, P.E. Bilbao-Ramos, F. Bolás-Fernández, J.J. Torrado, G. Molero, New amphotericin B-gamma cyclodextrin formulation for topical use with synergistic

- activity against diverse fungal species and *Leishmania* spp, *Int. J. Pharm.* 473 (2014) 148–157.  
<https://doi.org/10.1016/j.ijpharm.2014.07.004>.
- [15] A. Zheng, E.K. Chin, D.R.P. Almeida, S.H. Tsang, V.B. Mahajan, Combined Vitrectomy and Intravitreal Dexamethasone (Ozurdex) Sustained-Release Implant, *Retina*. 36 (2016) 2087–2092.  
<https://doi.org/10.1097/IAE.0000000000001063>.
- [16] J. Jiang, H.S. Gill, D. Ghate, B.E. McCarey, S.R. Patel, H.F. Edelhauser, M.R. Prausnitz, Coated microneedles for drug delivery to the eye, *Investig. Ophthalmol. Vis. Sci.* (2007).  
<https://doi.org/10.1167/iovs.07-0066>.
- [17] J.B. Ciolino, C.F. Stefanescu, A.E. Ross, B. Salvador-Culla, P. Cortez, E.M. Ford, K.A. Wymbs, S.L. Sprague, D.R. Mascoop, S.S. Rudina, S.A. Trauger, F. Cade, D.S. Kohane, In vivo performance of a drug-eluting contact lens to treat glaucoma for a month, *Biomaterials*. 35 (2014) 432–439.  
<https://doi.org/10.1016/j.biomaterials.2013.09.032>.
- [18] H. Hiratani, A. Fujiwara, Y. Tamiya, Y. Mizutani, C. Alvarez-Lorenzo, Ocular release of timolol from molecularly imprinted soft contact lenses, *Biomaterials*. 26 (2005) 1293–1298.  
<https://doi.org/10.1016/J.BIOMATERIALS.2004.04.030>.
- [19] E. Stefansson, G.N. Foulks, R.C. Hamilton, The effect of corneal contact lenses on the oxygen tension in the anterior chamber of the rabbit eye, *Investig. Ophthalmol. Vis. Sci.* (1987).
- [20] Gagandeep, T. Garg, B. Malik, G. Rath, A.K. Goyal, Development and characterization of nano-fiber patch for the treatment of glaucoma, *Eur. J. Pharm. Sci.* 53 (2014) 10–16.  
<https://doi.org/10.1016/j.ejps.2013.11.016>.
- [21] J. Sirc, S. Kubinova, R. Hobzova, D. Stranska, P. Kozlik, Z. Bosakova, D. Marekova, V. Holan, E. Sykova, J. Michalek, Controlled gentamicin release from multi-layered electrospun nanofibrous structures of various thicknesses., *Int. J. Nanomedicine*. 7 (2012) 5315–25.  
<https://doi.org/10.2147/IJN.S35781>.
- [22] D. Atila, D. Keskin, A. Tezcaner, Cellulose acetate based 3-dimensional electrospun scaffolds for skin tissue engineering applications, *Carbohydr. Polym.* 133 (2015) 251–261.  
<https://doi.org/10.1016/J.CARBPOL.2015.06.109>.
- [23] B. Göttel, J.M. de Souza e Silva, C. Santos de Oliveira, F. Syrowatka, M. Fiorentzis, A. Viestenz, A. Viestenz, K. Mäder, Electrospun nanofibers – A promising solid in-situ gelling alternative for ocular drug delivery, *Eur. J. Pharm. Biopharm.* 146 (2020) 125–132.  
<https://doi.org/10.1016/j.ejpb.2019.11.012>.
- [24] E. Eljarrat-Binstock, A.J. Domb, Iontophoresis: A non-invasive ocular drug delivery, *J. Control. Release.* (2006). <https://doi.org/10.1016/j.jconrel.2005.09.049>.
- [25] Vincent Hon-Kin Li, J.R. Robinson, Solution viscosity effects on the ocular disposition of cromolyn sodium in the albino rabbit, *Int. J. Pharm.* 53 (1989) 219–225. [https://doi.org/10.1016/0378-5173\(89\)90315-3](https://doi.org/10.1016/0378-5173(89)90315-3).
- [26] J. Grove, M. Durr, M.P. Quint, B. Plazonnet, The effect of vehicle viscosity on the ocular bioavailability of L-653,328, *Int. J. Pharm.* 66 (1990) 23–28. [https://doi.org/10.1016/0378-5173\(90\)90380-M](https://doi.org/10.1016/0378-5173(90)90380-M).
- [27] L. Mayol, F. Quaglia, A. Borzacchiello, L. Ambrosio, M.I. La Rotonda, A novel



- poloxamers/hyaluronic acid in situ forming hydrogel for drug delivery: Rheological, mucoadhesive and in vitro release properties, *Eur. J. Pharm. Biopharm.* 70 (2008) 199–206.  
<https://doi.org/10.1016/J.EJPB.2008.04.025>.
- [28] H. Ibrahim, C. Bindschaedler, E. Doelker, P. Buri, R. Gurny, Concept and development of ophthalmic pseudo-latexes triggered by pH, *Int. J. Pharm.* 77 (1991) 211–219.  
[https://doi.org/10.1016/0378-5173\(91\)90319-J](https://doi.org/10.1016/0378-5173(91)90319-J).
- [29] A. Rozier, C. Mazuel, J. Grove, B. Plazonnet, Gelrite®: A novel, ion-activated, in-situ gelling polymer for ophthalmic vehicles. Effect on bioavailability of timolol, *Int. J. Pharm.* 57 (1989) 163–168. [https://doi.org/10.1016/0378-5173\(89\)90305-0](https://doi.org/10.1016/0378-5173(89)90305-0).
- [30] T. Gratieri, G.M. Gelfuso, E.M. Rocha, V.H. Sarmiento, O. de Freitas, R.F.V. Lopez, A poloxamer/chitosan in situ forming gel with prolonged retention time for ocular delivery, *Eur. J. Pharm. Biopharm.* 75 (2010) 186–193. <https://doi.org/10.1016/j.ejpb.2010.02.011>.
- [31] A. Bernkop-Schnürch, M. Hornof, T. Zoidl, Thiolated polymers - Thiomers: Synthesis and in vitro evaluation of chitosan-2-iminothiolane conjugates, *Int. J. Pharm.* 260 (2003) 229–237.  
[https://doi.org/10.1016/S0378-5173\(03\)00271-0](https://doi.org/10.1016/S0378-5173(03)00271-0).
- [32] Y. Sakai, S.I. Yasueda, A. Ohtori, Stability of latanoprost in an ophthalmic lipid emulsion using polyvinyl alcohol, *Int. J. Pharm.* 305 (2005) 176–179. <https://doi.org/10.1016/j.ijpharm.2005.08.017>.
- [33] M.D. Hornof, C.E. Kast, A. Bernkop-Schnürch, In vitro evaluation of the viscoelastic properties of chitosan-thioglycolic acid conjugates, *Eur. J. Pharm. Biopharm.* 55 (2003) 185–190.  
[https://doi.org/10.1016/S0939-6411\(02\)00162-5](https://doi.org/10.1016/S0939-6411(02)00162-5).
- [34] A. Bernkop-Schnürch, Thiomers: A new generation of mucoadhesive polymers, *Adv. Drug Deliv. Rev.* 57 (2005) 1569–1582. <https://doi.org/10.1016/j.addr.2005.07.002>.
- [35] J. Nepp, W. Knoetzl, A. Prinz, S. Hoeller, M. Prinz, Management of moderate-to-severe dry eye disease using chitosan-N-acetylcysteine (Lacrimera®) eye drops: a retrospective case series, *Int. Ophthalmol.* 40 (2020) 1547–1552. <https://doi.org/10.1007/s10792-020-01324-5>.
- [36] T. Bourcier, A. Sauer, A. Dory, J. Denis, M. Sabou, Fungal keratitis, *J. Fr. Ophtalmol.* 40 (2017) e307–e313. <https://doi.org/10.1016/j.jfo.2017.08.001>.
- [37] M.J. Bharathi, R. Ramakrishnan, R. Meenakshi, S. Padmavathy, C. Shivakumar, M. Srinivasan, Microbial Keratitis in South India: Influence of Risk Factors, Climate, and Geographical Variation, *Ophthalmic Epidemiol.* 14 (2007) 61–69. <https://doi.org/10.1080/09286580601001347>.
- [38] M. Green, A. Apel, F. Stapleton, Risk factors and causative organisms in microbial keratitis, *Cornea.* 27 (2008) 22–27. <https://doi.org/10.1097/ICO.0b013e318156caf2>.
- [39] P. Bhartiya, M. Daniell, M. Constantinou, F.M.A. Islam, H.R. Taylor, Fungal keratitis in Melbourne, *Clin. Exp. Ophthalmol.* 35 (2007) 124–130. <https://doi.org/10.1111/j.1442-9071.2006.01405.x>.
- [40] M. Roth, L. Daas, A. Renner-Wilde, N. Cvetkova-Fischer, M. Saeger, M. Herwig-Carl, M. Matthaiei, A. Fekete, V. Kakkassery, G. Walther, M. von Lilienfeld-Toal, C. Mertens, J. Lenk, J. Mehlan, C. Fischer, M. Fuest, S. Kroll, W. Bayouth, A. Viestenz, A. Frings, C.R. MacKenzie, E.M. Messmer, B. Seitz, O. Kurzai, G. Geerling, The German keratomycosis registry: Initial results of a multicenter survey, *Ophthalmologie.* 116 (2019) 957–966. <https://doi.org/10.1007/s00347-019-0871-9>.
- [41] S.E. Nielsen, E. Nielsen, H.O. Julian, J. Lindegaard, K. Højgaard, A. Ivarsen, J. Hjortdal, S.

- Heegaard, Incidence and clinical characteristics of fungal keratitis in a Danish population from 2000 to 2013, *Acta Ophthalmol.* (2015). <https://doi.org/10.1111/aos.12440>.
- [42] M.A. Thiel, A.S. Zinkernagel, J. Burhenne, C. Kaufmann, W.E. Haefeli, Voriconazole concentration in human aqueous humor and plasma during topical or combined topical and systemic administration for fungal keratitis, *Antimicrob. Agents Chemother.* 51 (2007) 239–244. <https://doi.org/10.1128/AAC.00762-06>.
- [43] W. Behrens-Baumann, D. Finis, C. Mackenzie, M. Roth, G. Geerling, Keratomykose - Therapiestandards und aktuelle Entwicklungen, *Klin. Monbl. Augenheilkd.* 232 (2015) 754–764. <https://doi.org/10.1055/s-0035-1546032>.
- [44] S. Farrell, E. McElnea, S. Moran, S. Knowles, C.C. Murphy, Fungal keratitis in the Republic of Ireland, *Eye.* 31 (2017) 1427–1434. <https://doi.org/10.1038/eye.2017.82>.
- [45] C.S.F. Picone, R.L. da Cunha, Interactions between milk proteins and gellan gum in acidified gels, *Food Hydrocoll.* 24 (2010) 502–511. <https://doi.org/10.1016/j.foodhyd.2009.12.007>.
- [46] J.T. Oliveira, L. Martins, R. Picciochi, P.B. Malafaya, R.A. Sousa, N.M. Neves, J.F. Mano, R.L. Reis, Gellan gum: A new biomaterial for cartilage tissue engineering applications, *J. Biomed. Mater. Res. - Part A.* (2010). <https://doi.org/10.1002/jbm.a.32574>.
- [47] S.A. Agnihotri, S.S. Jawalkar, T.M. Aminabhavi, Controlled release of cephalexin through gellan gum beads: Effect of formulation parameters on entrapment efficiency, size, and drug release, *Eur. J. Pharm. Biopharm.* 63 (2006) 249–261. <https://doi.org/10.1016/J.EJPB.2005.12.008>.
- [48] P.-E. Jansson, B. Lindberg, P.A. Sandford, Structural studies of gellan gum, an extracellular polysaccharide elaborated by *Pseudomonas elodea*, *Carbohydr. Res.* 124 (1983) 135–139. [https://doi.org/10.1016/0008-6215\(83\)88361-X](https://doi.org/10.1016/0008-6215(83)88361-X).
- [49] K.S. Kang, G.T. Veeder, P.J. Mirrasoul, Agar-like polysaccharide produced by a *Pseudomonas* species: production and basic properties, *Appl. Environ. Microbiol.* (1982). <https://doi.org/10.1128/aem.43.5.1086-1091.1982>.
- [50] H. Grasdalen, O. Smidsrød, Gelation of gellan gum, *Carbohydr. Polym.* 7 (1987) 371–393. [https://doi.org/10.1016/0144-8617\(87\)90004-X](https://doi.org/10.1016/0144-8617(87)90004-X).
- [51] E.R. Morris, K. Nishinari, M. Rinaudo, Gelation of gellan – A review, *Food Hydrocoll.* 28 (2012) 373–411. <https://doi.org/10.1016/J.FOODHYD.2012.01.004>.
- [52] B.J. Catley, A. Ramsay, C. Servis, Observations on the structure of the fungal extracellular polysaccharide, pullulan, *Carbohydr. Res.* 153 (1986) 79–86. [https://doi.org/10.1016/S0008-6215\(00\)90197-6](https://doi.org/10.1016/S0008-6215(00)90197-6).
- [53] H. Bender, J. Lehmann, K. Wallenfels, Pullulan, ein extracelluläres Glucan von *Pullularia pullulans*, *Biochim. Biophys. Acta.* 36 (1959) 309–316. [https://doi.org/10.1016/0006-3002\(59\)90172-6](https://doi.org/10.1016/0006-3002(59)90172-6).
- [54] T. Kimoto, T. Shibuya, S. Shiobara, Safety studies of a novel starch, pullulan: Chronic toxicity in rats and bacterial mutagenicity, *Food Chem. Toxicol.* 35 (1997) 323–329. [https://doi.org/10.1016/S0278-6915\(97\)00001-X](https://doi.org/10.1016/S0278-6915(97)00001-X).
- [55] A. de Arce Velasquez, L.M. Ferreira, M.F.L. Stangarlin, C. de B. da Silva, C.M.B. Rolim, L. Cruz, Novel Pullulan–Eudragit® S100 blend microparticles for oral delivery of risedronate: Formulation, in vitro evaluation and tableting of blend microparticles, *Mater. Sci. Eng. C.* 38 (2014) 212–217.

- <https://doi.org/10.1016/J.MSEC.2014.02.003>.
- [56] A.C. Stijnman, I. Bodnar, R. Hans Tromp, Electrospinning of food-grade polysaccharides, *Food Hydrocoll.* 25 (2011) 1393–1398. <https://doi.org/10.1016/J.FOODHYD.2011.01.005>.
- [57] M.R. Karim, H.W. Lee, R. Kim, B.C. Ji, J.W. Cho, T.W. Son, W. Oh, J.H. Yeum, Preparation and characterization of electrospun pullulan/montmorillonite nanofiber mats in aqueous solution, *Carbohydr. Polym.* 78 (2009) 336–342. <https://doi.org/10.1016/J.CARBPOL.2009.04.024>.
- [58] K. Kycia, A. Chlebowska-Śmigiel, M. Gniewosz, E. Sokół, Effect of pullulan on the physicochemical properties of yoghurt, *Int. J. Dairy Technol.* (2018). <https://doi.org/10.1111/1471-0307.12401>.
- [59] T. Diab, C.G. Biliaderis, D. Gerasopoulos, E. Sfakiotakis, Physicochemical properties and application of pullulan edible films and coatings in fruit preservation, *J. Sci. Food Agric.* 81 (2001) 988–1000. <https://doi.org/10.1002/jsfa.883>.
- [60] S. Jahanshahi-Anbuhi, K. Pennings, V. Leung, M. Liu, C. Carrasquilla, B. Kannan, Y. Li, R. Pelton, J.D. Brennan, C.D.M. Filipe, Pullulan Encapsulation of Labile Biomolecules to Give Stable Bioassay Tablets, *Angew. Chemie Int. Ed.* 53 (2014) 6155–6158. <https://doi.org/10.1002/anie.201403222>.
- [61] Y. Murata, T. Isobe, K. Kofuji, N. Nishida, R. Kamaguchi, Preparation of Fast Dissolving Films for Oral Dosage from Natural Polysaccharides, *Materials (Basel)*. 3 (2010) 4291–4299. <https://doi.org/10.3390/ma3084291>.
- [62] Plantcaps® Vegetarian Capsules | Capsugel, (n.d.). <https://www.capsugel.com/consumer-health-nutrition-products/plantcaps-capsules> (accessed July 6, 2020).
- [63] T.S. Nguyen, P.M.M. Weers, V. Raussens, Z. Wang, G. Ren, T. Sulchek, P.D. Hoepflich, R.O. Ryan, Amphotericin B induces interdigitation of apolipoprotein stabilized nanodisk bilayers, *Biochim. Biophys. Acta - Biomembr.* 1778 (2008) 303–312. <https://doi.org/10.1016/j.bbamem.2007.10.005>.
- [64] D. Ellis, Amphotericin B: spectrum and resistance, *J. Antimicrob. Chemother.* (2002). [https://doi.org/10.1093/jac/49.suppl\\_1.7](https://doi.org/10.1093/jac/49.suppl_1.7).
- [65] G. Deray, L. Mercadal, C. Bagnis, Amphotericin B nephrotoxicity, *Nephrologie.* 23 (2002) 119–122. [https://doi.org/10.1093/jac/49.suppl\\_1.37](https://doi.org/10.1093/jac/49.suppl_1.37).
- [66] M. Tiphine, V. Letscher-Bru, R. Herbrecht, Amphotericin B and its new formulations: Pharmacologic characteristics, clinical efficacy, and tolerability, *Transpl. Infect. Dis.* 1 (1999) 273–283. <https://doi.org/10.1034/j.1399-3062.1999.010406.x>.
- [67] L. Kristanc, B. Božič, Š.Z. Jokhadar, M.S. Dolenc, G. Gomišček, The pore-forming action of polyenes: From model membranes to living organisms, *Biochim. Biophys. Acta - Biomembr.* 1861 (2019) 418–430. <https://doi.org/10.1016/j.bbamem.2018.11.006>.
- [68] J.J. Torrado, R. Espada, M.P. Ballesteros, S. Torrado-Santiago, Amphotericin B Formulations and Drug Targeting, *J. Pharm. Sci.* 97 (2008) 2405–2425. <https://doi.org/10.1002/jps.21179>.
- [69] A. Lemke, A.F. Kiderlen, O. Kayser, Amphotericin B, *Appl. Microbiol. Biotechnol.* (2005). <https://doi.org/10.1007/s00253-005-1955-9>.
- [70] *Arzneibuch-Kommentar 6.3/1292*, (n.d.). [http://dlib.bibliothek.uni-halle.de:8082/Xaver/start.xav?startbk=DAPV\\_PhEurKomm\\_8\\_D&bk=DAPV\\_PhEurKomm\\_8\\_D&S ID=Anonymous5941092352&skin=div&startSkin=div#\\_DAPV\\_PhEurKomm\\_8\\_D\\_\\_%2F%2F\\*%2F](http://dlib.bibliothek.uni-halle.de:8082/Xaver/start.xav?startbk=DAPV_PhEurKomm_8_D&bk=DAPV_PhEurKomm_8_D&S ID=Anonymous5941092352&skin=div&startSkin=div#_DAPV_PhEurKomm_8_D__%2F%2F*%2F)

- 5B%40attr\_id%3D%27Bd3-Amphotericin-B%27%5D\_\_1594109244777 (accessed July 7, 2020).
- [71] J.A. Sánchez-Brunete, M.A. Dea, S. Rama, F. Bolás, J.M. Alunda, S. Torrado-Santiago, J.J. Torrado, Amphotericin B molecular organization as an essential factor to improve activity/toxicity ratio in the treatment of visceral leishmaniasis, *J. Drug Target.* 12 (2004) 453–460.  
<https://doi.org/10.1080/10611860400006596>.
- [72] F. Gaboriau, M. Chéron, L. Leroy, J. Bolard, Physico-chemical properties of the heat-induced “superaggregates” of amphotericin B, *Biophys. Chem.* 66 (1997) 1–12.  
[https://doi.org/10.1016/S0301-4622\(96\)02241-7](https://doi.org/10.1016/S0301-4622(96)02241-7).
- [73] B. Göttel, J.M. de Souza e Silva, C. de Santos, F. Syrowatka, M. Fiorentzis, A. Viestenz, A. Viestenz, K. Mäder, Electrospun nanofibers – a promising solid in - situ gelling alternative for ocular drug delivery, *Eur. J. Pharm. Biopharm.* (2020).
- [74] C.J. Thompson, G.G. Chase, A.L. Yarin, D.H. Reneker, Effects of parameters on nanofiber diameter determined from electrospinning model, *Polymer (Guildf).* (2007).  
<https://doi.org/10.1016/j.polymer.2007.09.017>.
- [75] J.M. Deitzel, J. Kleinmeyer, D. Harris, N.C. Beck Tan, The effect of processing variables on the morphology of electrospun nanofibers and textiles, *Polymer (Guildf).* 42 (2001) 261–272.  
[https://doi.org/10.1016/S0032-3861\(00\)00250-0](https://doi.org/10.1016/S0032-3861(00)00250-0).
- [76] H. Van de Ven, C. Paulussen, P.B. Feijens, A. Matheussen, P. Rombaut, P. Kayaert, G. Van den Mooter, W. Weyenberg, P. Cos, L. Maes, A. Ludwig, PLGA nanoparticles and nanosuspensions with amphotericin B: Potent in vitro and in vivo alternatives to Fungizone and AmBisome, *J. Control. Release.* 161 (2012) 795–803. <https://doi.org/10.1016/j.jconrel.2012.05.037>.
- [77] J. Lyklema, Electrokinetics after Smoluchowski, in: *Colloids Surfaces A Physicochem. Eng. Asp.*, 2003. [https://doi.org/10.1016/S0927-7757\(03\)00217-6](https://doi.org/10.1016/S0927-7757(03)00217-6).
- [78] A.H.A. Mohamed-Ahmed, K.A. Les, K. Seifert, S.L. Croft, S. Brocchini, Noncovalent complexation of amphotericin-B with poly( $\alpha$ -glutamic acid), *Mol. Pharm.* (2013).  
<https://doi.org/10.1021/mp300339p>.
- [79] K.A. Les, A.H.A. Mohamed-Ahmed, S. Balan, J.W. Choi, D. Martin, V. Yardley, K. Powell, A. Godwin, S. Brocchini, Poly(methacrylic acid) complexation of amphotericin B to treat neglected diseases, *Polym. Chem.* (2014). <https://doi.org/10.1039/c3py01051a>.
- [80] K. Jores, W. Mehnert, M. Drechsler, H. Bunjes, C. Johann, K. Mäder, Investigations on the structure of solid lipid nanoparticles (SLN) and oil-loaded solid lipid nanoparticles by photon correlation spectroscopy, field-flow fractionation and transmission electron microscopy, *J. Control. Release.* (2004). <https://doi.org/10.1016/j.jconrel.2003.11.012>.
- [81] S. Mao, C. Augsten, K. Mäder, T. Kissel, Characterization of chitosan and its derivatives using asymmetrical flow field-flow-fractionation: A comparison with traditional methods, *J. Pharm. Biomed. Anal.* (2007). <https://doi.org/10.1016/j.jpba.2007.08.012>.
- [82] D. Huang, E.A. Swanson, C.P. Lin, J.S. Schuman, W.G. Stinson, W. Chang, M.R. Hee, T. Flotte, K. Gregory, C.A. Puliafito, J.G. Fujimoto, Optical coherence tomography, *Science* (80-. ). (1991).  
<https://doi.org/10.1126/science.1957169>.
- [83] J.S. Schuman, M.R. Hee, A. V. Arya, T. Pedut-Kloizman, C.A. Puliafito, J.G. Fujimoto, E.A.

- Swanson, Optical coherence tomography: A new tool for glaucoma diagnosis, *Curr. Opin. Ophthalmol.* (1995). <https://doi.org/10.1097/00055735-199504000-00014>.
- [84] P.A. Keane, P.J. Patel, S. Liakopoulos, F.M. Heussen, S.R. Sadda, A. Tufail, Evaluation of Age-related Macular Degeneration With Optical Coherence Tomography, *Surv. Ophthalmol.* 57 (2012) 389–414. <https://doi.org/10.1016/j.survophthal.2012.01.006>.
- [85] A. Ishibazawa, T. Nagaoka, A. Takahashi, T. Omae, T. Tani, K. Sogawa, H. Yokota, A. Yoshida, Optical coherence tomography angiography in diabetic retinopathy: A prospective pilot study, *Am. J. Ophthalmol.* 160 (2015) 35–44.e1. <https://doi.org/10.1016/j.ajo.2015.04.021>.
- [86] Y. Jia, S.T. Bailey, D.J. Wilson, O. Tan, M.L. Klein, C.J. Flaxel, B. Potsaid, J.J. Liu, C.D. Lu, M.F. Kraus, J.G. Fujimoto, D. Huang, Quantitative optical coherence tomography angiography of choroidal neovascularization in age-related macular degeneration, *Ophthalmology.* 121 (2014) 1435–1444. <https://doi.org/10.1016/j.ophtha.2014.01.034>.
- [87] C. O'Donnell, C. Maldonado-Codina, Agreement and repeatability of central thickness measurement in normal corneas using ultrasound pachymetry and the OCULUS Pentacam, *Cornea.* 24 (2005) 920–924. <https://doi.org/10.1097/01.ico.0000157422.01146.e9>.
- [88] R.L. Epstein, Y.L. Chiu, G.L. Epstein, Pentacam HR criteria for curvature change in keratoconus and postoperative LASIK ectasia, *J. Refract. Surg.* (2012). <https://doi.org/10.3928/1081597X-20121115-04>.
- [89] E.R. Morris, A.N. Cutler, S.B. Ross-Murphy, D.A. Rees, J. Price, Concentration and shear rate dependence of viscosity in random coil polysaccharide solutions, *Carbohydr. Polym.* 1 (1981) 5–21. [https://doi.org/10.1016/0144-8617\(81\)90011-4](https://doi.org/10.1016/0144-8617(81)90011-4).
- [90] T. Han, A.L. Yarin, D.H. Reneker, Viscoelastic electrospun jets: Initial stresses and elongational rheometry, *Polymer (Guildf).* 49 (2008) 1651–1658. <https://doi.org/10.1016/J.POLYMER.2008.01.035>.
- [91] P.M. Tomasula, A.M.M. Sousa, S.C. Liou, R. Li, L.M. Bonnaillie, L.S. Liu, Short communication: Electrospinning of casein/pullulan blends for food-grade applications, *J. Dairy Sci.* 99 (2016) 1837–1845. <https://doi.org/10.3168/jds.2015-10374>.
- [92] T. Uyar, F. Besenbacher, Electrospinning of uniform polystyrene fibers: The effect of solvent conductivity, *Polymer (Guildf).* (2008). <https://doi.org/10.1016/j.polymer.2008.09.025>.
- [93] H. Fong, I. Chun, D.H. Reneker, Beaded nanofibers formed during electrospinning, in: *Polymer (Guildf).*, Elsevier Science Ltd, 1999: pp. 4585–4592. [https://doi.org/10.1016/S0032-3861\(99\)00068-3](https://doi.org/10.1016/S0032-3861(99)00068-3).
- [94] V. Jacobs, R.D. Anandjiwala, M. Maaza, The influence of electrospinning parameters on the structural morphology and diameter of electrospun nanofibers, *J. Appl. Polym. Sci.* 115 (2010) 3130–3136. <https://doi.org/10.1002/app.31396>.
- [95] B. Pant, M. Park, S.-J. Park, Drug Delivery Applications of Core-Sheath Nanofibers Prepared by Coaxial Electrospinning: A Review, *Pharmaceutics.* 11 (2019) 305. <https://doi.org/10.3390/pharmaceutics11070305>.
- [96] R. Lord, On the instability of a cylinder of viscous liquid under capillary force., *PHILOS. MAG.* 34, 1892 (1892) 145–154. <https://doi.org/10.1080/14786449208620301>.

- [97] S.-H. Tan, R. Inai, M. Kotaki, S. Ramakrishna, Systematic parameter study for ultra-fine fiber fabrication via electrospinning process, *Polymer (Guildf)*. 46 (2005) 6128–6134. <https://doi.org/10.1016/j.polymer.2005.05.068>.
- [98] J.P. Craig, I. Singh, A. Tomlinson, P.B. Morgan, The role of tear physiology in ocular surface temperature, *Eye*. 14 (2000) 635–641. <https://doi.org/10.1038/eye.2000.156>.
- [99] J. Carlfors, K. Edsman, R. Petersson, K. Jörnving, Rheological evaluation of Gelrite® in situ gels for ophthalmic use, *Eur. J. Pharm. Sci.* 6 (1998) 113–119. [https://doi.org/10.1016/S0928-0987\(97\)00074-2](https://doi.org/10.1016/S0928-0987(97)00074-2).
- [100] M. Oechsner, S. Keipert, Polyacrylic acid/polyvinylpyrrolidone bipolymeric systems. I. Rheological and mucoadhesive properties of formulations potentially useful for the treatment of dry-eye-syndrome, *Eur. J. Pharm. Biopharm.* 47 (1999) 113–118. [https://doi.org/10.1016/S0939-6411\(98\)00070-8](https://doi.org/10.1016/S0939-6411(98)00070-8).
- [101] A. Paudel, M. Geppi, G. Van den Mooter, Structural and Dynamic Properties of Amorphous Solid Dispersions: The Role of Solid-State Nuclear Magnetic Resonance Spectroscopy and Relaxometry, *J. Pharm. Sci.* 103 (2014) 2635–2662. <https://doi.org/10.1002/jps.23966>.
- [102] M. Bastrop, A. Meister, H. Metz, S. Drescher, B. Dobner, K. Mäder, A. Blume, Water dynamics in bolaamphiphile hydrogels investigated by <sup>1</sup>H NMR relaxometry and diffusometry, *J. Phys. Chem. B*. 115 (2011) 14–22. <https://doi.org/10.1021/jp107755k>.
- [103] M.A.L. Guevara, Y.M. Torres, J.C.G. Naranjo, N.R. Suárez, L.C.S. Beyries, M.A.M. Feliu, T.S. Boada, I.C.R. Reyes, J. Philippé, Plasma Dynamic Viscosity Determined by NMR, *Appl. Magn. Reson.* 49 (2018) 1075–1083. <https://doi.org/10.1007/s00723-018-1026-x>.
- [104] C. Blümer, K. Mäder, Isostatic ultra-high-pressure effects on supercooled melts in colloidal triglyceride dispersions, *Pharm. Res.* 22 (2005) 1708–1715. <https://doi.org/10.1007/s11095-005-6949-x>.
- [105] R. Okada, S. Matsukawa, T. Watanabe, Hydration structure and dynamics in pullulan aqueous solution based on <sup>1</sup>H NMR relaxation time, *J. Mol. Struct.* 602–603 (2002) 473–483. [https://doi.org/10.1016/S0022-2860\(01\)00728-1](https://doi.org/10.1016/S0022-2860(01)00728-1).
- [106] B.P. Hills, J.E.M. Snaar, Water proton relaxation studies of pore microstructure in monodisperse glass bead beds, *Mol. Phys.* 84 (1995) 141–157. <https://doi.org/10.1080/00268979500100111>.
- [107] C. Ferrero, D. Massuelle, D. Jeannerat, E. Doelker, Towards elucidation of the drug release mechanism from compressed hydrophilic matrices made of cellulose ethers. I. Pulse-field-gradient spin-echo NMR study of sodium salicylate diffusivity in swollen hydrogels with respect to polymer matrix physical structure, *J. Control. Release.* 128 (2008) 71–79. <https://doi.org/10.1016/j.jconrel.2008.02.006>.
- [108] Y. Aso, S. Yoshioka, S. Kojima, Determination of the diffusion coefficient of insulin and lysozyme in crosslinked dextran hydrogels by pulsed-field-gradient NMR, *Chem. Pharm. Bull.* 46 (1998) 1836–1839. <https://doi.org/10.1248/cpb.46.1836>.
- [109] M. Saenz-De-Viteri, P. Fernández-Robredo, E. De Nova, E. Bonet-Faeriol, A.L. Sabater, J. Zarranz-Ventura, J. Caire, L.M. Sádaba, A. Salinas-Alamán, A. García-Layana, Comparative study measuring the dilatatory effect of a mydriatic device (Mydriaser®) versus topical drops, *Int. J. Ophthalmol.* 6

- (2013) 801–804. <https://doi.org/10.3980/j.issn.2222-3959.2013.06.11>.
- [110] J.D. Brandt, K. Sall, H. DuBiner, R. Benza, Y. Alster, G. Walker, C.P. Semba, Six-Month Intraocular Pressure Reduction with a Topical Bimatoprost Ocular Insert: Results of a Phase II Randomized Controlled Study, in: *Ophthalmology*, Elsevier Inc., 2016: pp. 1685–1694. <https://doi.org/10.1016/j.ophtha.2016.04.026>.
- [111] C. Faber, E. Scherfig, J.U. Prause, K.E. Sørensen, Corneal thickness in pigs measured by ultrasound pachymetry in vivo, *Scand. J. Lab. Anim. Sci.* (2008).
- [112] J. Heichel, F. Wilhelm, K.S. Kunert, T. Hammer, Topographic Findings of the Porcine Cornea., *Med. Hypothesis, Discov. Innov. Ophthalmol. J.* 5 (2016) 125–131. <https://www.ncbi.nlm.nih.gov/pmc/articles/PMC5346302/> (accessed April 24, 2019).
- [113] P.M. Kiely, G. Smith, L.G. Carney, Meridional variations of corneal shape, *Am. J. Optom. Physiol. Opt.* (1984). <https://doi.org/10.1097/00006324-198410000-00001>.
- [114] Z. Wang, K. Gao, J. Chen, Y. Hong, X. Ge, D. Wang, Z. Pan, P. Zhu, W. Yun, C. Jacobsen, Z. Wu, Advantages of intermediate X-ray energies in Zernike phase contrast X-ray microscopy, *Biotechnol. Adv.* 31 (2013) 387–392. <https://doi.org/10.1016/j.biotechadv.2012.04.001>.
- [115] X. Huang, N. Li, D. Wang, Y. Luo, Z. Wu, Z. Guo, Q. Jin, Z. Liu, Y. Huang, Y. Zhang, C. Wu, Quantitative three-dimensional analysis of poly (lactic-co-glycolic acid) microsphere using hard X-ray nano-tomography revealed correlation between structural parameters and drug burst release, *J. Pharm. Biomed. Anal.* 112 (2015) 43–49. <https://doi.org/10.1016/j.jpba.2015.04.017>.
- [116] A. Fernández-Ferreiro, J. Silva-Rodríguez, F.J. Otero-Espinar, M. González-Barcia, M.J. Lamas, A. Ruibal, A. Luaces-Rodríguez, A. Vieites-Prado, I. Lema, M. Herranz, N. Gómez-Lado, J. Blanco-Mendez, M. Gil-Martínez, M. Pardo, A. Moscoso, J. Cortes, M. Sánchez-Martínez, J. Pardo-Montero, P. Aguiar, In vivo eye surface residence determination by high-resolution scintigraphy of a novel ion-sensitive hydrogel based on gellan gum and kappa-carrageenan, *Eur. J. Pharm. Biopharm.* 114 (2017) 317–323. <https://doi.org/10.1016/j.ejpb.2017.01.023>.
- [117] J.L. Mishima, S., Gasset, A., Klyce, S.D., and Baum, Determination of tear volume and tear flow, [Association for Research in Vision and Ophthalmology, etc.], 1966. <https://iovs.arvojournals.org/article.aspx?articleid=2203634> (accessed March 6, 2019).
- [118] K.P. Xu, K. Tsubota, Correlation of tear clearance rate and fluorophotometric assessment of tear turnover, *Br. J. Ophthalmol.* 79 (1995) 1042–1045. <https://doi.org/10.1136/bjo.79.11.1042>.
- [119] J. Li, S. Tian, Q. Tao, Y. Zhao, R. Gui, F. Yang, L. Zang, Y. Chen, Q. Ping, D. Hou, Montmorillonite/chitosan nanoparticles as a novel controlled-release topical ophthalmic delivery system for the treatment of glaucoma., *Int. J. Nanomedicine.* 13 (2018) 3975–3987. <https://doi.org/10.2147/IJN.S162306>.
- [120] R.S. Bhatta, H. Chandasana, Y.S. Chhonker, C. Rathi, D. Kumar, K. Mitra, P.K. Shukla, Mucoadhesive nanoparticles for prolonged ocular delivery of natamycin: In vitro and pharmacokinetics studies, *Int. J. Pharm.* 432 (2012) 105–112. <https://doi.org/10.1016/j.ijpharm.2012.04.060>.
- [121] M. Ijaz, M. Ahmad, N. Akhtar, F. Laffleur, A. Bernkop-Schnürch, Thiolated  $\alpha$ -Cyclodextrin: The Invisible Choice to Prolong Ocular Drug Residence Time, *J. Pharm. Sci.* 105 (2016) 2848–2854.

- <https://doi.org/10.1016/j.xphs.2016.04.021>.
- [122] M. Ijaz, B. Matuszczak, D. Rahmat, A. Mahmood, S. Bonengel, S. Hussain, C.W. Huck, A. Bernkop-Schnürch, Synthesis and characterization of thiolated  $\beta$ -cyclodextrin as a novel mucoadhesive excipient for intra-oral drug delivery, *Carbohydr. Polym.* 132 (2015) 187–195. <https://doi.org/10.1016/j.carbpol.2015.06.073>.
- [123] J.A. Matthews, G.E. Wnek, D.G. Simpson, G.L. Bowlin, Electrospinning of collagen nanofibers, *Biomacromolecules*. (2002). <https://doi.org/10.1021/bm015533u>.
- [124] P. Kiselev, J. Rosell-Llompart, Highly aligned electrospun nanofibers by elimination of the whipping motion, *J. Appl. Polym. Sci.* (2012). <https://doi.org/10.1002/app.36519>.
- [125] A. Theron, E. Zussman, A.L. Yarin, Electrostatic field-assisted alignment of electrospun nanofibres, in: *Nanotechnology*, 2001. <https://doi.org/10.1088/0957-4484/12/3/329>.
- [126] K. Edsman, J. Carlfors, R. Petersson, Rheological evaluation of poloxamer as an in situ gel for ophthalmic use, *Eur. J. Pharm. Sci.* 6 (1998) 105–112. [https://doi.org/10.1016/S0928-0987\(97\)00075-4](https://doi.org/10.1016/S0928-0987(97)00075-4).
- [127] I.D. Rupenthal, C.R. Green, R.G. Alany, Comparison of ion-activated in situ gelling systems for ocular drug delivery. Part 2: Precorneal retention and in vivo pharmacodynamic study, *Int. J. Pharm.* 411 (2011) 78–85. <https://doi.org/10.1016/J.IJPHARM.2011.03.043>.
- [128] Calculation of molecular properties and bioactivity score, (2020). <https://www.molinspiration.com/cgi-bin/properties> (accessed March 23, 2020).
- [129] 2-[7-(3,3-Dimethyl-1-octadecylindol-1-ium-2-yl)hepta-2,4,6-trienylidene]-3,3-dimethyl-1-octadecylindole;iodide | C63H101IN2 - PubChem, (2020). <https://pubchem.ncbi.nlm.nih.gov/compound/74405886#section=Computed-Descriptors> (accessed March 23, 2020).
- [130] Fluorescein sodium (Uranin), (2020). <http://www.chemicaland21.com/specialtychem/finechem/FLUORESCEIN SODIUM.htm> (accessed March 23, 2020).
- [131] Y. Oba, S.R. Poulson, Octanol-water partition coefficients ( $K_{ow}$ ) vs. Ph for fluorescent dye tracers (fluorescein, eosin y), and implications for hydrologic tracer tests, *Geochem. J.* 46 (2012) 517–520. <https://doi.org/10.2343/geochemj.2.0226>.
- [132] H. Park, J.R. Robinson, Mechanisms of Mucoadhesion of Poly(acrylic Acid) Hydrogels, *Pharm. Res. An Off. J. Am. Assoc. Pharm. Sci.* 4 (1987) 457–464. <https://doi.org/10.1023/A:1016467219657>.
- [133] F. Zahir-Jouzani, J.D. Wolf, F. Atyabi, A. Bernkop-Schnürch, In situ gelling and mucoadhesive polymers: why do they need each other?, *Expert Opin. Drug Deliv.* 15 (2018) 1007–1019. <https://doi.org/10.1080/17425247.2018.1517741>.
- [134] T. Schmitz, V. Grabovac, T.F. Palmberger, M.H. Hoffer, A. Bernkop-Schnürch, Synthesis and characterization of a chitosan-N-acetyl cysteine conjugate, *Int. J. Pharm.* 347 (2008) 79–85. <https://doi.org/10.1016/j.ijpharm.2007.06.040>.
- [135] C.E. Kast, A. Bernkop-Schnürch, Thiolated polymers - thiomers: Development and in vitro evaluation of chitosan-thioglycolic acid conjugates, *Biomaterials*. 22 (2001) 2345–2352. [https://doi.org/10.1016/S0142-9612\(00\)00421-X](https://doi.org/10.1016/S0142-9612(00)00421-X).



- [136] V.M. Leitner, G.F. Walker, A. Bernkop-Schnürch, Thiolated polymers: Evidence for the formation of disulphide bonds with mucus glycoproteins, *Eur. J. Pharm. Biopharm.* 56 (2003) 207–214. [https://doi.org/10.1016/S0939-6411\(03\)00061-4](https://doi.org/10.1016/S0939-6411(03)00061-4).
- [137] S. Galindo-Rodriguez, E. Allémann, H. Fessi, E. Doelker, Physicochemical parameters associated with nanoparticle formation in the salting-out, emulsification-diffusion, and nanoprecipitation methods, *Pharm. Res.* 21 (2004) 1428–1439. <https://doi.org/10.1023/B:PHAM.0000036917.75634.be>.
- [138] B. Göttel, H. Lucas, F. Syrowatka, W. Knolle, J. Kuntsche, J. Heinzelmann, A. Viestenz, K. Mäder, In situ Gelling Amphotericin B Nanofibers: A New Option for the Treatment of Keratomycosis, *Front. Bioeng. Biotechnol.* 8 (2020). <https://doi.org/10.3389/fbioe.2020.600384>.
- [139] A.E. Hawley, L. Illum, S.S. Davis, Preparation of biodegradable, surface engineered PLGA nanospheres with enhanced lymphatic drainage and lymph node uptake, *Pharm. Res.* (1997). <https://doi.org/10.1023/A:1012117531448>.
- [140] S.K. Sahoo, J. Panyam, S. Prabha, V. Labhasetwar, Residual polyvinyl alcohol associated with poly (D,L-lactide-co-glycolide) nanoparticles affects their physical properties and cellular uptake, *J. Control. Release.* (2002). [https://doi.org/10.1016/S0168-3659\(02\)00127-X](https://doi.org/10.1016/S0168-3659(02)00127-X).
- [141] L.C.M. Egito, S.R. Batistuzzo De Medeiros, M.G. Medeiros, J.C. Price, E.S.T. Egito, Evaluation of the relationship of the molecular aggregation state of amphotericin B in medium to its genotoxic potential, *J. Pharm. Sci.* 93 (2004) 1557–1565. <https://doi.org/10.1002/jps.20038>.
- [142] C. Ernst, J. Grange, H. Rinnert, G. Dupont, J. Lematre, Structure of amphotericin B aggregates as revealed by UV and CD spectroscopies, *Biopolymers.* 20 (1981) 1575–1588. <https://doi.org/10.1002/bip.1981.360200802>.
- [143] G. Vandermeulen, L. Rouxhet, A. Arien, M.E. Brewster, V. Préat, Encapsulation of amphotericin B in poly(ethylene glycol)-block-poly( $\epsilon$ - caprolactone-co-trimethylenecarbonate) polymeric micelles, *Int. J. Pharm.* 309 (2006) 234–240. <https://doi.org/10.1016/j.ijpharm.2005.11.031>.
- [144] L.L.C. E.R. Squibb & Sons, Fachinformation Fungizone® 50 mg, (n.d.) 1–4. [https://www.google.com/url?sa=t&rct=j&q=&esrc=s&source=web&cd=1&cad=rja&uact=8&ved=2ahUKEwjI87Kao4jpAhVU6uAKHS4-AOQQFjAAegQIARAB&url=https%3A%2F%2Fs3.eu-central-1.amazonaws.com%2Fprod-cerebro-ifap%2Fmedia\\_all%2F63662.pdf&usq=AOvVaw2FdrzQxsB0EloYR5b8NBwU](https://www.google.com/url?sa=t&rct=j&q=&esrc=s&source=web&cd=1&cad=rja&uact=8&ved=2ahUKEwjI87Kao4jpAhVU6uAKHS4-AOQQFjAAegQIARAB&url=https%3A%2F%2Fs3.eu-central-1.amazonaws.com%2Fprod-cerebro-ifap%2Fmedia_all%2F63662.pdf&usq=AOvVaw2FdrzQxsB0EloYR5b8NBwU).
- [145] M.A. Holgado, M. Fernandez-Arevalo, J. Alvarez-Fuentes, I. Caraballo, J.M. Llera, A.M. Rabasco, Physical characterization of carteolol: Eudragit® L binding interaction, *Int. J. Pharm.* (1995). [https://doi.org/10.1016/0378-5173\(94\)00208-M](https://doi.org/10.1016/0378-5173(94)00208-M).
- [146] J. Alvarez-Fuentes, I. Caraballo, A. Boza, J.M. Llera, M.A. Holgado, M. Fernández-Arévalo, Study of a complexation process between naltrexone and Eudragit® L as an oral controlled release system, *Int. J. Pharm.* (1997). [https://doi.org/10.1016/S0378-5173\(96\)04849-1](https://doi.org/10.1016/S0378-5173(96)04849-1).
- [147] R.I. Moustafine, E.B. Margulis, L.F. Sibgatullina, V.A. Kemenova, G. Van den Mooter, Comparative evaluation of interpolyelectrolyte complexes of chitosan with Eudragit® L100 and Eudragit® L100-55 as potential carriers for oral controlled drug delivery, *Eur. J. Pharm. Biopharm.* (2008). <https://doi.org/10.1016/j.ejpb.2008.04.008>.

- [148] R.I. Moustafine, I.M. Zaharov, V.A. Kemenova, Physicochemical characterization and drug release properties of Eudragit® E PO/Eudragit® L 100-55 interpolyelectrolyte complexes, *Eur. J. Pharm. Biopharm.* 63 (2006) 26–36. <https://doi.org/10.1016/j.ejpb.2005.10.005>.
- [149] M. Gagoś, M. Arczewska, Influence of K<sup>+</sup> and Na<sup>+</sup> ions on the aggregation processes of antibiotic amphotericin B: Electronic absorption and FTIR spectroscopic studies, *J. Phys. Chem. B.* (2011). <https://doi.org/10.1021/jp110543g>.
- [150] M. Gagoś, M. Arczewska, Spectroscopic studies of molecular organization of antibiotic amphotericin B in monolayers and dipalmitoylphosphatidylcholine lipid multibilayers, *Biochim. Biophys. Acta - Biomembr.* (2010). <https://doi.org/10.1016/j.bbamem.2010.07.037>.
- [151] Evonik Industries AG, Specification and test methods of EUDRAGIT L 100 and EUDRAGIT S 100, (2012) 1–7.
- [152] J.A. Rizzo, A.K. Martini, K.A. Pruskowski, M.P. Rowan, K.L. Niece, K.S. Akers, Thermal stability of mafenide and amphotericin B topical solution, *Burns.* 44 (2018) 475–480. <https://doi.org/10.1016/J.BURNS.2017.08.019>.
- [153] A. Manosroi, L. Kongkaneramt, J. Manosroi, Stability and transdermal absorption of topical amphotericin B liposome formulations, *Int. J. Pharm.* (2004). <https://doi.org/10.1016/j.ijpharm.2003.10.031>.
- [154] A.C.F. Rumondor, L.A. Stanford, L.S. Taylor, Effects of polymer type and storage relative humidity on the kinetics of felodipine crystallization from amorphous solid dispersions, *Pharm. Res.* (2009). <https://doi.org/10.1007/s11095-009-9974-3>.
- [155] S. Torrado, S. Torrado, J.J. Torrado, R. Cadórniga, Preparation, dissolution and characterization of albendazole solid dispersions, *Int. J. Pharm.* (1996). [https://doi.org/10.1016/0378-5173\(96\)04586-3](https://doi.org/10.1016/0378-5173(96)04586-3).
- [156] Y.T. Kim, B.K. Shin, V.K. Garripelli, J.K. Kim, E. Davaa, S. Jo, J.S. Park, A thermosensitive vaginal gel formulation with HP $\gamma$ CD for the pH-dependent release and solubilization of amphotericin B, *Eur. J. Pharm. Sci.* 41 (2010) 399–406. <https://doi.org/10.1016/j.ejps.2010.07.009>.
- [157] S.H. Auda, M.M. Ahmed, S. Abd El-Rasoul, K.I. Saleh, Formulation and physicochemical characterization of piroxicam containing polymer films, *Bull. Pharm. Sci.* (2010).
- [158] S.Y.K. Fong, A. Ibisogly, A. Bauer-Brandl, Solubility enhancement of BCS Class II drug by solid phospholipid dispersions: Spray drying versus freeze-drying, *Int. J. Pharm.* 496 (2015) 382–391. <https://doi.org/10.1016/j.ijpharm.2015.10.029>.
- [159] S. Ghosh, S. Das, A.K. De, N. Kar, T. Bera, Amphotericin B-loaded mannose modified poly(d, l-lactide-co-glycolide) polymeric nanoparticles for the treatment of visceral leishmaniasis: in vitro and in vivo approaches, *RSC Adv.* 7 (2017) 29575–29590. <https://doi.org/10.1039/C7RA04951J>.
- [160] P.K. Angra, C. Oettinger, S. Balakrishna Pai, M.J. D'Souza, Amphotericin B microspheres: A therapeutic approach to minimize toxicity while maintaining antifungal efficacy, *J. Microencapsul.* (2009). <https://doi.org/10.3109/02652040902797516>.
- [161] K. Florey, N.W. Atwater, G.A.B. J, J.P. Comer, S.A. Fusari, B.C. Rudy, B.Z. Senkowski, *Analytical Profiles of Drug Substances, Volume 6*, Academic Press Inc London, London, 1977. [https://doi.org/10.1016/s0099-5428\(08\)60725-x](https://doi.org/10.1016/s0099-5428(08)60725-x).
- [162] F.L. Mota, A.P. Carneiro, A.J. Queimada, S.P. Pinho, E.A. Macedo, Temperature and solvent effects

- in the solubility of some pharmaceutical compounds: Measurements and modeling, *Eur. J. Pharm. Sci.* 37 (2009) 499–507. <https://doi.org/10.1016/j.ejps.2009.04.009>.
- [163] C.Y. Wu, L.Z. Benet, Predicting drug disposition via application of BCS: Transport/absorption/elimination interplay and development of a biopharmaceutics drug disposition classification system, *Pharm. Res.* 22 (2005) 11–23. <https://doi.org/10.1007/s11095-004-9004-4>.
- [164] R. Ghadi, N. Dand, BCS class IV drugs: Highly notorious candidates for formulation development, *J. Control. Release.* 248 (2017) 71–95. <https://doi.org/10.1016/j.jconrel.2017.01.014>.
- [165] T. Bourcier, O. Touzeau, F. Thomas, C. Chaumeil, M. Baudrimont, V. Borderie, L. Laroche, Candida Parapsilosis keratitis, *Cornea.* (2003). <https://doi.org/10.1097/00003226-200301000-00012>.
- [166] D. Díaz-Valle, J.M.B. Del Castillo, E. Amor, N. Toledano, M.M. Carretero, T. Díaz-Valle, Severe keratomycosis secondary to *Scedosporium apiospermum*, *Cornea.* (2002). <https://doi.org/10.1097/00003226-200207000-00015>.
- [167] P.A. Thomas, Fungal infections of the cornea, *Eye.* (2003). <https://doi.org/10.1038/sj.eye.6700557>.
- [168] R.A. Mahdy, W.M. Nada, M.M. Wageh, Topical amphotericin B and subconjunctival injection of fluconazole (Combination Therapy) versus topical amphotericin B (Monotherapy) in treatment of keratomycosis, *J. Ocul. Pharmacol. Ther.* (2010). <https://doi.org/10.1089/jop.2010.0005>.
- [169] J.S. Dangi, S.P. Vyas, V.K. Dixit, Effect of Various Lipid-Bile Salt Mixed Micelles on the Intestinal Absorption of Amphotericin-B in Rat, *Drug Dev. Ind. Pharm.* 24 (1998) 631–635. <https://doi.org/10.3109/03639049809082364>.
- [170] P. Furrer, J.M. Mayer, B. Plazonnet, R. Gurny, Ocular tolerance of absorption enhancers in ophthalmic preparations, *AAPS PharmSci.* (2003). <https://doi.org/10.1208/ps040102>.
- [171] P. Furrer, B. Plazonnet, J.M. Mayer, R. Gurny, Application of in vivo confocal microscopy to the objective evaluation of ocular irritation induced by surfactants, *Int. J. Pharm.* (2000). [https://doi.org/10.1016/S0378-5173\(00\)00540-8](https://doi.org/10.1016/S0378-5173(00)00540-8).
- [172] S.E. Marshall, B.A. Marples, W.G. Salt, R.J. Stretton, Aspects of the effect of bile salts on candida albicans, *Med. Mycol.* (1987). <https://doi.org/10.1080/02681218780000351>.
- [173] W.E. Hennink, O. Franssen, W.N.E. Van Dijk-Wolthuis, H. Talsma, Dextran hydrogels for the controlled release of proteins, *J. Control. Release.* 48 (1997) 107–114. [https://doi.org/10.1016/S0168-3659\(97\)00047-3](https://doi.org/10.1016/S0168-3659(97)00047-3).
- [174] A. Das, S. Wadhwa, A.K. Srivastava, Cross-Linked Guar Gum Hydrogel Discs for Colon-Specific Delivery of Ibuprofen: Formulation and In Vitro Evaluation, *Drug Deliv.* 13 (2006) 139–142. <https://doi.org/10.1080/10717540500313455>.
- [175] Europäisches Arzneibuch 8.8, (n.d.). [http://dlib.bibliothek.uni-halle.de:8082/Xaver/start.xav?startbk=PhEUR\\_8\\_D&bk=PhEUR\\_8\\_D&SID=Anonymous5913456524&skin=div&startSkin=div#\\_PhEUR\\_8\\_D\\_%2F%2F%\\*5B%40attr\\_id%3D%27numtext-5.01.01.00%27%5D\\_\\_1591345654805](http://dlib.bibliothek.uni-halle.de:8082/Xaver/start.xav?startbk=PhEUR_8_D&bk=PhEUR_8_D&SID=Anonymous5913456524&skin=div&startSkin=div#_PhEUR_8_D_%2F%2F%*5B%40attr_id%3D%27numtext-5.01.01.00%27%5D__1591345654805) (accessed June 5, 2020).
- [176] Q. Xiao, L.T. Lim, Q. Tong, Properties of pullulan-based blend films as affected by alginate content and relative humidity, *Carbohydr. Polym.* (2012). <https://doi.org/10.1016/j.carbpol.2011.07.040>.
- [177] V. Bhat, H.R. Shivakumar, K.S. Rai, G. Sanjeev, Effect of electron beam irradiation on physico-chemical properties of pullulan, *J. Radioanal. Nucl. Chem.* 293 (2012) 431–435.

- <https://doi.org/10.1007/s10967-012-1691-4>.
- [178] J.S.C. Loo, C.P. Ooi, F.Y.C. Boey, Degradation of poly(lactide-co-glycolide) (PLGA) and poly(L-lactide) (PLLA) by electron beam radiation, *Biomaterials*. 26 (2005) 1359–1367.  
<https://doi.org/10.1016/j.biomaterials.2004.05.001>.
- [179] A.T. Fintzou, M.G. Kontominas, A. V. Badeka, M.R. Stahl, K.A. Riganakos, Effect of electron-beam and gamma-irradiation on physicochemical and mechanical properties of polypropylene syringes as a function of irradiation dose: Study under vacuum, *Radiat. Phys. Chem.* 76 (2007) 1147–1155.  
<https://doi.org/10.1016/j.radphyschem.2006.11.009>.
- [180] A. Fernández-Carballido, P. Puebla, R. Herrero-Vanrell, P. Pastoriza, Radiosterilisation of indomethacin PLGA/PEG-derivative microspheres: Protective effects of low temperature during gamma-irradiation, *Int. J. Pharm.* 313 (2006) 129–135.  
<https://doi.org/10.1016/j.ijpharm.2006.01.034>.
- [181] G. Abuhanoglu, A.Y. Özer, Radiation effects on pharmaceuticals, *Fabad J. Pharm. Sci.* (2010).
- [182] A.H.A. Mohamed-Ahmed, K.A. Les, K. Seifert, S.L. Croft, S. Brocchini, Noncovalent complexation of amphotericin-B with poly( $\alpha$ -glutamic acid), *Mol. Pharm.* (2013).  
<https://doi.org/10.1021/mp300339p>.
- [183] J. Roberts, J. Bingham, A.C. McLaren, R. McLemore, Liposomal Formulation Decreases Toxicity of Amphotericin B In Vitro and In Vivo, *Clin. Orthop. Relat. Res.* 473 (2015) 2262–2269.  
<https://doi.org/10.1007/s11999-015-4232-y>.
- [184] F.A. Maulvi, D.H. Lakdawala, A.A. Shaikh, A.R. Desai, H.H. Choksi, R.J. Vaidya, K.M. Ranch, A.R. Koli, B.A. Vyas, D.O. Shah, In vitro and in vivo evaluation of novel implantation technology in hydrogel contact lenses for controlled drug delivery, *J. Control. Release*. 226 (2016) 47–56.  
<https://doi.org/10.1016/j.jconrel.2016.02.012>.
- [185] O. Galvin, A. Srivastava, O. Carroll, R. Kulkarni, S. Dykes, S. Vickers, K. Dickinson, A.L. Reynolds, C. Kilty, G. Redmond, R. Jones, S. Cheetham, A. Pandit, B.N. Kennedy, A sustained release formulation of novel quininib-hyaluronan microneedles inhibits angiogenesis and retinal vascular permeability in vivo, *J. Control. Release*. 233 (2016) 198–207.  
<https://doi.org/10.1016/j.jconrel.2016.04.004>.
- [186] Fluorescein Alcon® 10 % Injektionslösung | Gelbe Liste, (n.d.). [https://www.gelbe-liste.de/produkte/Fluorescein-Alcon-10-Injektionsloesung\\_38](https://www.gelbe-liste.de/produkte/Fluorescein-Alcon-10-Injektionsloesung_38) (accessed June 30, 2020).
- [187] U.E. Illangakoon, H. Gill, G.C. Shearman, M. Parhizkar, S. Mahalingam, N.P. Chatterton, G.R. Williams, Fast dissolving paracetamol/caffeine nanofibers prepared by electrospinning, *Int. J. Pharm.* 477 (2014) 369–379. <https://doi.org/10.1016/j.ijpharm.2014.10.036>.
- [188] P.L. Destruel, N. Zeng, J. Seguin, S. Douat, F. Rosa, F. Brignole-Baudouin, S. Dufay, A. Dufay-Wojcicki, M. Maury, N. Mignet, V. Boudy, Novel in situ gelling ophthalmic drug delivery system based on gellan gum and hydroxyethylcellulose: Innovative rheological characterization, in vitro and in vivo evidence of a sustained precorneal retention time, *Int. J. Pharm.* 574 (2020) 118734.  
<https://doi.org/10.1016/j.ijpharm.2019.118734>.
- [189] A.J. Morgan, J. Harper, S.L. Hosking, B. Gilmartin, The effect of corneal thickness and corneal curvature on pneumatonometer measurements, *Curr. Eye Res.* (2002).

- <https://doi.org/10.1076/ceyr.25.2.107.10162>.
- [190] L.G. Carney, T.F. Mauger, R.M. Hill, Buffering in human tears: pH responses to acid and base challenge, *Investig. Ophthalmol. Vis. Sci.* (1989).
- [191] M. Yamada, H. Mochizuki, M. Kawai, M. Yoshino, Y. Mashima, Fluorophotometric measurement of pH of human tears in vivo, *Curr. Eye Res.* (1997). <https://doi.org/10.1076/ceyr.16.5.482.7050>.
- [192] F.H. Fischer, M. Wiederholt, Human precorneal tear film pH measured by microelectrodes, *Graefe's Arch. Clin. Exp. Ophthalmol.* (1982). <https://doi.org/10.1007/BF02215658>.
- [193] W.H. Coles, P.A. Jaros, Dynamics of ocular surface pH, *Br. J. Ophthalmol.* (1984). <https://doi.org/10.1136/bjo.68.8.549>.
- [194] V. Filipe, A. Hawe, W. Jiskoot, Critical evaluation of nanoparticle tracking analysis (NTA) by NanoSight for the measurement of nanoparticles and protein aggregates, *Pharm. Res.* (2010). <https://doi.org/10.1007/s11095-010-0073-2>.
- [195] F. Babick, ed., Chapter 3.2.1 - Dynamic light scattering (DLS) | Elsevier Enhanced Reader, in: *Characterisation of Nanoparticles*, Elsevier, 2020: pp. 137–172. <https://doi.org/10.1016/B978-0-12-814182-3.00010-9>.
- [196] P. Hole, K. Sillence, C. Hannell, C.M. Maguire, M. Roesslein, G. Suarez, S. Capracotta, Z. Magdolenova, L. Horev-Azaria, A. Dybowska, L. Cooke, A. Haase, S. Contal, S. Manø, A. Vennemann, J.J. Sauvain, K.C. Staunton, S. Anguissola, A. Luch, M. Dusinska, R. Korenstein, A.C. Gutleb, M. Wiemann, A. Prina-Mello, M. Riediker, P. Wick, Interlaboratory comparison of size measurements on nanoparticles using nanoparticle tracking analysis (NTA), *J. Nanoparticle Res.* (2013). <https://doi.org/10.1007/s11051-013-2101-8>.
- [197] B.H. Zimm, The scattering of light and the radial distribution function of high polymer solutions, *J. Chem. Phys.* 16 (1948) 1093–1099. <https://doi.org/10.1063/1.1746738>.
- [198] E. Folta-Stogniew, K.R. Williams, Determination of molecular masses of proteins in solution: Implementation of an HPLC size exclusion chromatography and laser light scattering service in a core laboratory, *J. Biomol. Tech.* (1999).
- [199] R.C. Borra, M.A. Lotufo, S.M. Gagiotti, F. de M. Barros, P.M. Andrade, A simple method to measure cell viability in proliferation and cytotoxicity assays, *Braz. Oral Res.* (2009). <https://doi.org/10.1590/S1806-83242009000300006>.
- [200] G. Leonaviciute, W. Suchaoin, B. Matuszczak, H.T. Lam, A. Mahmood, A. Bernkop-Schnürch, Preactivated thiolated pullulan as a versatile excipient for mucosal drug targeting, *Carbohydr. Polym.* 151 (2016) 743–751. <https://doi.org/10.1016/j.carbpol.2016.06.005>.
- [201] D.F.S. Fonseca, P.C. Costa, I.F. Almeida, P. Dias-Pereira, I. Correia-Sá, V. Bastos, H. Oliveira, M. Duarte-Araújo, M. Morato, C. Vilela, A.J.D. Silvestre, C.S.R. Freire, Pullulan microneedle patches for the efficient transdermal administration of insulin envisioning diabetes treatment, *Carbohydr. Polym.* 241 (2020) 116314. <https://doi.org/10.1016/j.carbpol.2020.116314>.
- [202] P.-L. Destruel, N. Zeng, F. Brignole-Baudouin, S. Douat, J. Seguin, E. Olivier, M. Dutot, P. Rat, S. Dufay, A. Dufay-Wojcicki, M. Maury, N. Mignet, V. Boudy, In Situ Gelling Ophthalmic Drug Delivery System for the Optimization of Diagnostic and Preoperative Mydriasis: In Vitro Drug Release, Cytotoxicity and Mydriasis Pharmacodynamics, *Pharmaceutics.* 12 (2020) 360.

- <https://doi.org/10.3390/pharmaceutics12040360>.
- [203] A. Fernández-Ferreiro, M. González Barcia, M. Gil-Martínez, A. Vieites-Prado, I. Lema, B. Argibay, J. Blanco Méndez, M.J. Lamas, F.J. Otero-Espinar, In vitro and in vivo ocular safety and eye surface permanence determination by direct and Magnetic Resonance Imaging of ion-sensitive hydrogels based on gellan gum and kappa-carrageenan, *Eur. J. Pharm. Biopharm.* 94 (2015) 342–351.  
<https://doi.org/10.1016/j.ejpb.2015.06.003>.

---

## Appendices

<b>Appendix 1</b>	<b>Supplementary Material .....</b>	<b>XXIII</b>
<b>Appendix 2</b>	<b>Dataset .....</b>	<b>XXIV</b>
<b>Appendix 3</b>	<b>Amplitude sweep of electrospun nanofibers .....</b>	<b>XXV</b>
<b>Appendix 4</b>	<b>Nano-CT: Measurement parameters and data processing .....</b>	<b>XXVI</b>
<b>Appendix 5</b>	<b>Nanoparticle Tracking Analysis: Theoretical background .....</b>	<b>XXVII</b>
<b>Appendix 6</b>	<b>Flow-field-flow fractionation: Theoretical Background .....</b>	<b>XXVIII</b>
<b>Appendix 7</b>	<b>Resazurin reduction assay .....</b>	<b>XXIX</b>

## Appendix 1 Supplementary Material

**Table 10.** *Composition of used buffer solutions and different cell culture media.*

<b>Buffer/Medium</b>	<b>Ingredient</b>	<b>Amount</b>
Simulated tear fluid pH 7.4 (STF)	NaCl	0.68 g
	NaHCO <sub>3</sub>	2.2 g
	CaCl*H <sub>2</sub> O	0.084 g
	KCl	1.4 g
	NaN <sub>3</sub>	0.2 g
	H <sub>2</sub> O	1000 g
Phosphate buffer pH 7.4 (PBS)	NaH <sub>2</sub> PO <sub>4</sub>	2.38 g
	KH <sub>2</sub> PO <sub>4</sub>	0.19 g
	NaCl	8 g
	NaN <sub>3</sub>	0.2 g
	H <sub>2</sub> O	1000 g
Cell culture medium NHDF	FCS	9.64 % (v/v)
	DMEM	86.80 % (v/v)
	Penicillin-Streptomycin	0.96 % (v/v)
	L-Glutamine solution	1.77 % (v/v)
Cell culture medium 3T3	FCS	9.55 % (v/v)
	DMEM	87.63 % (v/v)
	Penicillin-Streptomycin	0.95 % (v/v)
	L-Glutamine solution	1.75 % (v/v)
	Sodium pyruvate solution	0.95 % (v/v)
Universal medium for yeasts	Yeast extract	3 g
	Malt extract	3 g
	Peptone from soybeans	5 g
	Glucose	10 g
	(Agar)	15 g
	Double distilled Water	1000 g



## Appendix 2 Dataset

**Table 11.** *Different compositions of polymer solutions for electrospinning in double distilled water with the obtained product and process stability (GG = Gellan Gum LA, PL = Pullulan).*

Number	GG % [m/v]	PL % [m/v]	Product	Process
1	0.1	-	Droplets	Unstable
2	0.2	-	Droplets	Unstable
3	0.4	-	Droplets	Unstable
4	0.6	-	Droplets	Unstable
5	0.3	20	Fibers	Unstable
6	-	1	Droplets	Stable
7	-	2	Droplets	Stable
8	-	3	Droplets	Stable
9	-	4	Droplets	Stable
10	-	8	Droplets	Stable
11	-	10	Beaded Fibers	Stable
12	-	12.5	Beaded Fibers	Stable
13	-	17.5	Fibers	Stable
14	-	20	Fibers	Stable
15	-	22.5	Fibers	Stable
16	0.4	10	Fibers	Unstable
17	0.6	10	Fibers	Unstable
18	0.7	10	Fibers	Unstable
19	0.7	12	Fibers	Unstable
20	0.7	14	Fibers	Unstable
21	0.225	15	Fibers	Stable
22	0.225	17.5	Fibers	Stable
23	0.225	20	Fibers	Stable
24	0.225	22.5	Fibers	Stable

### Appendix 3 Amplitude sweep of electrospun nanofibers

Similar sample amounts and buffer volumes were used for amplitude sweep as well for the frequency sweep investigation. Before the frequency sweep was performed, the LVR was determined by an amplitude sweep. During the LVR, storage modulus  $G'$  and loss modulus  $G''$  are independent from the applied deformation. The LVR had to be determined to ensure the sample integrity during the applied deformation. Therefore, an amplitude sweep was carried out previous. The amplitude sweep was carried out with a frequency of 1 Hz and a deformation of 0.01-100 % at 34 °C. Figure 51 displays the data of the performed amplitude sweep.

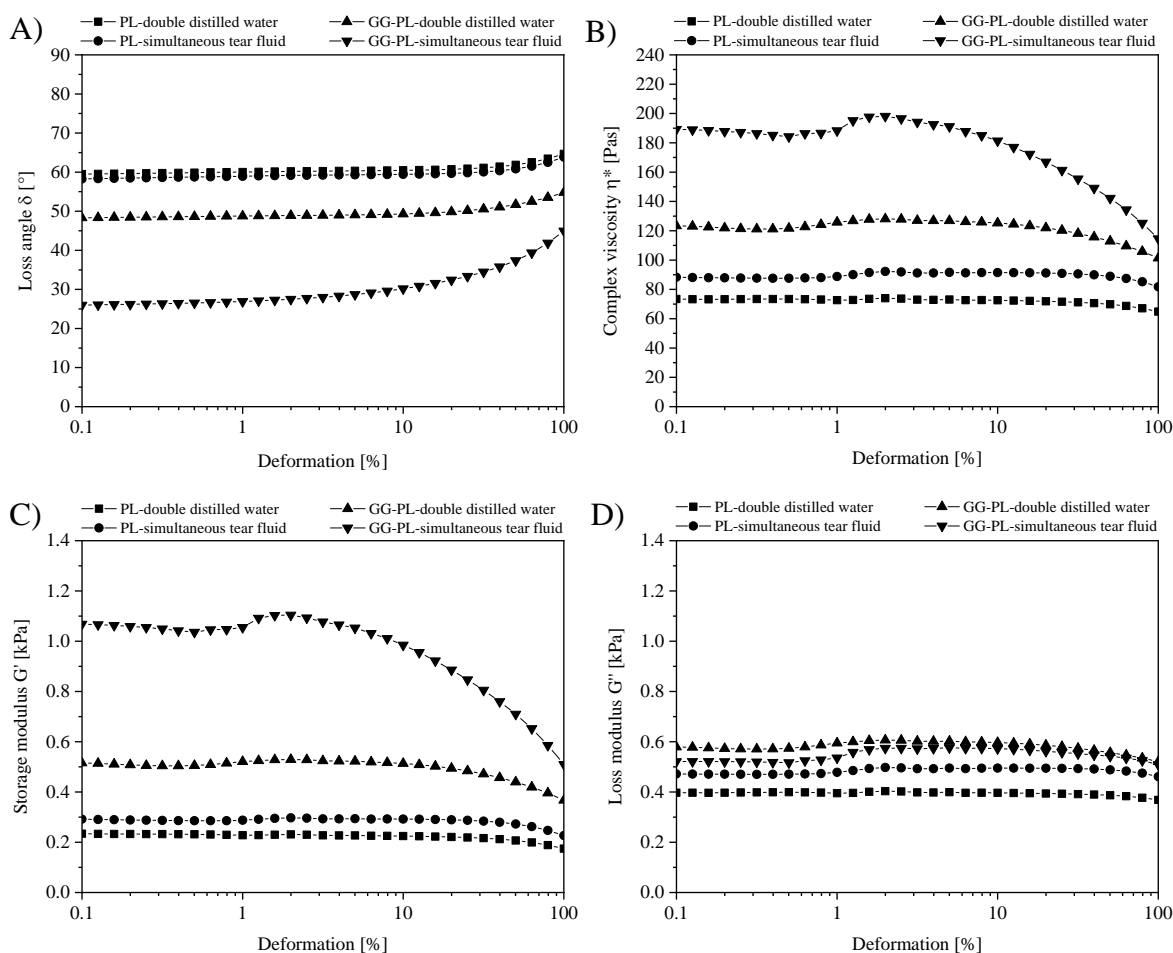


**Figure 51.** Amplitude sweep of pure Pullulan and 1 % Gellan Gum blended fibers in double distilled water and STF at 34 °C: A) Loss angle  $\delta$ ; B) Complex viscosity  $\eta^*$ ; C) Storage modulus  $G'$ ; D) Loss modulus  $G''$  ( $n = 3$ ).

Figure 51 C) and D) displays, that pure Pullulan fibers hydrated with STF and double distilled water, which showed no difference in  $G'$  and  $G''$  during deformation. In contrast to

pure Pullulan, the Gellan Gum containing fibers hydrated with STF showed an rise of  $G'$  to 1.09 kPa at 0.1 % deformation. At a deformation of 1 %,  $G'$  started slightly increasing, followed by strong decrease at 5 % deformation. Gel destruction takes places at deformation  $> 1$  %. Therefore, the following frequency experiments were carried out at 0.4 % deformation, which is appropriate to ensure gel structure integrity. The loss angle  $\delta$  in Figure 51 A) attracts attention as well, because pure Pullulan fibers are characterized with and without cations by a loss angle  $\delta$  of  $60^\circ$  caused by higher amounts of plastic components. The Gellan Gum blended fibers showed a loss angle  $\delta$  decrease from  $48^\circ$  in double distilled water to  $25^\circ$  at lower deformation with STF, which correlates with a rise of the elastic properties after cation addition.

#### **Appendix 4 Nano-CT: Measurement parameters and data processing**

Nanoscale 3D x-ray imaging was used to determine the fiber porosity, surface area, diameter distribution and alignment. Therefore, fibers with 1 % (w/w) Gellan Gum content were cut into  $1 \text{ mm}^2$  slices, followed by gluing the slices onto the tip of a metallic pin. The mounted sample was placed into a sample holder of the x-ray microscope [73]. All experiments were performed by a Carl Zeiss Xradia 810 Ultra x-ray microscope (Carl Zeiss Microscopy GmbH, Jena, Germany) with a chromium source (5.4 keV). The experiments were performed with 901 projections over  $180^\circ$ , with an exposure time of 15 s per projection with a detector binning of 1 and voxel size of 64 nm in the final images. Image reconstruction was performed by filtered back-projection algorithm using the XMReconstructor software integrated into the Xradia 810 Ultra, and the three-dimensional images were exported as a stack of tiff images. The XY stack images were corrected using Thermo Scientific Avizo (version 9.4.0). The images were filtered using iterative median filter with 5 iterations, followed by filtering with a windowed non-local means filter. The filtered datasets were segmented using interactive threshold module. The threshold selection was evaluated through all slices to ensure the selection of all fibers, while keeping the image noise at a minimum. Island removal was performed in order to remove small, detached segments of fibers and the remaining background noise. The specific surface area was calculated by the ratio of the estimated surface area of the fiber and the volume occupied by it using the Avizo module Object Specific Surface. Porosity of the fibers was calculated by comparing the

volume occupied by voxels attributed to empty space with the total number of voxels in the dataset. A volumetric dataset of 727x502x1020 voxels was used in this case. For the fiber diameter measurements, the “Auto Skeleton” module in Avizo was used. It allows to create a skeleton of the fiber network and to attribute thickness values for each point along the skeleton corresponding to the distance between this line and the border of the fibers. This value multiplied by two corresponds, then, to the fiber diameter. Only diameters equal to or above 4 voxels in size were considered in the fiber diameter calculations [73].

### Appendix 5 Nanoparticle Tracking Analysis: Theoretical background

NTA allows in contrast to PCS the particle size measurement by tracking the Brownian motion of every single particle in a defined time with a reduced proportional weighting. Therefore, a laser with a defined wavelength crosses the particle suspension and the resulting scatter patterns of each particle are visualized by microscopy with a charge-coupled device (CCD) camera [194]. NTA is suitable to investigate bi-or multimodal particle size distributions in more detail compared to PCS [194]. During NTA measurements, the moved distance of each individual particle over a defined period is recorded and used for calculation of the hydrodynamic radius  $r_h$ . PCS uses the Stokes-Einstein-equation (Equation 6) for calculation of the hydrodynamic radius by the light scattering fluctuation [195]. NTA is able to determine the particle movement in x- and y-direction by camera visualization, but the Brownian motion is a three dimensional phenomena [196]. Hence, the mathematic model was modified from three dimensional to a two dimensional model (Equation 7).

**Equation 6**

$$D = \frac{k_B T}{6\pi r_h \eta}$$

**Equation 7**

$$\overline{(x,y)^2} = \frac{2k_B T t}{3r_h \eta}$$

D	Diffusion constant
$k_B$	Boltzmann constant
T	Temperature
t	Time

$\eta$	Dynamic viscosity of the dispersion medium
$r_h$	Hydrodynamic radius
$\overline{(x, y)^2}$	Mean-squared speed of a particle

## Appendix 6 Flow-field-flow fractionation: Theoretical Background

The theoretical background of the molecular weight determination via A4F is described in the following section. Zimm described the scattering of light and radial distribution function of polymer solutions [197]:

**Equation 8** 
$$\frac{K * c}{R(\theta)} = \frac{1}{M_w * P(\theta)} + 2A_2c$$

$R(\theta)$	Rayleigh Ratio (Excess intensity of scattered light at DAWN angle $\theta$ (= angular dependence of scattered light) [ $\text{cm}^{-1}$ ])
$c$	Mass concentration [g/ml]
$M_w$	Weight-average molecular weight [g/mol]
$P(\theta)$	Theoretically derived form factor
$A_2$	Second virale coefficient (negligible for low concentrated solutions $A_2=0$ ) [ml* $\text{mol}/\text{g}^2$ ]
$K$	Optical parameter equal to $4\pi^2n^2(\text{dn}/\text{dc})^2/(\lambda_0^4N_A)$
$n$	Solvent refractive index $\text{dn}/\text{dc}$ refractive index increment (characterizes the change of the refractive index $n$ with the concentration)
$N_A$	Avogadro constant
$\lambda_0$	Wavelength of scattered light in vacuum [cm]

For low concentrated solutions, the second viral condition term  $2A_2c$  can be neglected. Note that as  $\theta$  approaches zero, the form factor  $P(\theta)$  approaches unity. Therefore, Equation 8 simplifies to:

**Equation 9** 
$$\frac{K * c}{R(\theta)} = \frac{1}{M_w}$$

The Debye fitting model was used for determination of the Pullulan molecular weight. Within a plot of  $\frac{R(\theta)}{K*c}$  against  $\sin^2\left(\frac{\theta}{2}\right)$  and fitting a polynomial fit in  $\sin^2\left(\frac{\theta}{2}\right)$  to the data. The molecular weight can be determined from the y-intercept [198]. Instead, Gellan Gum

LA was analyzed by the Random Coil method. Therefore, it is necessary that a theoretical form factor  $P(\theta)$  for random coils was inserted into Equation 8. In Equation 10 the form factor is defined. For calculation, we assumed that the polymers are approximately random coils. Followed by an iterative nonlinear least square fit [198].

**Equation 10**

$$P(\theta) = \frac{2}{u^2} (e^{-u} - 1 + u)$$

$$u = \left(\frac{4\pi}{\lambda}\right)^2 \langle r^2 \rangle \sin^2 \left(\frac{\theta}{2}\right)$$

r Radius

## Appendix 7 Resazurin reduction assay

The resazurin reduction assay is an effective, reliable method to characterize the cytotoxic effect of medical devices and substances on different cell lines *in vitro*. Based on the electron transfer from  $\text{NADPH} + \text{H}^+$  to resazurin and resorufin is formed [199]. The amount of reduced resazurin is used to correlate the number of metabolically active cells. After defined incubation times, the reduced resorufin concentration is quantified by fluorescence. In Figure 52, the biological transformation of resazurin to resorufin with the corresponding properties of the substrates is illustrated.

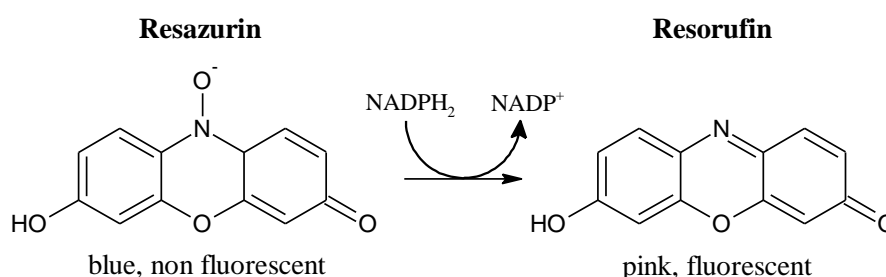


**Figure 52.** Biological transformation of resazurin to resorufin under influence of viable cells.

Normal human dermal fibroblasts (NHDF, human fibroblasts) and "3-day transfer, inoculum  $3 \times 10^5$  cells" (3T3, mice fibroblasts) cell lines were used for the cytotoxic experiments *in vitro*. 120000 NHDF and 60000 3T3 cells were placed in 24 well plates and grew for 24 h at  $37^\circ\text{C}$  and 5 %  $\text{CO}_2$  (Heracell 150  $\text{CO}_2$  Incubator, Heraeus Holding GmbH, Hanau, Germany) in 500  $\mu\text{l}$  of appropriate cell culture media. Different amounts of Pullulan-Gellan Gum fibers were placed into the well plates to ensure a concentration of 1, 10 and 100 mg/ml of fibers. After incubation for 4 and 24 h, 150  $\mu\text{l}$  Resazurin solution (0.015 mg/ml in PBS)

was added to each well, followed by re-incubation for 2 h. Afterwards, the well plates were analyzed by Cytation™ 5 imaging reader (BioTek Instruments, Bad Friedrichshall, Germany) using the RFP 531(excitation)/593(emission) filter set. The cell viability was determined using Equation 11.

**Equation 11**

$$\text{Cell viability [\%]} = \frac{Em_S - Em_{BG}}{Em_{un} - Em_{BG}} * 100\%$$

$Em_s$  = Emission Sample

$Em_{BG}$  = Emission Background

$Em_{un}$  = Emission untreated cells

The cellular tolerance of formulated drug delivery systems had to be ensured to maintain a safe therapy for the patients. It is well known that different cell lines show different reactions after treatment with the similar samples. Hence, NHDF and 3T3 cells were used during the described experiments. In Figure 53 the results of the resazurin assay of the drug free Pullulan-Gellan Gum fibers are displayed. They were incubated over a period of 24 h. Both cell lines showed neither after 4 h nor after 24 h a cytotoxic effect of the instilled fibers from 1 mg/ml to 10 mg/ml. The cell viability was 100 %, but after increasing the fiber concentration to 100 mg/ml, a decrease of the viability was obtained. The NHDF cells showed after 4 h 60 % and after 24 h 50 % cell viability. The 3T3 cells showed after 4 h 57 % and after 24 h 30 % viability. One reason could be the cytotoxic effect of the fibers at a concentration of 100 mg/ml, but furthermore induce the high amount of fiber material gel formation inside the well plates. The gels are visible as microscopic images in Figure 53. The images of the treated cells show dark spots in the wells. These spots are caused by the fiber formed gel with cell media contact. These gel-spots prevent the necessary spectral absorption and emission of the formed resorufin. Hence, the results have to be discussed critical. Furthermore, the fluorescence quantification depends on the optical path length of the fluid. By addition of larger amounts of gelling agent, the liquid level in the well plates changed. As consequence, exact quantification at higher gel concentrations was difficult. In addition to the spectral challenges, the formed gel decelerates the diffusion velocity inside the cellular media. Therefore, the diffusion of the nutritive ingredients for the cells is slowed and thereby the cell growth is inhibited. Another reason could be that the gravity forces of the gel affect the seeded cells and as consequence the cell viability became reduced at 100 mg/ml.

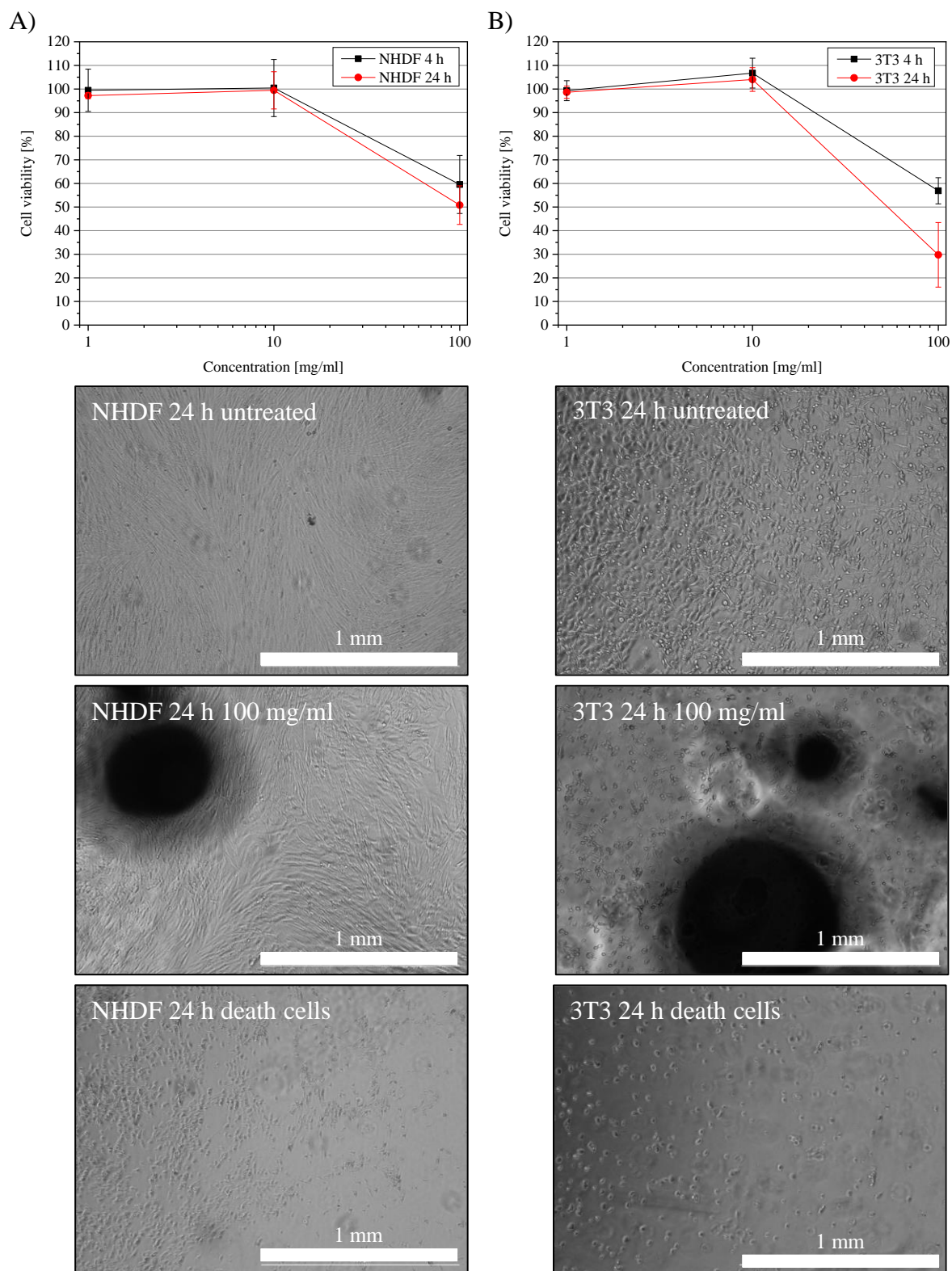


**Figure 53.** Resazurin assay of the electrospun Pullulan-Gellan Gum fibers of NHDF (A) and 3T3 (B) cells after 4 h and 24 h incubation ( $n = 3 \pm SD$ ). Microscopic images of death cells, untreated cells and after gel incubation for 24 h.



Hence, the microscopic images in Figure 53 were shown to gain information about the microscopic cell appearance. The images show untreated viable cells as well as treated cells with 100 mg/ml after 24 h sample of each cell type. The untreated NHDF cells had a smooth stretched appearance and no differences in comparison to the treated cells were shown. The 3T3 cells treated with sample showed instead larger regions without cells what gave reason to expect that more cells underlie apoptosis under the Pullulan-Gellan Gum induced stress. These results indicate that the NHDF cells were more resistant against the electrospun fibers at a higher concentration. In contrast the 3T3 cells suppose more cytotoxic behavior triggered by the fibers. The concentration of 100 mg/ml was investigated, because *in vivo* a concentration of 4000 mg/ml would be achieved after application of a 4 mg lens. The resulting *in vivo* concentrations cannot be investigated during the resazurin assay, therefore other cytotoxicity models have to be used. Pullulan as spinning copolymer is well known as non-toxic and non-mutagenic ingredient [54,200]. In the literature, no significant effect of Pullulan as a microneedle formulation against non-tumorigenic immortalized human keratinocytes (HaCT) was discussed [201]. Next to Pullulan, the fibers contain 1 % Gellan Gum. Gellan Gum is common for its good cellular compatibility and is used in conventional eye drops. Furthermore, other groups describe that human corneal epithelial cells as well as human keratocytes, which were treated with *in situ* gelling Gellan Gum eye drops showed no reduction of the cellular viability and ensure safe ocular application [202,203].

## Deutsche Zusammenfassung

Das therapeutische Interesse an neuen Arzneistoffträgersystemen zur Anwendung am Auge steigt stetig an, um die Probleme der geringen Bioverfügbarkeit konventioneller Augentropfen zu lösen. Die kurze Verweilzeit flüssiger Zubereitungen am Auge erfordert eine hohe Applikationsfrequenz, um Wirkstoffspiegel im therapeutischen Bereich generieren zu können. Insbesondere die Behandlung von Pilzinfekten am Auge stellt die Medizin vor große Herausforderungen, nicht zuletzt bedingt durch Notwendigkeit der stündlichen Applikation. Gellan Gum, als *in situ* gelierendes Agens, welches bereits als Hilfsstoff in Augentropfen eingesetzt wird, gilt als ein vielversprechender Kandidat die genannten Probleme der konventionellen Ophthalmictherapie zu überwinden.

Zu Beginn der vorliegenden Arbeit wurde das rheologische Verhalten potenzieller Polymerlösungen, bestehend aus Pullulan und Gellan Gum, untersucht um Rückschlüsse auf Viskosität und Spinnbarkeit zu ziehen. Darin wurde beobachtet, dass Gellan Gum in bidestilliertem Wasser ein ausgeprägtes, schwerverflüssigendes Verhalten zeigt. Bedingt durch die anionischen Ladungen des Polymers kommt es unter Scherbeanspruchung zur elektrostatischen Abstoßung der Polymerketten, wodurch die Viskosität sinkt. Durch den Zusatz von Pullulan als Spinn-co-Polymer ist es möglich Gellan Gum via Elektrosinnen zu Fasern zu verarbeiten. 15-20 % Pullulan reichten bereits aus, um erfolgreich 0,225 %-ige Gellan Gum Lösungen zu Fasern zu verarbeiten. Ein größerer Anteil Gellan Gum in der Spinnlösung führte ebenfalls zur Ausbildung von Fasern, ermöglichte jedoch nicht einen störungsfreien Spinnprozess. Die hergestellten Fasern wurden mittels ESEM untersucht und ergaben Faserdurchmesser im mittleren Nanometerbereich. Mit zunehmendem Anteil an Pullulan innerhalb der Spinnlösung war ein Anstieg der Faserdurchmesser zu erkennen. Durch Zusatz von Pullulan war es somit möglich Fasern mit 1 % Gellan Gum herzustellen, ausschließlich diese wurden im Laufe der Arbeit intensiver untersucht.

Die hergestellten Gellan Gum haltigen Fasern zeigten ein für Gele charakteristisches Verhalten innerhalb der oszillationsrheologischen Untersuchungen. Ein Phasenwinkel  $\delta < 45^\circ$  wurde erreicht, als die Fasern mit STF hydratisiert wurden. Wurden die gleichen Experimente mit ionenfreiem, destilliertem Wasser durchgeführt war dies nicht der Fall. Ebenso zeigten die Gellan Gum freien Fasern diese Eigenschaft nicht. Diese wiesen einen Phasenwinkel  $\delta > 45^\circ$  auf und waren somit vom Verhalten viskoelastischer Flüssigkeiten

gekennzeichnet. Zusätzlich zu den rheologischen Untersuchungen wurden NMR Analysen durchgeführt. Dabei wurden sowohl  $T_2$ -Relaxationszeiten, als auch entsprechende Diffusionskoeffizienten bestimmt. Diese korrelierten mit den rheologischen Daten und zeigten eine stärkere Immobilisierung des enthaltenen Wassers innerhalb einer Gelmatrix durch das in die Fasern eingearbeitete Gellan Gum.

Ziel der vorliegenden Arbeit war es u.a. die Geometrie der Arzneiform an die anatomischen Besonderheiten des Auges anzupassen. So wurden die zunächst planaren, elektrogewebten Fasern auf 1,5 cm Durchmesser getrimmt und anschließend mit einer selbstkonstruierten, 3D-gedruckten Matrix aus PLA zu einer Krümmung von 10,92 mm geformt. Das menschliche Auge, im Vergleich zeigt eine Krümmung von 7,10-8,75 mm. Durch Anpassung der Krümmung konnte eine gleichmäßige Benetzung der Augenoberfläche *in vitro* erreicht werden.

Im Laufe der Arbeit wurde ein neues *in vitro* Modell zur Bestimmung der okulären Verweilzeit entwickelt und mittels 3D-Druck hergestellt. Das entworfene Modell, in Kombination mit MFSI, ermöglichte es durch die Verwendung von Schweineaugen *ex vivo* die exakten anatomischen und histologischen Bedingungen des Auges zu simulieren. Das Modell war dazu in der Lage potenzielle Arzneistoffformulierungen bei Raumtemperatur auf Mucoadhäsivität und Verweilzeit, bereits im frühen Stadium der Entwicklung zu untersuchen. Die entwickelten Fasern verlängerten die Verweilzeit um ein Vielfaches im Vergleich zu konventionellen Augentropfen. Zusätzlich wurden PLGA-Nanopartikel in die Fasern eingearbeitet um den Einfluss der dispersen Phase auf die Verweilzeit zu untersuchen. Diese zeigten wiederum eine Verlängerung der Verweilzeit im Vergleich zu den partikelfreien Fasern. Bedingt war dies durch den Verteilungskoeffizienten der unterschiedlichen Farbstoffe Fluoresceinnatrium und DiR. Alle untersuchten Proben zeigten eine gleichmäßige Verteilung auf der Hornhautoberfläche und eine reduzierte Clearance *in vitro*.

Nach umfangreicher physikochemischer Charakterisierung der wirkstofffreien Fasern sollte AmpB in die Fasern eingearbeitet werden. AmpB, als BCS IV Molekül stellt bis heute eine große Herausforderung an die galenische Entwicklung dar, um eine qualitative Formulierung zu gewährleisten. In der vorliegenden Arbeit wurden verschiedene Möglichkeiten aufgezeigt um AmpB in wässrig-gewebte Fasern einzuarbeiten. Dazu wurden u.a. Solubilisierungsmittel wie Natriumcholat zugesetzt, der Wirkstoff in PLGA-Nanopartikel verkapselt sowie ein Polyelektrolytkomplex mit Eu-L gebildet. Die

hergestellten PVA stabilisierten Nanopartikel wurden mittels PCS und NTA untersucht und zeigten einen PDI von 0.05-0.25, sowie z-averages von 130-250 nm und eine neutrale Oberflächenladung. Der hergestellte Polyelektrolytkomplex wurde sowohl mittels UV/Vis-, als auch mit ATR-IR-Spektroskopie untersucht. Dabei wurde sowohl die Verschiebung des Absorptionsmaximums von 405 nm zu 315 nm, als auch die neue Transmissionsbande bei  $1554\text{ cm}^{-1}$  in ATR-IR Untersuchungen beschrieben, welche die Ausbildung des Polyelektrolytkomplexes belegten. Die durchgeführten DSC und Röntgenuntersuchungen zeigten zusätzlich, dass AmpB gebunden in einem Polyelektrolytkomplex vorlag. Dieses Verhalten war dadurch bedingt, dass der Abstand zwischen den AmpB Molekülen vergrößert und dadurch der Wirkstoff an der Ausbildung eines Kristallgitters gehindert wurde.

Zusätzlich zu den wirkstofffreien Fasern wurden die beschriebenen Technologien zur Erhöhung der Löslichkeit von AmpB versponnen und die erhaltenen Fasern mittels ESEM untersucht. Alle Fasern zeigten einen Faserdurchmesser im mittleren Nanometerbereich. Im klinischen Alltag werden Augentropfen im off-label use mit einem Gehalt von 0,5 % AmpB zur Behandlung der Keratomykose eingesetzt. AmpB, versponnen ohne weiteren Solubilisierungszusatz, zeigte einen Beladungsgrad von 0,02 %. Der Zusatz von Natriumcholat ermöglichte eine Erhöhung des Beladungsgrades auf 0,04 %. Die Verarbeitung in PLGA Nanopartikel und das anschließende Elektrosponnen erreichte hingegen eine Beladung von 0,05 %. Lediglich durch die Verarbeitung des Polyelektrolytkomplexes wurden Konzentrationen von 0,68 %, also im therapeutisch relevanten Bereich der klinischen Dosis erreicht. Um die inhibitorische Wirkung der natriumcholat- und der polyelektrolytkomplexbeladenen Fasern auf Pilzerreger zu untersuchen wurde ein Plattendiffusionstest mit *Issatchenkia orientalis* durchgeführt. Darin wurde gezeigt, dass die Menge an AmpB in den Natriumcholatifasern zu gering waren um eine effektive Hemmung des Pilzes zu induzieren. Die komplexbeladenen Fasern hingegen, zeigten eine deutliche Hemmung des mikrobiellen Wachstums, sowie eine ausreichende Effektivität des Wirkstoffs trotz Komplexbildung. In den durchgeführten Zelltoxizitätsuntersuchungen zeigten sowohl die unbeladenen, als auch die komplexbeladenen Fasern eine verringerte Zytotoxizität gegenüber hoch differenzierter Hornhautepithelzellen. Die konventionell eingesetzte AmpB Formulierung (Fungizone®) hingegen war durch ausgeprägte Zytotoxizität gekennzeichnet.

Pullulan und Gellan Gum sind seit Jahrzehnten als non-toxische Hilfsstoffe im Bereich der Pharmazeutischen Technologie bekannt und werden bereits seit vielen Jahren in Fertigarzneimitteln eingesetzt. Diese Tatsache, sowie die Ergebnisse der durchgeführten Toxizitätstests *in vitro* bestätigten das weitere Vorgehen die Verweilzeit von wirkstofffreien Fasern am humanen Auge *in vivo* zu untersuchen. Entsprechende Experimente wurden mit elektrogewebten Fasern ohne Wirkstoff in einer Pilotstudie an gesunden Probanden durchgeführt. Zur Detektion wurde der Farbstoff Fluoresceinnatrium in die Proben eingearbeitet. Die zuvor mittels Elektronenstrahl sterilisierten Linsen wurden mittels OCT und Pentacam<sup>®</sup> untersucht. Es zeigte sich, dass die untersuchten Augentropfen, 5 min nach Applikation, als kaum messbare Mengen auf der Hornhaut detektiert werden konnten. Großteil des eingetropften Farbstoffs akkumulierte unmittelbar nach Applikation in den Wimpern. Die gewebten Linsen zeigten hingegen, dass nach 10-15 min verbleibende Gelbestandteile auf der Hornhaut detektiert werden konnten. Weiterhin verblieb ein Teil als Depot im Bindehautsack. Die Quantifizierung der OCT Aufnahmen zeigten, dass die Linsen unmittelbar nach Applikation eine 5-fach höhere Konzentration auf der Hornhaut aufwiesen als die Augentropfen. Diese Ergebnisse belegten die Überlegenheit des entwickelten Systems. Die durchgeführten *in vivo* Experimente wurden mit der Untersuchung des Einflusses der Proben auf den Augen pH abgeschlossen. Dazu wurde der pH der Tränenflüssigkeit vor und nach Linsenapplikation bestimmt. Die Messungen bestätigten die Thesen, dass die Proben den physiologischen pH-Wert des Auges nicht beeinflussen.

Innerhalb der vorliegenden Arbeit wurden *in situ* gelierende Nanofasern auf Gellan Gum Basis entwickelt und umfassend physikochemisch charakterisiert. Die entwickelten Fasern stellten sich als ein potenzielles System, zur Verbesserung der Therapiemöglichkeiten von Keratomykosen heraus. Der formulierte Polyelektrolytkomplex war in der Lage das Wachstum von Candidaspezies zu hemmen. Dennoch ist die detaillierte Quantifizierung des Hemmungsausmaßes des Komplexes im Vergleich zum unverarbeiteten AmpB sinnvoll, um Auskunft über die IC<sub>50</sub>-Werte zu erhalten. Ebenso ist die Testung an weiteren pathogenen Pilzstämmen zu untersuchen um Aussagen über das Wirkspektrum treffen zu können. Diese Arbeit soll den Grundstein für zukünftige tierexperimentelle und klinische Studien legen, in welchen die Effektivität der wirkstoffbeladenen Fasern, als auch relevante Dosen und Therapieschemata bestimmt werden könnten. Um das entwickelte Produkt bis zur Marktreife voranzutreiben ist die Entwicklung einer geeigneten Primärverpackung

notwendig, welche es ermöglicht die flexiblen Linsen während des Transports mechanisch zu schützen, sie aus der Verpackung zu entnehmen, dabei aber auch die Sterilität der Arzneiform aufrechtzuerhalten. Um die vorliegende Arbeit abzuschließen lässt sich sagen, dass das entwickelte System nicht auf die Anwendung der Keratomykose begrenzt ist. Auch die Verwendung von Wirkstoffen zur Behandlung von Entzündungen, Glaukomen, viraler oder bakterieller Infektionen sind denkbar. Die entwickelten Fasern sind ebenso wenig auf das Auge limitiert. Denn auch die Anwendung als buccale, dermale oder nasale Arzneiform stellen potenzielle Applikationsmöglichkeiten der elektrogewebenen Fasern dar.

## Acknowledgements

Ich bedanke mich bei meinem Doktorvater Prof. Dr. Karsten Mäder für die Möglichkeit diese Arbeit anzufertigen, aber insbesondere für das mir entgegengebrachte Vertrauen. Die fordernden Aufgaben und Erfahrungen haben mich in meiner persönlichen Entwicklung geformt. Durch unsere enge Zusammenarbeit habe ich dich umso mehr fachlich, als auch persönlich kennen und schätzen gelernt. Vielen Dank!

Weiterhin gilt mein Dank insbesondere:

- » Prof. Dr. Arne Viestenz und Dr. Anja Viestenz aus dem Institut für Augenheilkunde für die praxisnahe Aufgabenstellung, die fachliche Expertise und die effektive Zusammenarbeit. Sie haben mir einen Einblick in den Alltag der unmittelbaren Patiententherapie ermöglicht. Insbesondere bedanke ich mich für das entgegengebrachte Vertrauen die von mir hergestellten Proben *in vivo* zu testen.
- » Prof. Dr. Judith Kuntsche für die Durchführung komplexer A4F Messungen.
- » Prof. Dr. Kurt Merzweiler und Dr. Christoph Wagner für die Arbeit am Röntgendiffraktometer um die Kristallinität der Proben zu untersuchen.
- » Prof. Dr. Thomas Groth und seiner Arbeitsgruppe für die Bereitstellung der 3T3 und NHDF Zellen und die Etablierung des Resazurin-Assays.
- » Dr. Joana Heinzelmann und Ihrem Team unter der Leitung von Prof. Dr. Viestenz für die Durchführung von Zytotoxizitätsuntersuchungen an humanen Zellmodellen.
- » Dr. Militadis Fiorentzis für die Durchführungen der OCT Messungen.
- » Dr. Wolfgang Knolle für die Elektronensterilisation der hergestellten Proben.
- » Dr. Juliana Martins de Souza e Silva und Dr. Cristine Santos de Oliveira für die Durchführung der Nano-CT Messungen.
- » Frank Syrowatka für die ESEM Aufnahmen.
- » Heike Rudolph für die ATR-IR Messungen.
- » Benjamin Grubbauer für seine Geduld und seine Unterstützung bei meinen Schwierigkeiten verbunden mit der englischen Sprache

- » Der Arbeitsgruppe Pharmazeutische Technologie:
- Dr. Henrike Lucas, Ihrer Expertise im Bereich Fluoreszenzimagining und Ihrem einzigartigen Engagement im Hintergrund unserer Arbeitsgruppe.
  - Dr. Marie-Luise Trutschel für die Zusammenarbeit am NMR-Spektrometer und die schöne Zeit als Büromitglied.
  - Johannes Albrecht für die schöne und kollegiale Zeit im Büro.
  - Eric Lehner, Jonas Steiner, Eike Busmann und Anastasios Nalbadis für die erlebten Momente.
  - Manuela Woigk für die Unterstützung und Ihrer unübertroffenen Expertise im Bereich der HPLC Methodenentwicklung.
  - Kerstin Schwarz für die Durchführung der thermischen Analysen.
  - Julia Kollan für die vorbereitenden Arbeiten bezüglich der *in vitro* Zytotoxizitätsuntersuchungen.
  - Diana Rarisch für die unterstützenden Tätigkeiten im Labor.
  - Bei der gesamten AG Pharmazeutische Technologie für die fachlichen Diskussionen, die kollegiale Zusammenarbeit sowohl während Experimenten, als auch in studentischen Praktika. Insbesondere aber für die schöne, gemeinsame Zeit.

Abschließend möchte ich mich bei meiner Familie bedanken. Ihr habt mich ermutigt diesen Weg zu gehen und habt mich dabei unterstützt. Ihr wart für mich da und konntet immer ein offenes Ohr für meine Probleme finden. Ohne eure Unterstützung wäre die Anfertigung dieser Arbeit nicht möglich gewesen.

Vielen Dank!



## Curriculum Vitae

### Persönliche Angaben:

Name: Benedikt Nicolas Göttel  
Geburtsdatum: 05.07.1992  
Geburtsort: Landstuhl

### Berufserfahrung:

Seit 01/2021 Pharmazeut  
Landesamt für Soziales, Jugend und Versorgung (RLP), Trier

12/2016-11/2020 Wissenschaftlicher Mitarbeiter  
AG Pharmazeutische Technologie (Prof. Dr. Karsten Mäder)  
Martin-Luther-Universität Halle-Wittenberg

04/2017-12/2020 Apotheker  
Humanitas Apotheke, Halle (Saale)

05/2016-10/2016 Pharmazeut im Praktikum  
Humanitas Apotheke, Halle (Saale)

11/2015-04/2016 Diplomand  
AG Pharmazeutische Technologie (Prof. Dr. Karsten Mäder)  
Martin-Luther-Universität Halle-Wittenberg  
Thema: „Herstellung polymerer Wirkstoffvliese als potenzielle  
Arzneistoffträgersysteme mit Hilfe des Elektrosinnens und  
anschließender Charakterisierung des Freisetungsverhaltens“

### Ausbildung

11/2016 Approbation als Apotheker

10/2011-09/2015 Studium der Pharmazie  
Martin-Luther-Universität Halle-Wittenberg

04/2011 Abitur  
Gymnasium Ramstein-Miesenbach

Trier, den 16.05.2022

---

Ort, Datum

---

Unterschrift

## List of Publications

### Pear Reviewed Articles

B. Göttel, H. Lucas, F. Syrowatka, W. Knolle, J. Kuntsche, Joana Heinzemann, A. Viestenz, K. Mäder

*In situ gelling Amphotericin B Nanofibers: A new Option for the Treatment of Keratomycosis*  
Frontiers in Bioengineering and Biotechnology Nanobiotechnology 8 (2020)

B. Göttel, J. Martins de Souza e Silva, C. Santos de Oliveira, F. Syrowatka, M. Fiorentzis, A. Viestenz, A. Viestenz, K. Mäder

*Electrospun nanofibers – A promising solid in-situ gelling alternative for ocular drug delivery*

European Journal of Pharmaceutics and Biopharmaceutics 146 (2020) 125–132

J. Zech, S. Leisz, B. Göttel, F. Syrowatka, A. Greiner, C. Strauss, W. Knolle, C. Scheller, K. Mäder

*Electrospun Nimodipine-loaded fibers for nerve regeneration: Development and in vitro performance*

European Journal of Pharmaceutics and Biopharmaceutics 151 (2020) 116–126

M. Riehl, M. Harms, B. Göttel, H. Kubas, D. Schiroky and K. Mäder

*Acid-induced degradation of widely used NIR dye DiR causes hypsochromic shift in fluorescence properties*

European Journal of Pharmaceutical Sciences 132 (2019) 27–33

**Poster Presentations**

B.Göttel, K. Mäder

*New insight into the release profile of PLGA microfibers prepared by electrospinning with focus to the microenvironmental change*

CRS Annual Meeting & Exposition, 2019, Valencia, Spain

B.Göttel, K. Mäder

*Kinetic modelling on drug release from electrospun PLGA fibers*

CRS German Chapter Annual Meeting, 2019, Leipzig, Germany

B.Göttel, K. Mäder

*Release Studies of Ultrathin PLGA Fibers Prepared by Electrospinning*

PBP World Meeting, 2018, Granada, Spain

M. Kirchberg, B. Göttel, A. Schädlich, S. Kempe, H. Metz, K. Mäder

*Non-invasive characterization of the microenvironment inside degrading PLGA polymers*

PBP World Meeting, 2018, Granada, Spain

B.Göttel, K. Mäder

*Electron paramagnetic resonance study of PLGA fibers prepared by electrospinning*

CRS German Chapter Annual Meeting, 2018, Halle, Germany

## Selbstständigkeitserklärung

Hiermit erkläre ich an Eides statt, dass die vorliegende Dissertationsarbeit am Institut für Pharmazie der Martin-Luther-Universität Halle-Wittenberg unter Anleitung von Prof. Dr. Karsten Mäder im Fachbereich Pharmazeutische Technologie und der im Rahmen der Kooperation tätigen Personen selbstständig und ohne fremde Hilfe angefertigt wurde. Sämtliche Quellen und Hilfsmittel die zur Anfertigung der Arbeit genutzt wurden sind an den entsprechenden Stellen kenntlich gemacht. Ich versichere, dass inhaltlich oder wörtlich übernommene Stellen aus anderen Arbeiten in der Arbeit als solche kenntlich gemacht wurden.

Weiterhin erkläre ich, dass die vorliegende Arbeit bisher weder in der gegenwärtigen, noch in einer anderen Fassung an einer andern in- oder ausländischen Fakultät zum Promotionsversuch vorgelegt wurde.

Trier, den 16.05.2022

---

Ort, Datum

---

Unterschrift